# INFORMATION TO USERS

This manuscript has been reproduced from the microfilm master. UMI films the text directly from the original or copy submitted. Thus, some thesis and dissertation copies are in typewriter face, while others may be from any type of computer printer.

**The quality of this reproduction is dependent upon the quality of the copy submitted.** Broken or indistinct print, colored or poor quality illustrations and photographs, print bleedthrough, substandard margins, and improper alignment can adversely affect reproduction.

In the unlikely event that the author did not send UMI a complete manuscript and there are missing pages, these will be noted. Also, if unauthorized copyright material had to be removed, a note will indicate the deletion.

Oversize materials (e.g., maps, drawings, charts) are reproduced by sectioning the original, beginning at the upper left-hand corner and continuing from left to right in equal sections with small overlaps. Each original is also photographed in one exposure and is included in reduced form at the back of the book.

Photographs included in the original manuscript have been reproduced xerographically in this copy. Higher quality 6" x 9" black and white photographic prints are available for any photographs or illustrations appearing in this copy for an additional charge. Contact UMI directly to order.

**UMI**

A Bell & Howell Information Company
300 North Zeeb Road, Ann Arbor MI 48106-1346 USA
313/761-4700 800/521-0600

# Measurement of the Internal Toroidal Magnetic Field on the Helicity Injected Tokamak using the Transient Internal Probe

By

James Paul Galambos

A dissertation submitted in partial fulfillment of the
requirements for the degree of

Doctor of Philosophy

University of Washington

1996

Approved by Thomas R. Jarboe
(Chairperson of the Supervisory Committee)

Program Authorized
to Offer Degree NUCLEAR ENGINEERING DEPARTMENT

Date 31 OCTOBER 1996

In presenting this dissertation in partial fulfillment of the requirements for the Doctoral degree at the University of Washington, I agree that the Library shall make its copies freely available for inspection. I further agree that extensive copying of this dissertation is allowable only for scholarly purposes, consistent with "fair use" as prescribed in the U. S. Copyright Law. Requests for copying or reproduction of this dissertation may be referred to University Microfilms, 1490 Eisenhower Place, P.O. Box 975, Ann Arbor, MI 48106, to who the author has granted "the right to reproduce and sell (a) copies of the manuscript in microform and/or (b) printed copies of the manuscript made from microform."

Signature 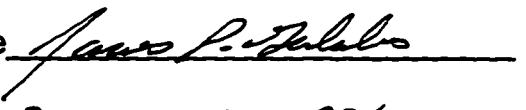

Date 31 OCTOBER 1996

University of Washington

Abstract

Measurement of the Internal Toroidal Magnetic Field on the Helicity Injected Tokamak using the Transient Internal Probe

by James Paul Galambos

Chairperson of the Supervisory Committee:

Professor Thomas Jarboe
Department of Nuclear Engineering

The Transient Internal Probe is a novel diagnostic technique specifically developed to measure internal magnetic field profiles in hot plasmas. The concept involves shooting a magneto-optic probe through a plasma at high velocity so that field measurements are obtained before ablation of the probe begins. The magnetic field profiles are obtained by illuminating the probe with a linearly polarized laser and measuring the amount of Faraday rotation induced in the beam as it passes through the probe and is reflected back to the detection system. Coupling between the gas gun and the high vacuum regime of the plasma chamber is achieved with a highly efficient gas interface system such that less than 0.4 torr-l (0.003%) of the muzzle gas enters the plasma chamber. Determination of the polarization angle of the reflected light is accomplished with a high speed, high resolution polarimeter.

The TIP concept was demonstrated by measuring the internal toroidal magnetic field profile on the Helicity Injected Tokamak. Measurements were conducted with the probe traveling more than 1.9 km/s. Field measurement accuracy was better than 2.5 % with spatial resolution of better than 1 centimeter. Qualitative results concerning the time required for ablation of the probe to begin were obtained and these results supported the surface boiling model used to predict probe behavior. These results proved the diagnostic to be a valuable new tool for investigating the magnetic structure of hot plasmas.

## Table of Contents

## List of Figures

## List of Tables

**Acknowledgments**

I am deeply humbled when I reflect on the enormous contributions of so many individuals to the success of this project. The teamwork displayed in making this project work was unsurpassed compared with any endeavor of which I have been a participant. Of the many individuals who participated, I would like to recognize a few extraordinary efforts.

First and foremost were the efforts of my wife, Karen. She was unwavering in her support, allowing me to pursue this degree despite the rather significant sacrifices it imposed on our family. She truly rose above the call of duty, staying up many late nights hand grinding special glass bullets to the precise tolerances required by the experiment while I analyzed data, so that we could shoot the next day and get more data. And, of course, her help critiquing and proofreading this document was invaluable.

I also am deeply indebted to my lab partner and close friend, Mike Bohnet for his tireless efforts supporting me and this project. Mike is an exceptional engineer, and his insights and selfless devotion to the project were the difference many times over, between success and failure.

Dennis Peterson, the lead instrument maker in our shop, was also essential to the success of this experiment. Dennis treated me to the art of machining and mechanical design. His wisdom, critiquing flawed designs and proposing alternative ideas, saved inestimable amounts of time and effort. Not to mention, working with Dennis was a complete joy.

My faculty and staff support was outstanding. I want to recognize professor Tom Jarboe, the principle investigator for this project, who ably led the research and professor Tom Mattick who was an invaluable addition to the team. Additionally, I am grateful to Dr. Brian Nelson for his enormous patience and enthusiasm. John Rogers, the staff engineer for the HIT experiment, was equally helpful and patient.

Finally, several students contributed significantly to this research. In particular graduate students, Dave Orvis, Adam Martin, and Chad Painter were a constant source of encouragement and help. Many undergraduates helped as well, and I especially want to recognize the efforts of Ivan Kwok, John Utz, Ngoc Sin, Kevin Kdep, and Michael Wu.

As always, I am struck by the willingness of other to help me. Unfortunately these words do little to describe the depth of my gratitude toward these individuals. But I thank God for each, and will not forget their efforts.

## 1. Introduction

Obtaining a lasting, safe, dependable, and economical energy source has been a goal of industrialized nations for over a century. For nearly a century, oil has proven to be the energy source of choice. Unfortunately, burning oil has many negative environmental effects. In addition, the relative scarcity of oil inside the national boundaries of the major industrial nations has resulted in intense international efforts to procure stable oil supplies. This pursuit has led to a number of conflicts and required the diversion of enormous amounts resources and effort to maintain a stable energy supply. Recent events in the Persian Gulf have served to highlight this point.

Several energy alternatives are available, but each suffers from significant drawbacks. Fusion energy promises the potential of virtually unlimited, safe, accessible energy. The tremendous energy density of this source is evident in the explosion of a hydrogen bomb. Unfortunately, unlocking the power of fusion energy in a controlled manner has proved to be quite difficult. The fundamental problem is overcoming the electrostatic repulsion between the protons in the nucleus of the fusing particles such that the powerful nuclear force can take over to fuse the particles and release the fusion energy. Several methods and techniques to unlock the energy of fusion are being investigated. The most prominent effort involves heating isotopes of hydrogen into a plasma until nuclei in the high energy tail of the velocity distribution have the kinetic energy necessary to overcome the repulsive force. The problem then becomes confining this hot (several million degree) plasma such that the fusion reactions occur in sufficient quantity to exceed the energy input required to heat and confine the plasma. Magnetically confined fusion is one concept that has made significant progress towards realizing significant fusion power.

### 1.1 Magnetically Confined Plasmas

### 1.1.1 Magnetic Confinement

In magnetic confinement, external coils are used to establish magnetic fields which combine with magnetic fields generated by currents within the plasma. The topology of these fields is engineered such that closed magnetic surfaces are created that envelop the plasma. Tension in the field lines resists bending and compression which provides a restoring force to contain the pressure of the plasma. For ideal plasmas in equilibrium, the balance between the outward plasma pressure and magnetic confining force is given by the ideal MHD equation

$$\mathbf{J} \times \mathbf{B} = \nabla P \qquad \text{Eq. 1.1}$$

in which the plasma velocity is assumed to be zero. Here **J** is the current density in the plasma, **B** is the magnetic field, and P is the pressure. This equation results in surfaces of constant pressure. For toroidal systems, equation 1.1 can be rewritten in terms of these flux surfaces. The resulting equation, called the Grad-Shafranov equation, provides a method for obtaining the equilibrium plasma profile. Specifically in two dimensions, for a toroidally symmetric system, it is

$$R^2 \nabla \cdot \left(\frac{\nabla \psi}{R^2}\right) = -\mu_0 R^2 \frac{dP}{d\psi} - F\frac{dF}{d\psi} \qquad \text{Eq. 1.2}$$

In this equation $F(\psi)$ is related to the toroidal field by

$$F(\psi) = RB_t \qquad \text{Eq. 1.3}$$

Thus, the flux function $\psi$ is related to the two undetermined functions $P(\psi)$ and $F(\psi)$. In order to solve the equation for the flux surface the two free functions must be measured or assumed. The pressure profile requires knowledge of the internal temperature profile and density profile. Measurement of the electron

temperature profile can be determined non-intrusively with lasers by using multi-point Thompson scattering. Determination of the ion temperature profile can be obtained using neutral particle analyzers to evaluate the energy distribution of ejected ions that have been neutralized through charge exchange with injected neutral particles. Density profiles can also be obtained non-obtrusively using reflectometry or multi-chord interferometry. The internal toroidal field profile is still required to complete the determination of the flux surface function $\psi$. Once determined, the ideal MHD equilibrium magnetic and current profiles can be easily calculated using equations 1.4a,b respectively.

$$B = \frac{1}{R}\nabla\psi \times e_\varphi + \frac{F}{R}e_\varphi \qquad \text{Eq. 1.4a}$$

$$\mu_0 J + \frac{1}{R}\frac{dF}{d\psi}\nabla\psi \times e_\varphi - R\nabla\cdot\left(\frac{\nabla\psi}{R^2}\right)e_\varphi \qquad \text{Eq. 1.4b}$$

With an accurate characterization of the plasma equilibrium, efficient progress can be made towards improving plasma performance.

### 1.1.2 Significance of Current Profile

One of the most important parameters in plasma confinement is the plasma current profile. Coincident with the development of internal magnetic field diagnostics, most notably the motional stark effect diagnostic, current profile studies began which showed that plasma confinement and stability can be greatly improved through proper manipulation of the current profile. By changing the current profile from the normal broad profile of a tokamak to a more peaked profile, Ferron et al. [1] noted that the L-mode confinement was improved by a factor of four and H-mode confinement, by as much as three over $\tau_{ITER\text{-}89p}$ scaling. Additionally, the plasma was more stable to ballooning modes. The cause for these improvements was presumed due to the increased shear, but a formal model was not developed. Kessel et al. [2] formally modeled

various current profiles and showed theoretically that a profile that is peaked off axis results in a region of negative shear followed by a steeply increasing positive shear. This profile was studied numerically and found to have excellent stability properties, high bootstrap current fraction, and exceptional confinement. Recent experiments on TFTR [3] have transiently achieved this profile with dramatic results. Confinement was improved to neo-classical levels over the center region of the plasma. These developments highlight the importance of accurately determining the current profile in order to effectively study and manage the plasma.

## 1.2 Internal Plasma Magnetic Field Diagnostics

### 1.2.1 Motional Stark Effect Diagnostic

Several diagnostics have been developed to investigate the internal magnetic structure of hot plasmas. The obvious method is to directly insert a probe into the plasma. But high heat loading, which is discussed in chapter 2, precludes the use of mechanically inserted probes which operate on mili-second time scales, whereas ablation occurs on sub-milisecond times scales. Consequently, alternative diagnostic techniques are required to measure the internal magnetic fields of hot plasmas.

One of the most powerful internal plasma diagnostics is the measurement of local magnetic pitch using the motional stark effect diagnostic (MSE). For MSE, an energetic neutral beam is injected into the plasma. As the neutral beam propagates through the plasma, collisions with background ions and electrons occur which excite these atoms. The motion of these ions across magnetic field lines creates an electric field ($\mathbf{E} = \mathbf{v} \times \mathbf{B}$). Here $\mathbf{v}$ is the velocity of the beam. This electric field acts on the excited hydrogen atoms by splitting the states and polarizing the emitted radiation. The splitting of the Balmer $\alpha$ line ($\lambda_0 = 6562$ A) results in fifteen lines which are grouped into two sets. The first is

the $\pi$ series ($\Delta m = 0$) which are polarized parallel to **E**. The second set is the $\sigma$ series which are polarized parallel to the local magnetic field. By collecting emitted radiation from a localized portion of the beam and measuring the polarization of that light, the direction of the local field can be determined.

Several large tokamaks which have neutral beam injectors use MSE to determine the internal q profile. Initial measurements on the Princeton Beta Experiment (PBX) resulted in a 6% uncertainty in q-profile with two centimeter resolution [4]. Similar results were achieved on General Atomic's DIII-D machine [5]. Frequency response for these measurements is on the order of a kilohertz due to the time required to collect sufficient light for good accuracy.

Certain drawbacks limit the effectiveness of the MSE diagnostic. First, it requires a large neutral beam accelerator to perform the experiment. Second, MSE requires large magnetic fields in order to get sufficient splitting of the energy levels, thus it is inappropriate for devices without large toroidal fields. The slow time response, which is a function of the time required to collect sufficient light for a measurement, does not permit investigation of magnetic fluctuations in the plasma. Additionally, the slow time response limits the spatial resolution of the diagnostic. Finally, MSE does not measure the magnitude of the local field, but only the direction.

### 1.2.2 Heavy Ion Beam Probes

Another method of measuring internal magnetic fields in Tokamaks is called the Heavy Ion Beam Probe (HIBP) . For HIBP, heavy ions of known energy are injected into the plasma where they become doubly ionized. Magnetic forces strongly alter the trajectory of the beam and the toroidal displacement of the exiting particles is measured. By making assumptions about the toroidal field and plasma current distribution, the displacement measurement can be correlated to the poloidal field localized to a small sample

volume. This volume is approximately 0.3 $cm^3$ and is determined by the beam energy, entrance angle, and position of detector.

This method has been used to measure MHD fluctuations in the Texas Experimental Tokamak [6]. HIBP has many advantages. Time response and spatial resolution are excellent. Field resolution on the fluctuation measurement above were reported to be within 5 percent of simulation. Finally, besides measuring local magnetic fields, this diagnostic can be used to investigate electric potential, density, and temperature. Unfortunately, for large tokamaks, it is very difficult to produce high enough beam energy to reach the center of the plasma. The orbits become smaller than the radius of the plasma. Additionally, significant knowledge of the internal field and current of the plasma are required to properly isolate the measurement to the local poloidal field. These limitations make the diagnostic inappropriate for non-tokamak configurations and somewhat negate its usefulness in calculating the current profile.

### 1.2.3 Multi-chord Faraday Rotation

Multi-chord faraday rotation polarimetry is another technique which has been effectively used to measure internal magnetic field profiles in plasmas [7,8]. This technique utilizes the faraday rotation of a long wavelength laser to determine the chord averaged magnetic field. The magnitude of the faraday rotation is given by

$$\alpha = C_f \int n_e B \cdot dl \qquad \text{Eq. 1.5}$$

where $\alpha$ is amount of rotation and $C_f$ is a constant. If the electron density profile, $n_e$, is known and several chords are measured, the magnetic profile can be obtained by using an Abel inversion. This method has the advantage of being completely non-perturbing to the plasma. Time response is limited by the type of polarimetry, but typically is 1 msec or less. A disadvantage of this

technique is that the measurement is a chord average and it requires knowledge of the electron density profile. Also, refraction of the laser beam for the long wavelengths necessary to get sufficient rotations is quite significant. This effect moves the output beam with respect to the detectors, giving spurious signals that are not distinguishable from rotation.

Other methods such as measuring the tilt angle of the ablation plume of injected impurity pellets [9], or observation of Zeeman splitting in light emission from lithium pellets [10,11] have been used. Both of these methods are perturbing and somewhat limited in accuracy relative to the methods discussed above. For configurations without internal diagnostics the profile is inferred from solutions to the Grad-Shafronov equation fit to data from external probes measuring global parameters. Unfortunately, a large number of internal profile solutions can match the surface measurements.

## 1.3 Transient Internal Probe

### 1.3.1 Diagnostic Concept

Presently, in the magnetic fusion community, a large gap exists concerning the ability to determine internal current profiles in hot plasmas. Only large tokamak experiments with neutral beam capabilities are able to make internal profile determinations using magnetic pitch angle data obtained form motional stark effect diagnostics. Small scale tokamak experiments without neutral beam injection and so called 'alternative concepts' that do not have large vacuum magnetic fields to use motional stark effect diagnostics, do not have an effective means of making the necessary internal field measurements required to determine the plasma current profile. These experiments play a crucial role in fusion development by providing cost effective platforms to test new technologies and ideas. But without the ability to measure internal current profiles, experimentalists for these experiments are severely limited in their

ability to effectively understand the internal physics of their devices. This makes improvements in performance through manipulation of the internal current profile highly difficult.

The transient internal probe (TIP) diagnostic[12-15] was developed to close this gap by creating a new diagnostic designed to measure the internal magnetic field profile in hot plasmas. The concept, shown in Figure 1.1, involves shooting a diamond clad magneto-optic probe through the plasma at high velocity (2-5 km/s) allowing measurement of the local magnetic field before surface boiling occurs. Magnetic field measurements are obtained by illuminating the probe with an Argon laser such that the light passes through the probe material and is retro-reflected off the rear surface of the probe back to a detection system located outside the plasma. The local magnetic field is determined by knowing the verdet constant of the probe and measuring the amount of faraday rotation in the reflected light.

The TIP diagnostic has many potential advantages over other magnetic field diagnostics. First, though the probe is a heat sink locally, it is relatively small (4mm x 4mm x 10mm) and non-perturbing to the plasma as a whole since it exits the plasma prior to the onset of significant ablation. Additionally, it measures the direction and magnitude of the magnetic field directly. Because the magnitude of the measurement is based on the polarization state of the reflected light which is periodic, the accuracy of the measurement is determined by the resolution of the polarimeter, independent of the magnitude of the field being measured. Time response of the probe is on the order of a gigaherz. This time is limited by the time required for the field to 'soak' into the probe and will be discussed in Section 2.2.2. Presently, the electronics of the detection system are more constraining. Finally, TIP can be used to measure fields in any magnetic configuration, including transient plasmas in which TIP could be stationary and allow the plasma to pass over the probe.

The most significant constraints on the TIP diagnostic are the endurance of the probe for a given energy density of the plasma, and the component of the magnetic field that is accessible to be measured. Section 2.2.1 discusses the heat loading and belief time for TIP as a function of plasma temperature and density. Presently only the component of the magnetic field parallel to the direction of flight is measured. This limits TIP's ability to probe toroidal configurations, since measurements of the poloidal field have to be taken off the magnetic axis of the plasma. This problem is being addressed and significant progress has been made towards developing a probe which measures the field component perpendicular to the flight path of the probe [16]. This will allow a complete profile of the poloidal field. This paper will deal with axial probe measurements only.

### 1.3.2 Discussion of Diagnostic Development and Results

The first goal of this research program was to develop the diagnostic concept and demonstrate its capabilities for making internal magnetic field measurements in a hot plasma. Several technological challenges were encountered in the development of TIP. The intense energy density of magnetically confined plasmas limits probe exposure to the plasma to less than a few hundred micro-seconds, necessitating a gas gun to generate velocities of 2-5 km/s. Coupling the gas gun to the plasma vacuum chamber encompassed connecting systems with 9 orders of magnitude in pressure differential. This forced the development of a gas interface system which trapped the muzzle gases. The most difficult challenge involved developing a launch system that accelerated the glass probes without fracturing the glass and delivered the probe to the plasma in a stable flight profile with no tumbling. Finally, a new fast acting polarimetry system was developed to accurately measure the polarization angle in sub microsecond time frames. These challenges and the engineering

solutions developed to make the concept work are discussed further in chapters 2, 3 and 4.

The second goal of this research program, representing the culmination of the developmental process, was to make internal magnetic field measurements in a hot plasma. Measurements were conducted on the Helicity Injected Tokamak (HIT) [17]. Several measurements of the toroidal field profile were made allowing evaluation of the diagnostic performance and evaluation of the diagnostic's effect on plasma parameters and tokamak performance. Results of these measurements are included in chapter 5. Finally, in chapter 6, concluding remarks concerning the diagnostic are included along with suggestions for future applications and diagnostic improvement.

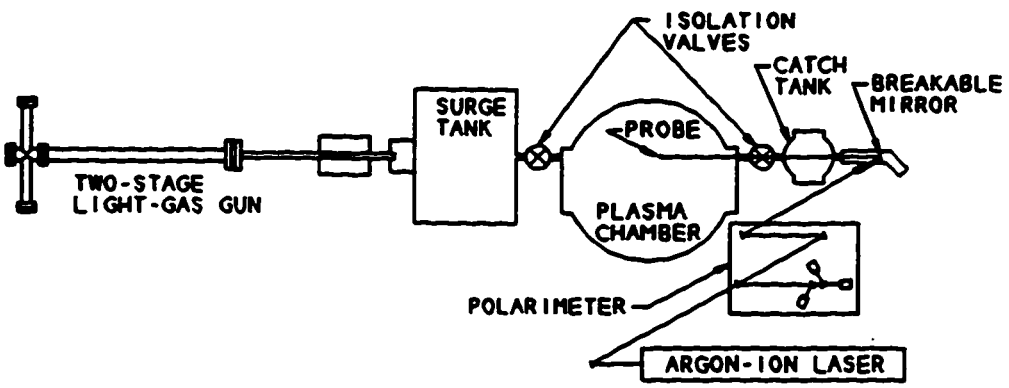


Figure 1.1 Overview of Transient Internal Probe concept.

## 2. Theory of Operation

### 2.1 Faraday Rotation

Faraday rotation within the probe is the physical principle upon which the TIP diagnostic is based. Faraday rotation, though a quantum effect, can be well understood with a classical model. Inside the probe material the optically resonant electrons are driven by the applied electric field of the incident laser light. This light, which is linearly polarized, can be considered the sum of a left hand circularly polarized wave and a right hand polarized wave. These waves drive the electrons in a circular motion about the nucleus. In the presence of an external magnetic field, the energy state of the resonant electrons is split due to the change in potential energy as the magnetic dipole of the atoms interacts with the external field according to the equation

$$U = \mathbf{m} \cdot \mathbf{B} \qquad \text{Eq. 2.1}$$

where **m** is the magnetic dipole of the atom and **B** the external field. Note the magnitude of the energy split is based on the component of B parallel to the magnetic dipole, and hence the propagation vector of the laser. The effect of the energy split will be of opposite sign depending on the direction of the circular driving force. Thus the right handed wave and left handed wave will interact with a different energy level. This difference results in different indexes of refraction for the respective circularly polarized waves. When the circular waves are recombined this circular dichroism results in the rotation of the polarization angle given by

$$\Psi = \pi(n_+ - n_-)\,\Delta z/\lambda \qquad \text{Eq. 2.2}$$

In this equation $\Psi$ is the amount of faraday rotation, $n_+$ and $n_-$ represent the different refractive indexes for the circular light, $\lambda$ is the wavelength of the laser,

and $\Delta z$ is the distance traveled in the medium. The effect of the magnetic field is contained in the difference of refractive indexes in equation 2.2. Separating the magnetic field magnitude from equation 2.2 yields a linear relationship between the field strength and the amount of rotation as shown in equation 2.3 below.

$$\Psi = vB\Delta z \qquad \text{Eq. 2.3}$$

where $v$ is the verdet constant, which is a property of the material.

As discussed earlier, faraday rotation also occurs from the interaction of the magnetic field and the laser light as it passes through the plasma. The advantage of the TIP concept over conventional faraday rotation measurements is the enormous difference in verdet constant of the probe material relative to the verdet constant of the plasma. This allows local field measurements to be made with small probes, as opposed to chord averaged measurements over the length of the plasma. As an example, a plasma with density $n_e=10^{14}$ $cm^{-3}$ has a verdet constant on the order of $2 \times 10^{-9}$ deg/G cm at a wavelength of 514 nm, whereas the verdet constant for typical probe material is $10^{-2}$ deg/G cm. Consequently a one meter path through a one tesla field would result in about 0.002 degrees of rotation.

## 2.2 Plasma Probe Interaction

The plasma interaction with the probe is a fundamental concern to the operation of the TIP diagnostic. Three basic processes are of interest, heat loading to the probe, physical sputtering of the probe surface, and magnetic diffusion time into the probe. Heat loading is important because this determines the amount of time a probe can make measurements in the plasma. Sputtering of the probe surface is a concern since this process results in impurities being introduced into the plasma immediately upon the probe's entrance into the

plasma. Finally, the magnetic diffusion time sets the physical limit of the probe's response time to magnetic fluctuations in the plasma.

### 2.2.1 Thermal Loading

The probe 'belief time' is defined as the time required for the surface to become hot enough to boil. Once the surface of the probe begins to vaporize, significant impurities are introduced into the plasma and the optical performance of the probe may be degraded. In order to calculate the belief time, the heat load to the probe must be known. Determining the heat loading to a surface in a plasma is complex, but significant work has been done by a number of researchers using several different models to account for the various processes that occur at the boundary [18-23]. Once the heat load is determined, estimation of the belief time is done by using a conductive heat transfer model.

In order to calculate the heat loading, the probe is treated as a non-conducting heat sink in which the energy of the ions and electrons is deposited to the surface upon impact. Assuming $T_i$ is not $>>T_e$, the faster moving electrons form a negative potential sheath around the probe which retards the electrons and accelerates the ions so that the net current to the surface is zero. Effectively, the sheath serves as a mechanism to transfer energy from fast electrons to the ions. It can be shown [20] that the sheath typically extends a few debye lengths into the plasma. In this region, charge neutrality is not maintained.

One of the important particle flows is the flow of electrons from the surface called secondary electron emission. Secondary electron emission can be caused by energetic electron impact, thermionic emission, radiation, or ion impact. Significant changes to the sheath occur as a result of secondary electron emission. As the cold electrons leave the surface, the sheath potential

becomes less negative allowing more hot electrons to reach the probe surface. This has the result of creating a complex temperature distribution with both a hot electron and cold electron temperature distribution.

An often cited model that takes into account secondary electron emission in determining the sheath potential and heat load for a non-conducting surface facing a hot Maxwellian plasma has been developed by P. Stangeby. He shows that prior to the sheath, a pre-sheath region exists in which quasi charge neutrality is maintained, but the electron density drops by the Boltzman factor given by

$$n_{se} = n_{\infty} e^{\frac{e\varphi_{se}}{kT_e}}. \qquad \text{Eq. 2.4}$$

In this equation $n_{se}$ is the density at sheath edge, $n_{\infty}$ is the plasma density far from the probe, and $\varphi_{se}$ is the potential difference from the sheath edge to the plasma far from the probe.

By solving Poisson's equation the Bohm criteria is obtained showing that the ions are accelerated to the ion acoustic speed, $C_s$, in order for the sheath to form where isothermal flow is assumed

$$C_s = \sqrt{\frac{kT_e + kT_i}{M_i}}. \qquad \text{Eq. 2.5}$$

Once the ions reach the sheath edge, they are simply accelerated to the probe surface such that the incident flux is

$$\Gamma_i = n_{se} C_s \qquad \text{Eq. 2.6}$$

The electrons arrive at their thermal velocity, but their density is reduced by the sheath potential. Additionally, secondary electron emission reduces the net flux of electrons to the probe surface. The resulting electron flux is thus given by

$$\Gamma_e = \frac{1}{4} n_{se} (1-\gamma) C_{th} e^{-\frac{e\varphi_f}{kT_e}} \qquad \text{Eq. 2.7}$$

where $\gamma$ is the secondary electron emission coefficient and

$$C_{th} = \left(\frac{8k\,T_e}{\pi m_e}\right)^{1/2} \qquad \text{Eq. 2.8}$$

Equating the ion flux to the electron flux results in an analytical expression for the sheath potential of

$$\frac{e\varphi_f}{kT_e} = \frac{1}{2} \ln\left[\left(2\pi \frac{m_e}{M_i}\right)\left(1+\frac{kT_i}{kT_e}\right)(1-\gamma)^{-2}\right] \qquad \text{Eq. 2.9}$$

Note that this floating potential is for the sheath region only, and the pre-sheath potential must be added to get the total potential difference. The pre-sheath potential, $e\varphi_{se}$ is between 0.5 and 0.7 $T_e$. Using this value

$$n_{se} = \frac{1}{2} n_\infty \qquad \text{Eq. 2.10}$$

Heat loading to the probe is then obtained by multiplying the electron flux by the particle kinetic energy minus the potential energy of the sheath field and adding the kinetic energy of the incident ion particles. This yields the equation

$$Q = n_{se} C_s \left[\frac{2kT_e}{1-\gamma} - e\varphi_f + 2kT_i\right]. \qquad \text{Eq. 2.11}$$

This model can be improved by accounting for the reflection of particles and thus energy at the surface along with taking into account ionization energy and recombination energy since the ions are neutralized when they strike the surface. The improved equation for heat loading normalized to the particle flux times the electron temperature for comparison with other references is then

$$\delta = \left[\frac{2kT_e}{kT_e(1-\gamma)} - e\varphi_f\right](1-R_{eE}) + \frac{2kT_i(1-R_{iE})}{kT_e} + e\varphi_{se} + \frac{\chi_i}{kT_e} + \frac{\chi_r}{kT_e}(1-R_{in}). \qquad \text{Eq. 2.12}$$

where

$$\delta \equiv \frac{Q}{n_{se}C_s kT_e}$$

| | |
|---|---|
| $\chi_i$ | ionization energy |
| $\chi_r$ | molecular recombination energy |
| $R_{eE,iE}$ | energy reflection coefficient for electrons and ions |
| $\gamma$ | secondary electron emission fraction |

In order to calculate the heat loading, the values for the various coefficients must be determined. The secondary electron emission coefficient is the most difficult to determine since it varies considerably with incident particle energy and surface material. Studies by Pedgley et al. [24] and Woods et al. [25] give values for $\gamma$ for various types of graphite surfaces. No data is available for diamond emission resulting from plasma impact so values for clean graphite will be used. For the case of a TIP probe traveling through a 1 keV plasma with $kT_i = kT_e$, $\gamma$ is approximately 0.75. Values for the energy reflection coefficient, again for graphite, are given in reference [26] with $R_e$ and $R_i$ about 0.9. Ionization energy is 13.6 eV for hydrogen and the recombination energy 4-5 eV such that for high plasma energies of a keV they can be neglected. Using these numbers and a plasma density of $5 \times 10^{19}$ m$^3$

$$e\varphi_f = -1.45kT_e \quad \text{and} \quad \delta = 10.8$$

yielding an absolute heat flux of 1.3 MW/cm$^2$. This compares with a model by Loveberg [18] which simply treats the ions and electron distributions as Maxwellian distributions entering the sheath at their respective thermal speeds. The result is a sheath potential for deuterium given by

$$e\varphi_f = kT_e \ln(\sqrt{\frac{m_e}{M_i}}) = -4.1kT_e \qquad \text{Eq. 2.13}$$

and a heat loading given by

$$Q = \frac{n}{\sqrt{2\pi m_i}}(kT)^{3/2}(\ln\sqrt{\frac{M_i}{m_e}} + 4). \qquad \text{Eq. 2.14}$$

The corresponding heat flux is 0.56 MW/cm$^2$. The effect of the secondary electron emission is to reduce the sheath potential which reduces the energy of the ions at impact, but allows more electrons to reach the surface and increase the overall heat load. If the surface can take the heat loading, secondary electron emission can have the beneficial effect of reducing the amount of sputtering by lowering the ion impact energy [23].

In the Stangeby model for heat loading, the ions are assumed to remain Maxwellian despite being accelerated in the pre-sheath region. Additionally, this model does not account for the change in temperature distribution for the electrons due to the presence of cold secondary emission electrons. Shirashi [21] has developed a simplified model for determining the sheath potential and heat flux for this case. Swager [22] has developed a complete kinetic model that numerically solves the Vlasov equation and Poisson's equation accounting for secondary electron emission and two component temperature distributions. Comparisons done by Swager [22] show that for electrons in thermal equilibrium with the ions the difference between his model and the Stangeby model for the heat flux is less than 10 percent.

The majority of these studies have been motivated by concerns about heat loading to the first wall of magnetically confined plasmas. Kuteev et al. [28] injected small (r=23 μm) graphite pellets into the T-10 tokamak as a means of developing a diagnostic to measure the $nT^{3/2}$ profile in a tokamak. To do this, they modeled the heat loading using a numerical model developed by

Laframoise, [29] which takes into account the ion energy distribution, but neglected secondary electron emission. The results of the experiment showed the observed delay time until the onset of surface boiling agreed with the calculation to 50% [28]. The actual delay time was shorter which is consistent with the fact that secondary electron emission was neglected causing the calculated heat flux to be somewhat lower than the actual heat flux.

### 2.2.2 Calculation of Belief Time for the Probe

The belief time is found by solving the heat equation for constant heat flux on an infinite slab. As shown in reference [30], the equation describing the temperature as a function of position and time is

$$T(x,t) = T_o + \frac{2Q}{\kappa}\sqrt{\alpha t/\pi}\, e^{-\frac{x^2}{4\alpha t}} - Q\,erfc\left(\frac{x}{2\sqrt{\alpha t}}\right) \qquad \text{Eq. 2.15}$$

where $\alpha$ is the thermal diffusivity of the material and $T_O$ is the initial temperature. The characteristic heat penetration depth is then

$$\lambda = 2\sqrt{\alpha t} \qquad \text{Eq. 2.16}$$

For probe materials this depth is much less than a millimeter, making the infinite slab approximation acceptable. Setting x equal to zero gives the surface temperature as a function of time and heat loading. Using the heat load derived earlier for Q, and letting T equal the boiling temperature of the probe surface material, equation 2.15 can be solved for the probe 'belief time,' $t_b$, given by

$$t_b = \frac{T^2 \pi \rho k c}{(Q)^2} \qquad \text{Eq. 2.17}$$

where k is the thermal conductivity, $c$ is the heat capacity, and $\rho$ is the density of the probe. Figure 2.1 shows calculations of the belief time for various probe materials at a plasma density of $5 \times 10^{13}$ $cm^{-3}$ as a function of plasma

temperature. Temperatures encountered in this experiment on HIT were in the range of 40-60 eV allowing probing of the plasma with unclad probes, provided the retro-sheet is protected. Clearly, more refractive cladding must be used to investigate plasmas with $T_e$ above 100 eV. Shown in Figure 2.2 are several belief times which have been calculated assuming a diamond coated probe. Also plotted are some familiar fusion devices indicating theoretical range of TIP operation.

This calculation is conservative in that no reduction in particle flux due to magnetic field lines is taken into account and no cooling of the plasma sheath around the probe is assumed. Obviously, the validity of this model is based on the belief time for the probe being less than the exposure time of the probe in the plasma. If the belief time is exceeded while the probe is in the plasma, significant ablation will occur. This ablation will require the heat transfer model for the probe to include convective heat transfer as well as conduction. In this situation, the heat loading to the probe is reduced by the cold ablation cloud surrounding the probe. Probe survival in the plasma will thus be extended, but large amounts of probe surface material impurities will be introduced into the plasma. Parks [31] has modeled this ablative interaction and determined that a 1 mm diameter diamond traveling at 6.3 km/s could reach the center of an ignited plasma. Depending on the impurity tolerances of the plasma, the optical performance of an ablating probe, and the frequency response desired, the TIP diagnostic may be able operate in regimes where the belief time is exceeded. Ultimately the degree to which the probe is susceptible to ablative effects will determine the plasma density and temperature regime in which the TIP diagnostic can be used.

### 2.2.3 Surface Sputtering

Physical sputtering involves the ejection of neutral atoms from the surface of the probe into the plasma as a result of energetic ion bombardment.

Sputtering of the probe surface is important because it results in the introduction of impurities immediately upon contact with the plasma, well before ablation begins. Much work has been done to investigate the sputter rates of various plasma facing materials such as graphite, silicon carbide, beryllium, tungsten, and various steel alloys [26]. The sputter rates vary significantly as a function of incident particle type, particle energy, surface material, and surface material temperature. Unfortunately little data is available on diamond, but the graphite data should serve well as a conservative estimate of diamond behavior. The physical sputter rate for graphite has been modeled quite accurately by Kawamura [32] and it peaks at approximately 0.05 atoms sputtered per incident ion. The peak occurs at an incident ion energy of 100 eV and drops quickly to less than $10^{-3}$ for incident ions with energies of 1 keV.

These results refer only to physical sputtering. Many mechanisms exist for carbon which enhance the sputtering process such as chemical sputtering, radiation enhanced sublimation, and self-sputtering. Chemically enhanced sputtering occurs when hydrogen ions react with carbon atoms to form $CH_4$. This enhancement peaks noticeably to 0.1 atoms/ ion for surface temperatures between 800 and 1000 $^0$C. Radiation enhanced sputtering due to the creation of excited carbon atoms is observed at temperatures above 1300 $^0$C and grows exponentially reaching unity around 2200 $^0$K. Figure 2.3 is a reproduction taken from reference [26] showing the sputtering rate for graphite as a function of temperature. Assuming a highly conservative average sputter rate of unity and diamond clad probes of the same dimension as present TIP probes (4mm x 4mm x 1cm), the impurity introduction rate can be calculated. Using the formula for ion flux rate given in equation 2.5 for a 1 keV plasma at 5 x $10^{13}$ $cm^{-3}$, the ion flux is $10^{15}$ ions/$cm^2$ μsec. The rate of carbon release to the plasma is 2 x $10^{15}$ atoms/μsec. For a tokamak the size of DIII D (20 $m^3$ plasma volume) a 500 μsecond transit time would result in an additional impurity fraction of 0.1%.

### 2.2.4 Magnetic Field Diffusion into the Probe

Diffusion of the magnetic field into the probe determines the theoretical probe response time. Other factors such as the speed of the data acquisition system may set more restrictive limits. But the theoretical limit is set by the time required for the magnetic field to diffuse through the plasma sheath and into the probe. For the case of a stagnant conducting probe, this time can be significant since depending on the size of the probe. Lovberg [18] provides a calculation of this response time by solving the magnetic diffusion equation for a conducting material. The result is a characteristic time given by

$$\tau = \frac{\mu_o r^2 \sigma}{4} \qquad \text{Eq. 2.19}$$

where r is the probe radius and $\sigma$ is the conductivity of the probe and plasma which are assumed about equal. This is not appropriate for the TIP probe since the probe is a dielectric and the plasma is not stagnant. Essentially the field is convected to the probe as the plasma condenses on the probe surface. At the surface, diffusion into the dielectric glass material is virtually instantaneous.

In the case of strong ablation where a cold plasma cloud around the probe acts as a conducting surface and carries current around the probe, the probe response would be delayed. Calculation of the diffusion time for this scenario can be done by treating the probe as if it had a thin conducting shell with conductivity equal to the cold plasma cloud surrounding probe. The resulting characteristic diffusion time is then given by

$$\tau = \frac{\mu_o r \Delta r \ \sigma}{2} \qquad \text{Eq. 2.20}$$

where r is again the radius of the probe and $\Delta r$ is the cloud thickness. Assuming a plasma sheath with a temperature of 10-100 eV and density of $10^{20}$ $m^{-3}$ yields a conductivity of $10^4$-$10^6$ respectively $(ohm\ m)^{-1}$ using Spitzer resistivity.[33]

Taking $\Delta r$ and r to be 2mm, the diffusion time is on the order of a few nano-seconds to a few micro-seconds.

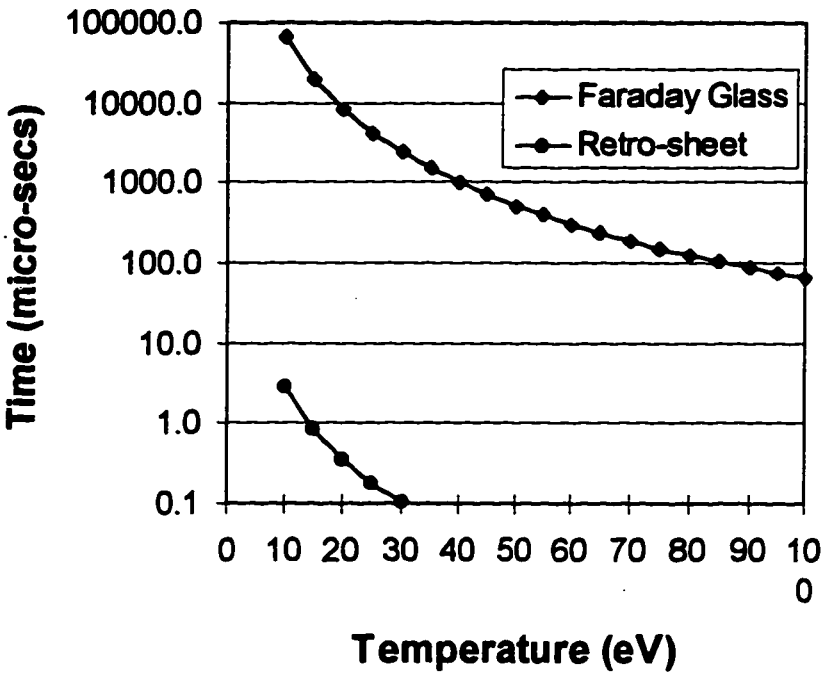


Figure 2.1 Time required to boil for unclad probe materials assuming plasma density, $n_e = 5 \times 10^{19} m^{-3}$.

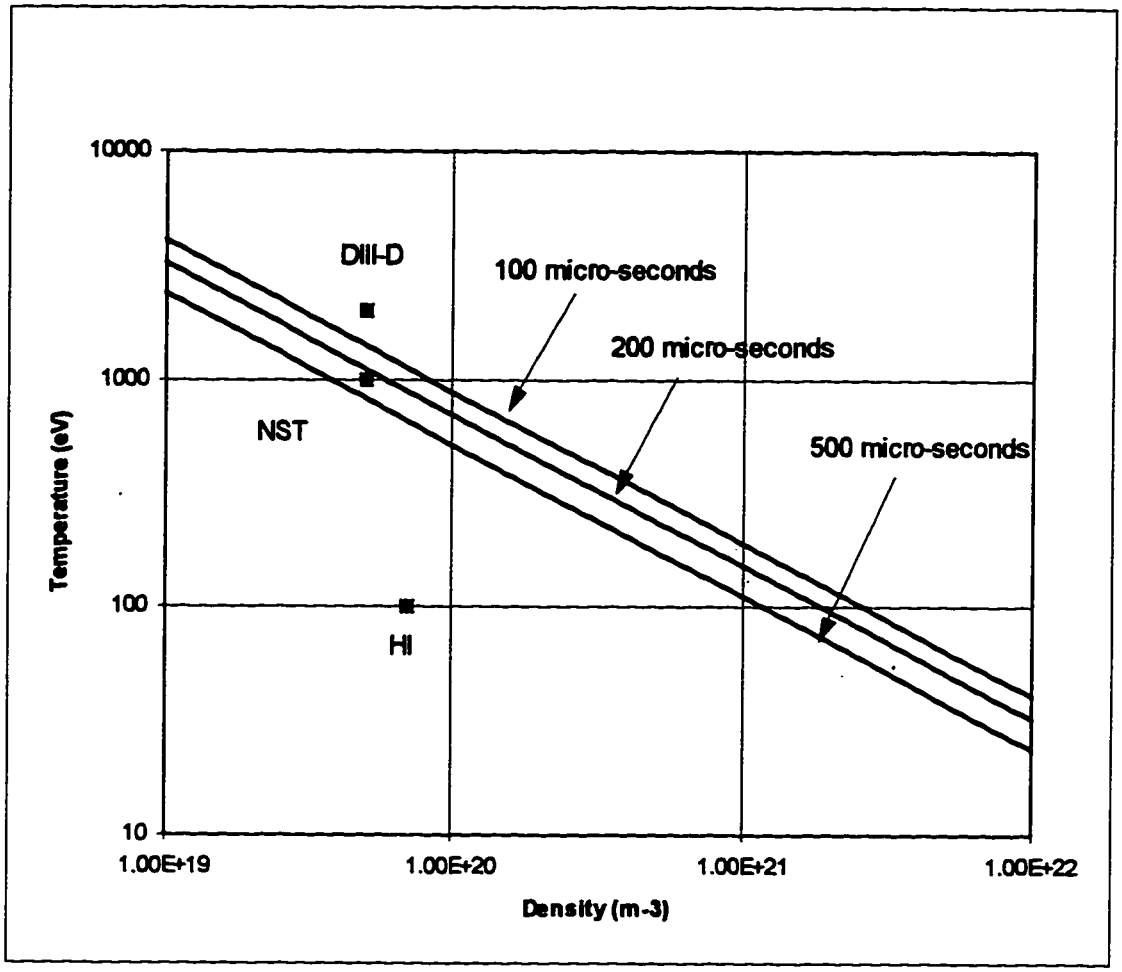


Figure 2.2 Plot of belief time for diamond clad probe as a function of plasma density and temperature.

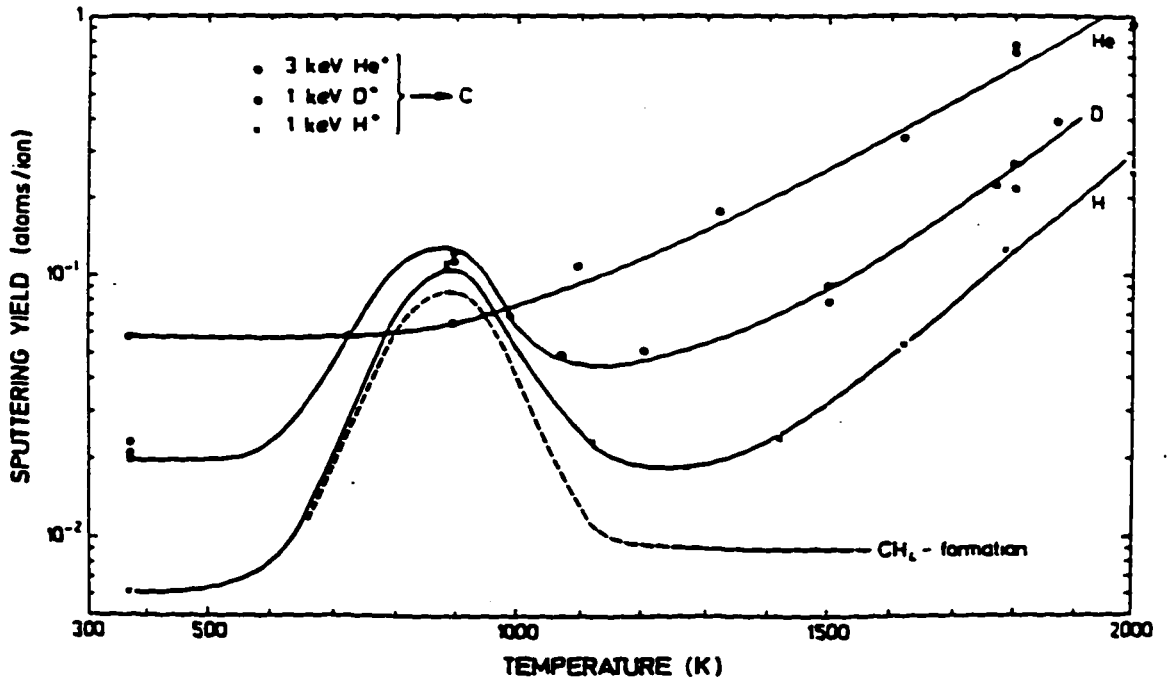


Figure 2.3 Plot of sputtering rate for graphite as a function of surface temperature.

## 3. Description of Diagnostic

### 3.1 Two Stage Light Gas Gun

The first component of the TIP diagnostic system is the probe accelerator. The design criteria for the probe accelerator included a target velocity of greater than 2 km/sec, compatibility with plasma vacuum environments, and high performance reliability and consistency. A two stage light gas gun was chosen to meet these requirements. A two stage as opposed to single stage gun was chosen in order to reach the required muzzle pressures of thousands of atmospheres without high pressure pumps and heating elements. Light gases are used as the accelerating gas because of their inherently higher sound speed which more efficiently accelerates projectiles. Light gases such as Helium and Hydrogen are also acceptable in a plasma environment because of their low Z number. Finally, gas guns have a long history of reliable and reproducible performance. A complete discussion of the design, construction and testing of the gas gun is included in reference [34].

#### 3.1.1 Description of Gas Gun

The TIP two stage gas gun is shown in figure 3.1. The essential components include the driver tube, pump tube, piston, and the two inserts. Operation of the gun is as follows: The aluminum bronze piston is positioned with the breech insert into the back end of the pump tube, covering two large holes which connect the "T" shaped driver tube with the pump tube. Following evacuation of both tubes with a vacuum pump, the driver tube is filled with nitrogen to nominally 1900 psi. The pump tube is then filled with helium to 73 psi. Piston o-rings prevent leakage between the systems.

Firing of the gun occurs when the firing valve is electrically opened. This valve connects the driver tube to the back of the piston via the breech insert.

Upon actuation of the firing valve, the 1900 psi driver gas pushes the piston forward uncovering large ports connecting the driver tube with the pump tube. This rapidly vents the driver tube into the pump tube and accelerates the piston down the pump tube. A Bridgeman seal on the nose of the piston seals the piston to the pump tube walls compressing the helium into the transition insert located at the end of the pump tube. As the pressure builds up the piston is decelerated and stops slightly short of the insert. The maximum breech pressure can be varied by adjusting the initial fill pressures. Typically a peak pressure of 35,000 psi is reached.

Holding back the high pressure is a diaphragm made out of 304 stainless steel. The diaphragm is scored to a pre-determined depth, such that it bursts at the proper pressure. Once the diaphragm breaks, the high pressure helium is released into the barrel accelerating the probe down the barrel. Instructions on how to prepare the diaphragm are included in appendix D.2.

### 3.1.2 Gas Gun Coupling System and Barrel

The barrel is joined to the pump tube via a differential threaded coupler which compresses the stainless steel diaphragm between two flanges as shown in figure 3.2. The coupler works by threading onto the pump tube at 8 threads per inch. Inside of the coupler, another flange threaded on the barrel at 9 threads per inch is backed off the barrel by friction. This works out to a tightening advantage of 72 threads per inch as the coupler is finally tightened. Two 36" jacking bars are used to easily provide the necessary closing force to compress the stainless steel diaphragm properly between the gripping flanges. This coupler was designed to replace a previous design in which the diaphragm was simply compressed between two large flanges which were bolted together. Though simple in operation, this method introduced perpendicular moments on the barrel as it was tightened and it was cumbersome to operate. The

differential system introduces no side forces which can alter alignment or bend the barrel.

The barrel for the gas gun is a custom made 68" long .50 caliber smooth bore barrel made of high strength heat treated alloy steel. The long barrel length was chosen to accommodate both acceleration of the probe and sabot removal. The sabot removal process, which is described in section 3.3.2, required vent holes to be symmetrically drilled in the barrel to vent the high pressure helium. A small tank, sealed with sliding o-ring seals was mounted on the barrel to collect the vented helium and control the atmosphere and pressure inside the barrel. A clamping ring and flange is located on the end of the barrel which seals a mylar diaphragm with an o-ring to form a vacuum barrier between the barrel and the expansion tank. Finally, the barrel is mounted to the expansion tank with a flexible bellows coupling and sliding o-ring seal. This insures that virtually no moment is exerted on the end of the barrel. Figure 3.2 shows the barrel with the auxiliary tank and the mylar diaphragm holder mounted.

### 3.1.3 Description of Gun Control Systems

Pressurizing, firing, and venting of the gas gun was done remotely using an electro-pneumatic control system. Figure 3.3 provides a diagram of the gas gun control system and gas supply network. Once the gun is pumped down, the gun room is evacuated and operation is directed from the control panel. The procedures for operating the gas gun are included in appendix D.

The firing sequence described in appendix D ends by opening the first of two firing valves in series as shown in figure 3.3. At this point, actual firing of the gun is turned over to the tokamak control system that uses an optical trigger to send a pulse to an electrically actuated stepper motor. The stepper motor is coupled directly to the shaft of a high pressure ball valve, preset a few degrees away from the open position. At firing, the motor accepts a 5-15 volt pulse and

rotates to full open in a few milliseconds, thus firing the gun. An interlock system blocks the firing signal from occurring unless the vacuum pressure is acceptable in both TIP vacuum systems and unless the tokamak isolation valves are open.

## 3.2 Faraday Probes

### 3.2.1 Probe Description

The probe package is quite simple in composition, consisting of three separate parts; the faraday glass, the sabot, and the retro-reflector. Figure 3.4 shows the three components assembled together to form the sabot/probe payload that is accelerated in the gas gun. Several faraday glass materials were considered and discussion of those materials is presented in section 3.2.2. Dimensions of the probe were chosen to maximize performance of the probe while minimizing the size of the probe. The probe face dimensions were chosen as a compromise between maximizing the aperture to collect light from the laser and keeping the probe small enough to fit into the sabot and have sufficient margin to deflect the sabot without touching the probe. The size chosen was 4mm x 4mm. These dimensions are ground by hand such that variation in the diagonal length is less than 12 microns. As shown in equation 2.3 the magnetic resolution of the probe is directly proportional to the probe length, consequently a long probe is desirable. However, spatial resolution of the probe is inversely proportional to the length. Ultimately probe length was limited to be one centimeter in order to keep spatial resolution on the order of a centimeter. The resulting magnetic resolution of the probes is then 16 gauss assuming the ability to measure the polarization angle within 0.3 degrees.

The purpose of the sabot is to protect the probe during acceleration inside the breech. Polycarbonate (LEXAN®) was chosen for the material because of its superior strength, light weight and ease of machining. Each sabot

is precisely machined to better than 12 micron accuracy in order to insure sufficient reproducibility between shots.

Retro-reflection of the illuminating laser light is achieved by attaching a sheet imbedded with micro-corner cubes to the rear of the probe. These sheets are made by the Reflexite Corporation and are normally used to enhance the reflective properties of street signs. The material was found to have good reflective properties and was able to withstand the high compression forces during acceleration without significantly altering the reflectance properties of the sheets. Unfortunately, the material did have some drawbacks. A divergence of 15 degrees was built into the sheets to optimize the reflectance for drivers viewing at small incidence angles. Additionally, upon reflection, the sheets make linearly polarized light slightly elliptic. The ellipticity effect on the polarization measurement is somewhat mitigated in the calibration process. But, this non-ideal behavior does have a deleterious effect on the overall accuracy of the diagnostic. Detailed procedures describing probe fabrication are included in appendix A.

### 3.2.2 Faraday Rotator Materials

The properties of the faraday rotator material ultimately determine the size and accuracy of the probe. Ideally the material should be amorphous, highly linear, have the highest verdet constant possible, and be able to withstand the acceleration process in the gas gun. Several materials were considered for probes. Table 3.1 shows the various materials considered and their properties. The first two columns are terbium doped borosillicate glasses which are common materials used to make isolators for lasers.

Table 3.1 Probe Materials

| Company | *Hoya* | *Kigre* | *Litton-Airtron* | *Infrared Tech.* |
|---|---|---|---|---|
| | | | | |
| Product name | FR-5* | M-32* | TGG* | CdMnTe** |
| verdet coeff (deg/cm g) | 0.00716 | 0.0095 | 0.012 | 0.17 |
| Index of Refraction | 1.688 | 1.727 | 1.976 | 2.6 |
| Density($g/cm^3$) | 4.28 | 4.33 | 7.26 | 6.2 |
| Type of material | glass | glass | crystal | crystal |
| Availability | easily | easily | easily | rare |

*Values listed are for $\lambda$=514 nm

**Values listed are for $\lambda$=632 nm

M-32 was used most widely because it has the highest verdet constant of the amorphous glass materials which were conveniently machined and withstood acceleration quite readily. Improvement in the verdet performance of the glass can be obtained by using a shorter wavelength illumination laser. Figure 3.5 shows the wavelength dependence of the Verdet coefficient for FR-5. The amount of improvement is limited by the transmission performance of the glass which drops rapidly to nil below 400 nm. Additionally, a strong absorption region exists between 475 and 500 nm. This is typical of terbium doped glasses and precludes the use of the strong Argon laser line at 488 nm. Consequently the 514 nm line was used.

Krypton ion lasers provide the best available continuous wave solution at these wavelengths. Krypton has a 406 nm line that would improve the verdet constant of M-32 by a factor of 1.8 relative to the 514 nm line used for this experiment.

CdMnTe has an exceptional verdet constant and allows more options for choice of illuminating laser since it transmits light in the red portion of the spectrum. Unfortunately, the material is quite rare and expensive. Experiments were conducted to evaluate the transmittance and verdet coefficient of the

material.. Results of the tests were unsatisfactory as the material appeared to be quite birefringent. Transmission was not as good as the terbium glasses, but acceptable for probes that were anti-reflection coated. The birefingent conclusion may have been tainted by the use of an unsilvered corner cube to return the light to the detection system. Further tests should be conducted to confirm the birefringent behavior. Handling of the material proved difficult also. Cadmium is a hazardous material requiring special handling during cutting and grinding. Additionally, the material is quite brittle and unlikely to survive acceleration in the gun without additional care, although no test shots were conducted.

Terbium Gallium Garnet (TGG) appears to be a strong substitute candidate material. Like the amorphous glasses, TGG's verdet coefficient improves with shorter wavelengths, such that a TGG probe at 406 nm would have a verdet coefficient improvement of 3 over present M-32 probes at 514 nm. Acceleration tests using the gas gun were conducted by firing hand ground undoped garnet 'dummy' probes. They did not withstand the acceleration process. Properly cut probes with improved sabot designs may permit use of garnets as probes. In any choice of material, significant lead time to obtain the material should be anticipated. Typically, a minimum of three months is required to procure the material and additional time is required to cut and fabricate the probes.

## 3.3 Gas Interface System

### 3.3.1 System Overview

The gas interface system serves three primary functions. First, it removes the probe from the sabot allowing only the probe to enter into the plasma. Second, the system provides the means for transition between the mega-torr pressure regime of the gas gun and the micro-torr regime of the plasma

chamber. Finally, it holds the mirrors which link the probe to the optical detection system and provides the means to contain the debris created as the probe hits the breakable mirror and comes to rest.

The gas interface system is comprised of three parts: the sabot removal section, the expansion tank, and the catch tube assembly. Once the gun has fired, the probe and sabot travel down the barrel into the sabot removal section housed in the auxiliary tank where the sabot is axially separated from the probe using a technique called "gas dynamic stripping." The now separated probe and sabot enter the expansion tank which stops the sabot and muzzle gasses, while allowing the probe to travel into the plasma via a long pipe. Upon exiting the plasma chamber, the probe enters the catch tube and finally crashes into the breakable mirror that is used to illuminate the probe. Ultimately, a removable stainless steel container collects the destroyed probe and mirror.

### 3.3.2 Sabot Removal

Removal of the sabot prior to entering the plasma chamber is required to prevent contamination of the plasma from rapid ablation of the plastic sabot. Critical to sabot removal is that it must be done without tilting the probe. Developing an effective sabot removal technique that did not induce instabilities to the probe proved to be the most difficult process in the development of the TIP diagnostic. A two step process was used to achieve this.

As described previously, approximately midway down the barrel length, the auxiliary tank surrounds the symmetric vent holes drilled into the barrel. The end of the barrel is sealed with a 0.0005" thick mylar diaphragm. This arrangement allows the barrel to be filled with nitrogen to the desired stripping pressure. The manner in which axial stripping occurs is shown in figure 3.6. The probe/sabot package travels down the barrel developing a high pressure shock wave in front of the projectile. As the package clears the vent holes the

muzzle gas from the gun is vented from behind the probe. A large differential pressure is felt by the sabot which seals with the barrel. The probe feels no net force since it is a square shape in a round hole thus allowing the pressure to equalize around it. Consequently the sabot is decelerated relative to the probe resulting in axial separation.

Once axial separation has occurred, an angled plate deflects the larger sabot off line while allowing the probe to pass unaffected. This plate is housed in the expansion tank. A photograph of the probe with a deflected sabot following it is shown in figure 3.7.

Many factors affect the performance of the stripping process. The most critical parameters are auxiliary tank fill pressure, probe weight and density, sabot weight, the barrel venting rate, and to a lesser extent, the tightness of the probe to sabot. The criteria for sabot stripping is that the probe be consistently separated completely from the sabot and maintain less than $10^0$ tilt 4-5 meters down range. Ideally, the fill pressure should be as low as possible since increased fill pressure reduces probe velocity. Additionally, probe stability was observed to be improved when the stripping distance between the end of the sabot and rear of probe was on the order of 1-2 centimeters or less. This limit must be approached carefully since failure to fully separate results in the probe being deflected with the sabot causing significant damage to the fast valve. Section 4.2.2 gives a summary of results obtained in developing the sabot removal technique.

### 3.3.3 Expansion Tank

A 1000 liter expansion tank forms the vacuum boundary separating the gun and plasma chamber. Figure 3.8 shows the expansion tank which is comprised of two compartments. The first compartment is a small tank which mates with the barrel. A sliding o-ring bellows connection forms the vacuum seal with the outside of the barrel. The mylar diaphragm discussed earlier is

housed in the small tank. Mylar was chosen because it is has high strength and it is transparent, thereby permitting alignment of the barrel during pump down. Approximately 8 inches downrange from the barrel is a one inch thick aluminum wall with a 3/4 inch diameter hole in it which allows the probe and sabot to pass. This wall acts as a baffle and supports the deflector plate discussed previously. A second partial baffle is located 6 inches from the deflector plate to further impede the flow of muzzle gases. The far wall of the tank supports the fast valve and sabot catcher and acts as another baffle.

A fast valve is used to limit the amount of muzzle gas entering the plasma chamber. The valve is shown in figure 3.9. A thin wire pulls back against a spring loaded aluminum door. Actuation of the valve is achieved by the deflected sabot crashing into the restraining wire a mere 15 to 20 micro-seconds after the glass probe has left the chamber. When the wire is broken this door slams shut against a viton o-ring seal effectively preventing muzzle gas from entering the plasma chamber. A slower electro-pneumatic valve down stream of the fast valve then shuts providing the required hard vacuum integrity.

Performance of the expansion tank system was excellent. Base pressure was maintained at approximately $1 \times 10^{-6}$ torr. Fast valve closing time was less than 5 msec. The most significant measure of performance was the amount of gas allowed to enter into the plasma. This was measured to be less than 0.4 torr-liters. Operation with the high vacuum environment of the tokamak showed no significant changes in plasma performance or base pressure.

### 3.3.4 Description of Catch Tube Assembly

The last major component of the gas interface system is the catch tube assembly. It links the optical detection system with the plasma and collects debris from the probe following impact with the breakable steering mirror that is housed within the catch tube. Figure 3.10 shows the catch tube assembly. The catch tank supports the turbo-molecular pump and provides a view port for

photographing the probe. The laser is admitted into the tube via a welded tube. The tube is angled at 30 degrees off the probe flight axis in order to keep the incidence angle of the laser on the breakable mirror small. This minimizes degradation of the linear polarization. An insert in the tank holds a 1 1/2 " square breakable mirror at a fixed angle of 15 degrees off axis, providing rough alignment of the laser down the flight path of the probe. Two steerable mirrors outside the vacuum boundary provide fine alignment control, such that the beam is coincident with the path of the probe. Finally an angled cylinder with a protective inner sleeve, mounted with quick release o-ring seals, catches the pulverized glass from the sabot and mirror. The system has performed admirably. Vacuum baseline pressures of less than $10^{-6}$ torr are easily achieved. Glass removal and cleaning is done using a vacuum cleaner followed by an alcohol rinse. "Turn around time" for the system is 15 minutes. Pump down to base pressure takes approximately 90 minutes.

## 3.4 Optical Detection System

### 3.4.1 Discussion of Optics

The optical detection system serves two purposes. First, it delivers linearly polarized light to the probe. Second, it collects the reflected light and determines the amount of faraday rotation. Once the faraday rotation is determined, the magnetic field profile is obtained by equation 2.3.

Figure 3.11 shows the top view of the optical detection system. Light at 514 nanometers from an argon ion laser is expanded to approximately 1 cm in diameter and passes through a vertically oriented linear polarizer. It then travels through a beam splitter and onto the steering mirrors described in the previous section. A portion of the expanded beam goes through the probe and is retro-reflected back to the optical detection system. The entrance beam splitter then directs the beam through a narrow band filter and focusing lens. A thirty percent

reflective beam splitter further directs a portion of the light to detector one and a fifty percent splitter divides the remaining light between detectors two and three such that the incident intensity on each detector is nearly equal.

The detectors are shown in figure 3.12. Each consists of an aluminum cylinder with a linear polarizer on the front and a photodiode in the rear. Adjustable mounts provide five degrees of freedom to position each detector in the center of the beam. The linear polarizers are oriented to minus sixty degrees, zero, and plus sixty degrees relative to vertical for detectors one, two, and three respectively. The polarizers act as analyzers which preferentially pass light of a given polarization state to the photo-diode, such that the voltage output of the photo-diode is related to the polarization of the reflected light incident on the detector. Power for the detectors is provided by 9 volt batteries to minimize electro-magnetic noise in the signals. Noise and background light are further reduced by housing the entire system in a 3/8" thick aluminum box. Section 3.4.2 discusses the data analysis in more detail and Appendix B describes the alignment and calibration procedures in detail.

### 3.4.2 Calibration of the Optical Detection System

The polarization angle of the reflected light is the fundamental quantity measured by the TIP diagnostic. Ultimately, the accuracy of the magnetic field measurement is dependent on measurement of the probe position and orientation, as well as the measurement of the polarization angle. This section discusses the polarization angle measurement.

Ideally, for linearly polarized light each detector output should follow a cosine squared function given below

$$I_i = IA_i \cos^2(\psi - \alpha_i) + I_{zero} \qquad \text{Eq. 3.1}$$

where I is the reflected intensity on the detection system, $A_i$ is the relative fraction of power delivered to each detector , $\psi$ is the incident polarization

angle, $\alpha_i$ is the offset angle of the linear polarizer, and $I_{zero}$ is the detector zero intensity offset voltage. This function is periodic every 90 degrees and it is quite insensitive when the polarization argument is near zero and 90 degrees. Consequently, three detectors with polarizers offset at sixty degrees are used. This insures that one detector is always operating in a sensitive region and increases the periodicity to 180 degrees.

Calibration involves inputting light of known polarization into the detection system and normalizing the signals, so the values of $A_i$, $\alpha$,and $I_{zero}$ for each detector can be determined. As discussed in reference [35], interaction between the optics and the illuminating laser lignt results in the light becoming slightly elliptic. The most serious offender being the corner cube retro reflector sheet. This problem is addressed through a combination of changing the detector intensity model and through the calibration procedure.

First, the detector intensity model described by equation 3.1 is replaced by an arbitrary 9$^{th}$ order polynomial function given by the equation

$$I_i = I \sum_{n=0}^{9} a_n x^n . \qquad \text{Eq. 3.2}$$

This allows more flexibility in fitting the detector responses to calibration data. Second, the calibration procedure attempts to simulate as near as possible, the optical conditions present during an actual free flying measurement. This is done by calibrating the system with a faraday probe in a location in the flight path of the probe such that non-ideal behavior of the retro-sheet and steering mirrors are taken into account.

Briefly, calibration of the system then proceeds as follows. First, the optical detection system is aligned according to appendix B. A half-wave plate is then installed between the beam expander and first beam splitter. The half-wave plate is then rotated in precise two degree increments causing the input polarization to rotate 4 degrees. The input polarization is rotated through 360

degrees and the detector output voltages are recorded. These data points are later averaged to provide one voltage for each 4 degree increment. The laser beam is then blocked and an additional data point set is recorded to determine the detector voltage offsets. These offset voltages are subsequently subtracted from all previous signal readings.

Once the offsets have been subtracted, the detector voltages are normalized by dividing each detector voltage by the sum of all three detector voltages. This normalization procedure is done to account for variations in reflected power from the probe. The calibration data points fit with a $9^{th}$ order polynomial curve are shown in figure 3.13. These curves closely approximate the ideal cosine squared curve of equation 3.1, but evidence of ellipticity is clearly present since the detector response curves do not zero. All of the data reduction required to generate the calibration curves and polynomial coefficients is done using the program "JPOLAR.PRO" which is included in Appendix B along with the formal calibration procedure.

### 3.4.3 Optical Detection System Data Analysis

Once the coefficients for the individual detector response functions have been determined, the Optical Detection System is ready to measure an unknown input polarization. Essentially the calibration process is reversed. Offset voltages are measured just prior to a shot. The shot is taken and the offset voltages are subtracted from the detector voltage data which are then subsequently normalized by dividing each signal by the sum of all three. The normalized voltages are then fit to the calibration curves using a least squares method to determine the polarization state of the reflected light. The program "MAG.PRO" in Appendix E performs this process. Reference [35] provides a more in-depth discussion of the code. Bench tests of the system in which known polarization states where input into the system showed the system to have an uncertainty of approximately $0.3^0$.

The $0.3^0$ uncertainty is observed under ideal conditions in which the probe face is normal to the illuminating laser, the probe is stationery , and the reference polarization state is input with a half-wave plate. Further discussion of the system uncertainty is required in order to understand the results presented in chapters 4 and 5. Calibration of the system is also done under the ideal conditions just described. Three factors affect the measurement under flying conditions, variation in reflected scattered light intensity, probe rotation and probe tilt. Normalization of the detector signal can account for the large variations in reflected intensity, but it does not account for changes in the proportion scattered light received at the detector relative to the overall signal. If background light remains small relative to the overall intensity the affect is minimal. This will be the case if the probe remains centered in the illumination beam. In this situation the polarization fraction, defined as the ratio of polarized reflected light to unpolarized scattered light, remains constant or increases as the probe approaches the detection system. In the event the probe tilts or passes out of the illumination beam, the polarization fraction decreases resulting in significant drift in the measured polarization angle. This effect was tested by pushing a TIP probe down a track designed to maintain precise alignment. The result showed that for constant or increasing intensity profiles, the variation in measured polarization angle was negligible. Figure 3.14 shows the variation to be less than 0.25 degrees over 3 meters. But profiles in which the intensity drops significantly results in excessive drift in the measured polarization angle. As much as 8 degrees of drift was observed in shots taken where the light intensity profile was decreasing significantly. This magnitude of drift in the polarization is not understood and remains as a question for future research. Consequently, data obtained during shots when the intensity is dropping is highly questionable.

Another source of uncertainty is probe tilt and rotation. During flight some tilt in the probe occurs and the probe can rotate about the long axis of the probe.

Bench measurements using the track described above, in which the probe and retro-reflector sheet are rotated show variations in the measured polarization angle of up to $1.8^0$. Figure 3.15 shows the result of such a test in which the periodic rotation of the probe is observed in the signal. As the angle of incidence deviates from normal, this effect becomes more pronounced.

Finally, the calibration procedure itself is somewhat problematic. As the different polarization states are input from the half-wave plate different magnitudes of ellipticity are introduced. This is due to the different response of the steering mirrors and beam splitters to different incident polarizations. For actual measurements, the input polarization is held constant in the P state and rotation occurs within the probe. Only on the return path are the varying incident polarization angles encountered by the steering mirrors and beam splitter. This effect is small relative to the previously mentioned uncertainties, but does have an effect.

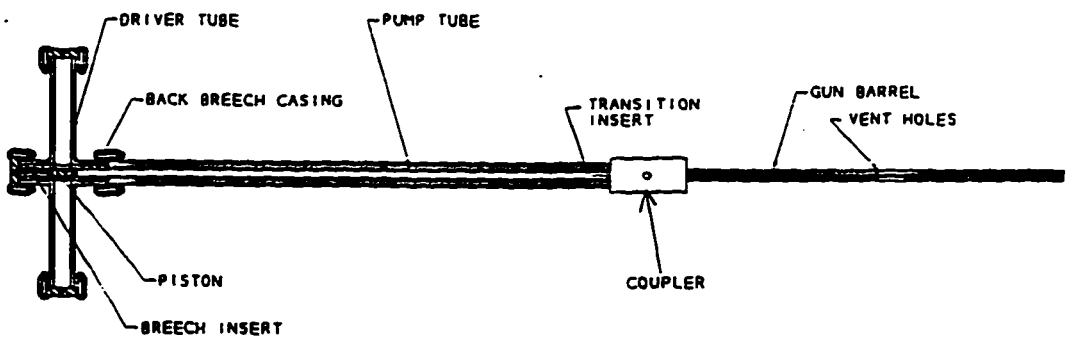


Figure 3.1 TIP Two Stage Light Gas Gun.

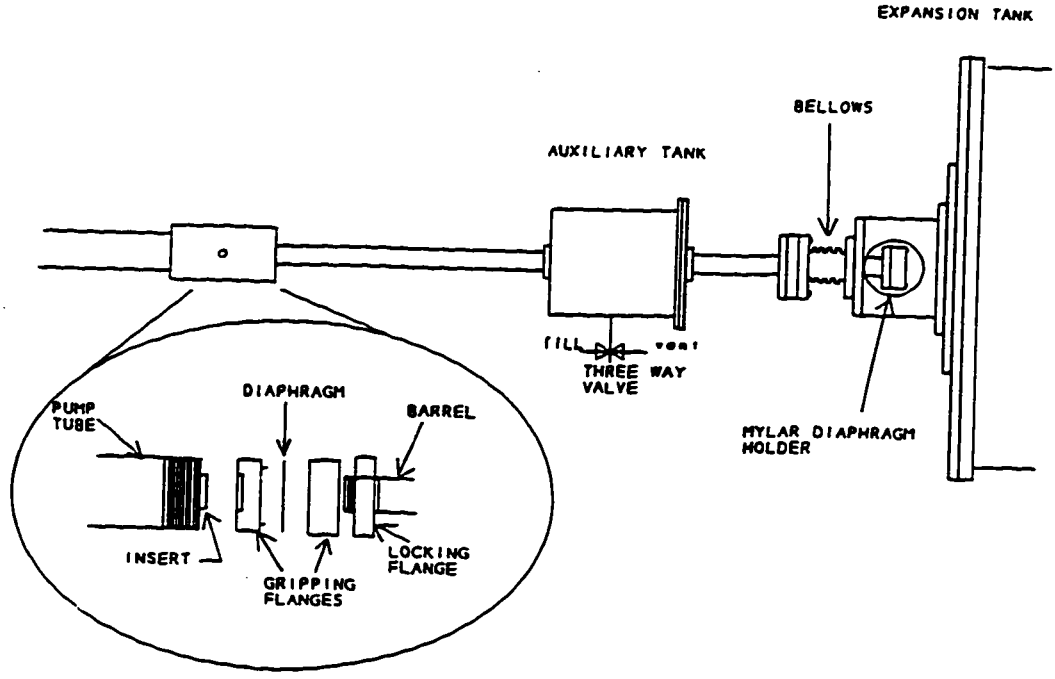


Figure 3.2 TIP barrel components showing axial locking joint, auxiliary tank and sliding bellows connection with mylar diaphragm holder in place.

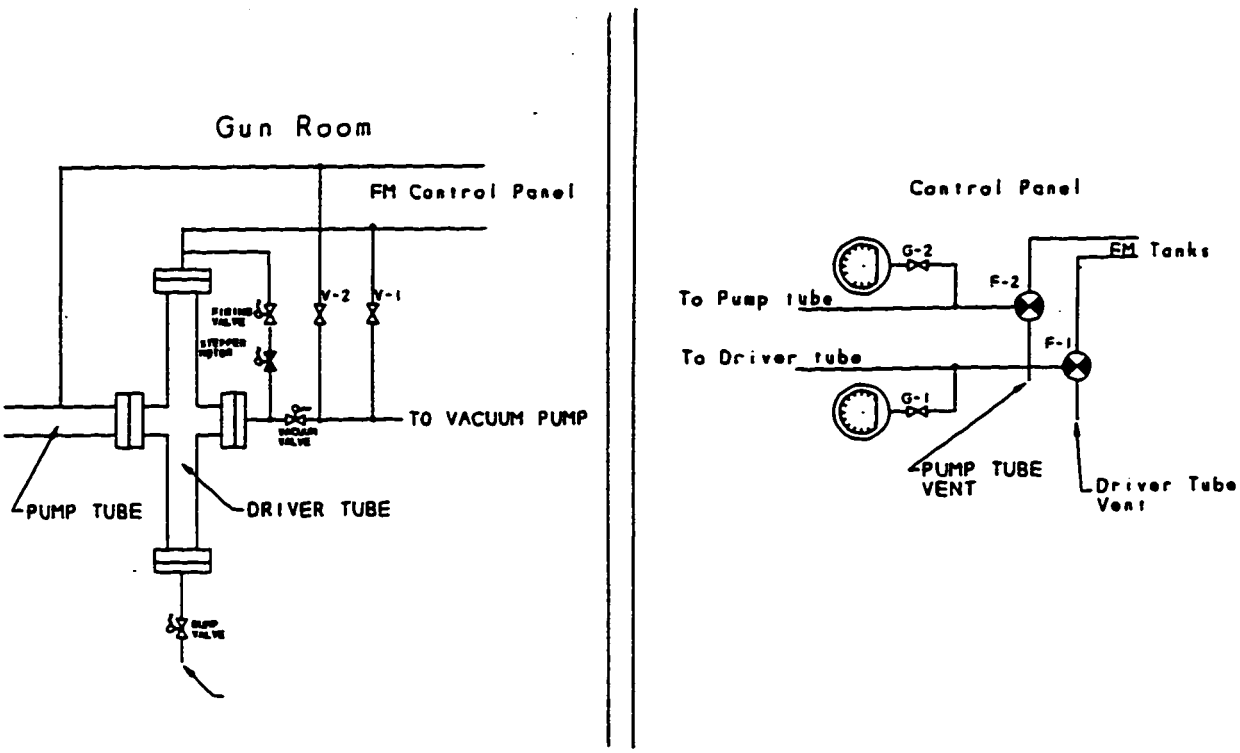


Figure 3.3 TIP gas handling system showing control panel valves and gas gun control operating valves and gas line connections.

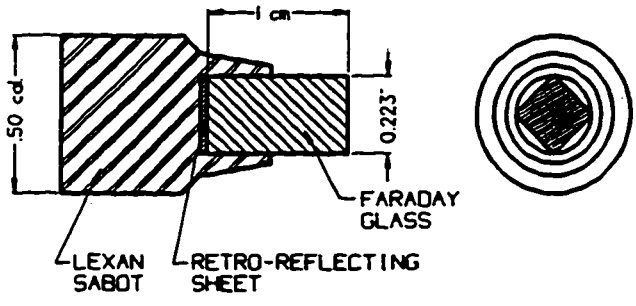


Figure 3.4 Diagram of Faraday rotator probe and sabot.

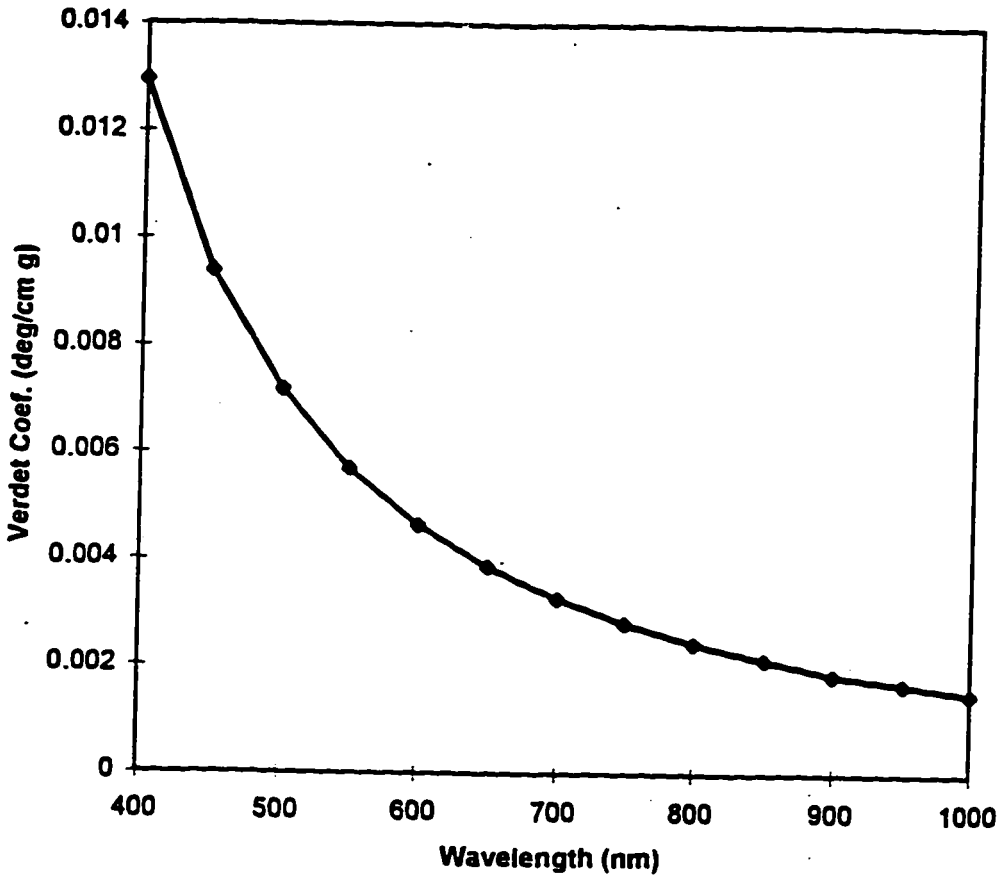


Figure 3.5 Graph of verdet coefficient as a function of wavelength.

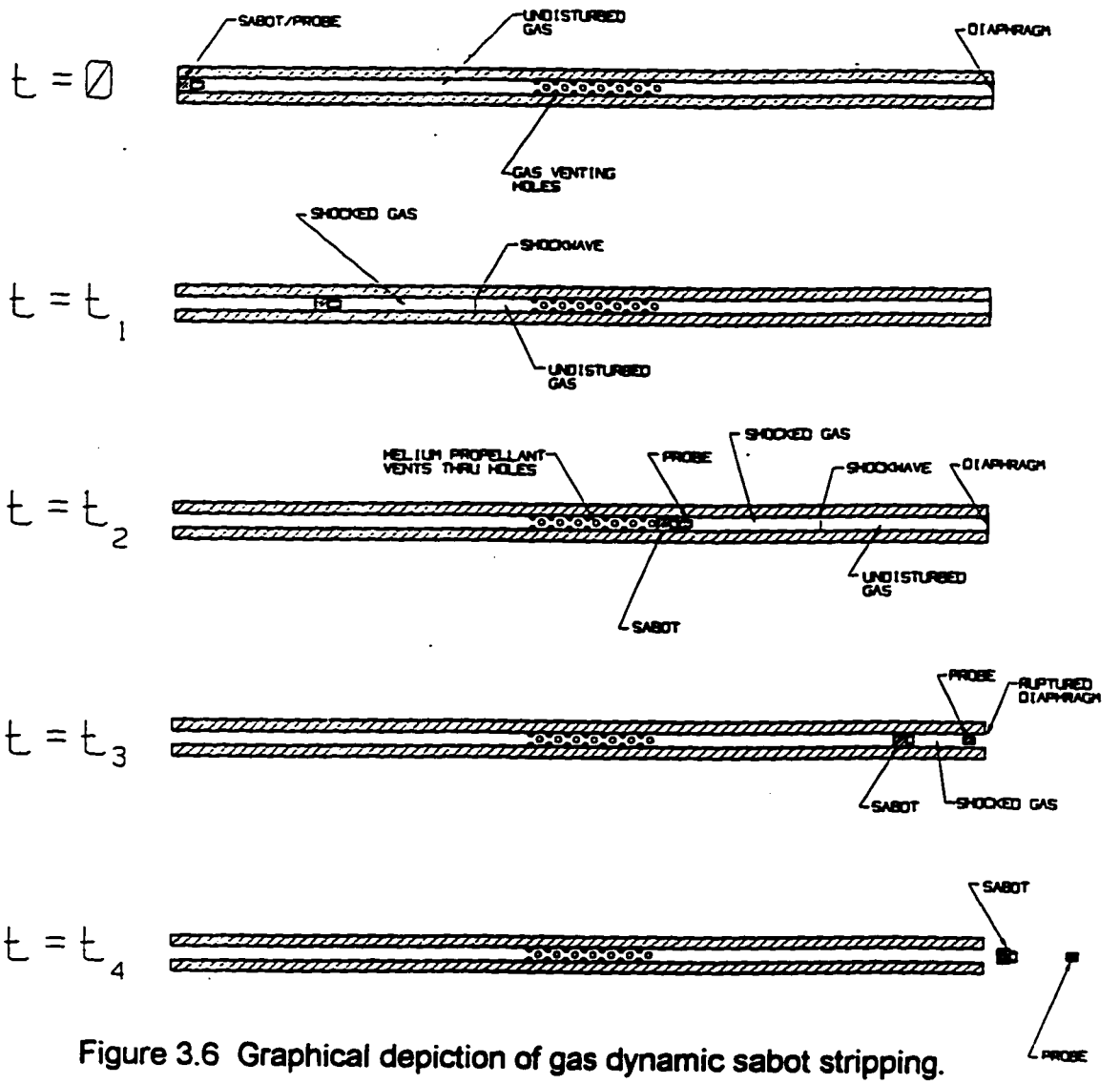


Figure 3.6 Graphical depiction of gas dynamic sabot stripping.

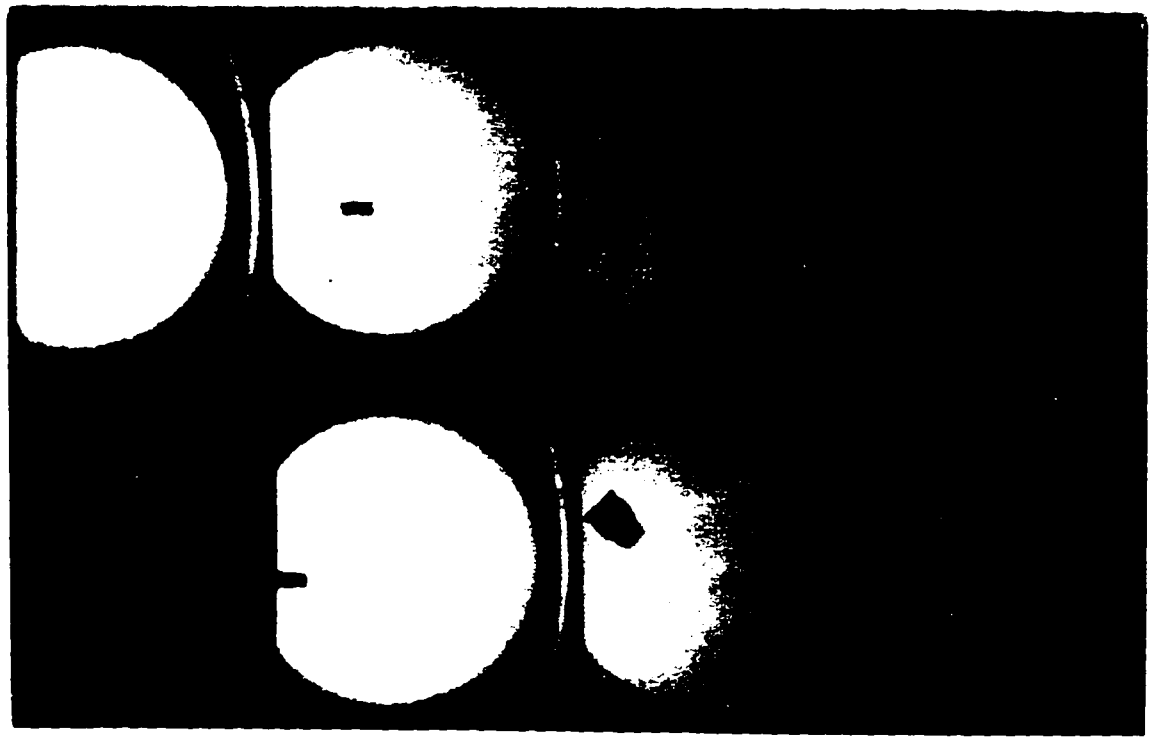

Figure 3.7 Photograph of deflected sabot trailing TIP probe.

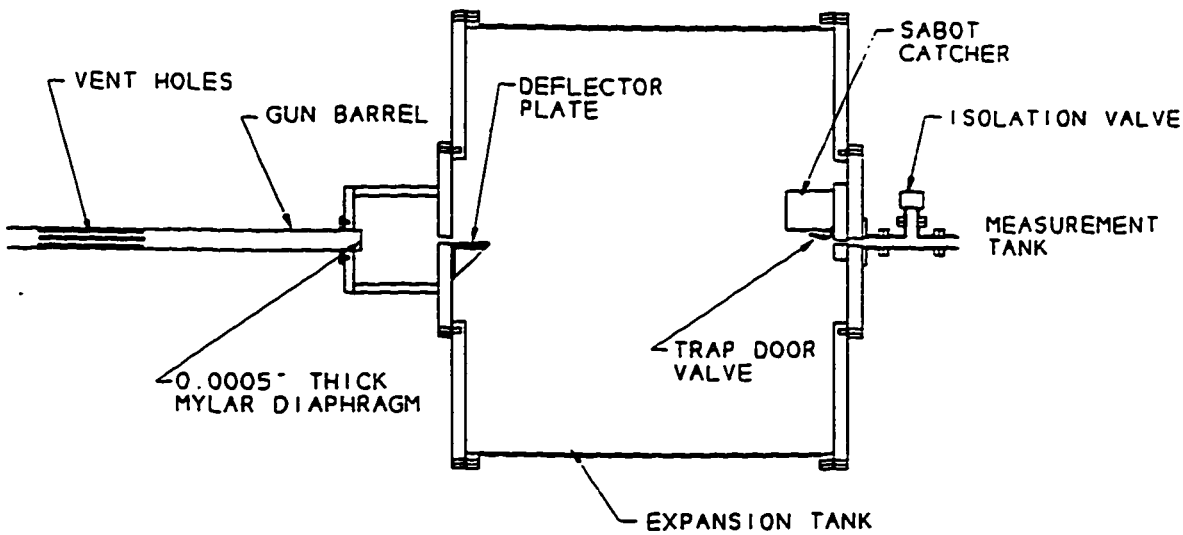


Figure 3.8 Diagram of expansion tank.

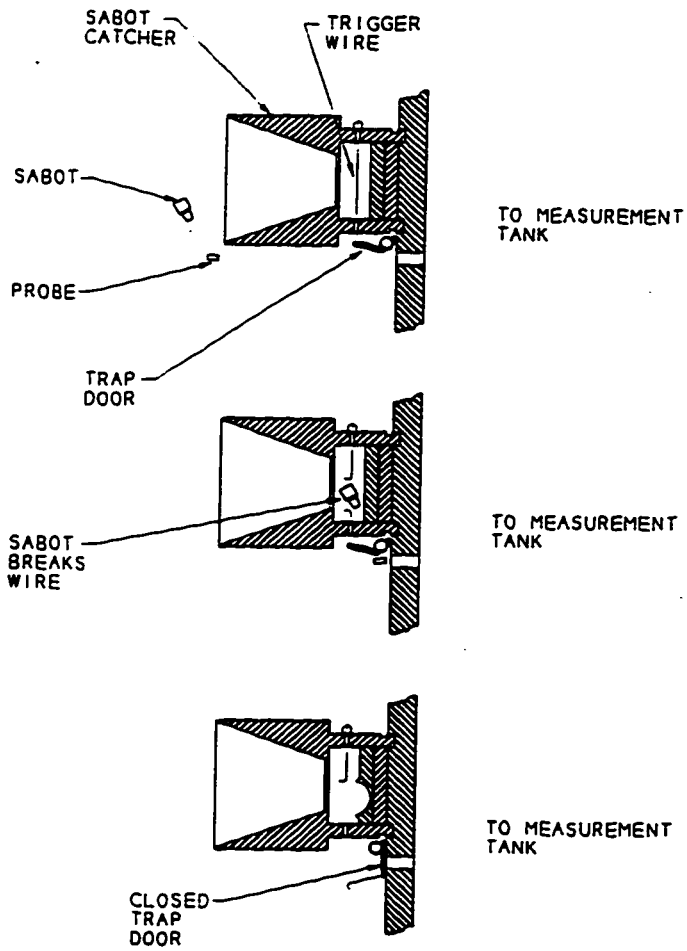


Figure 3.9 Sabot actuated fast valve.

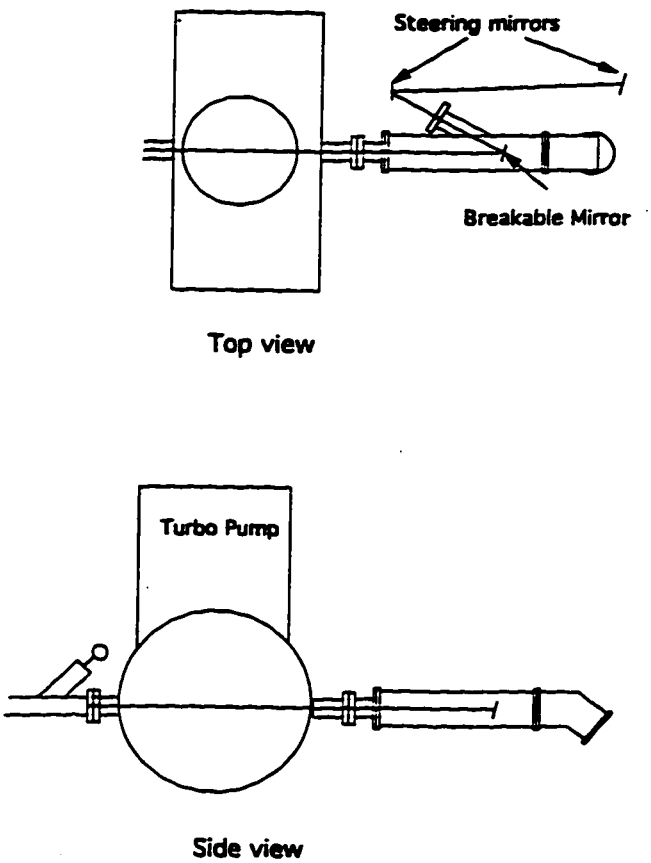


Figure 3.10 Catch tank assembly.

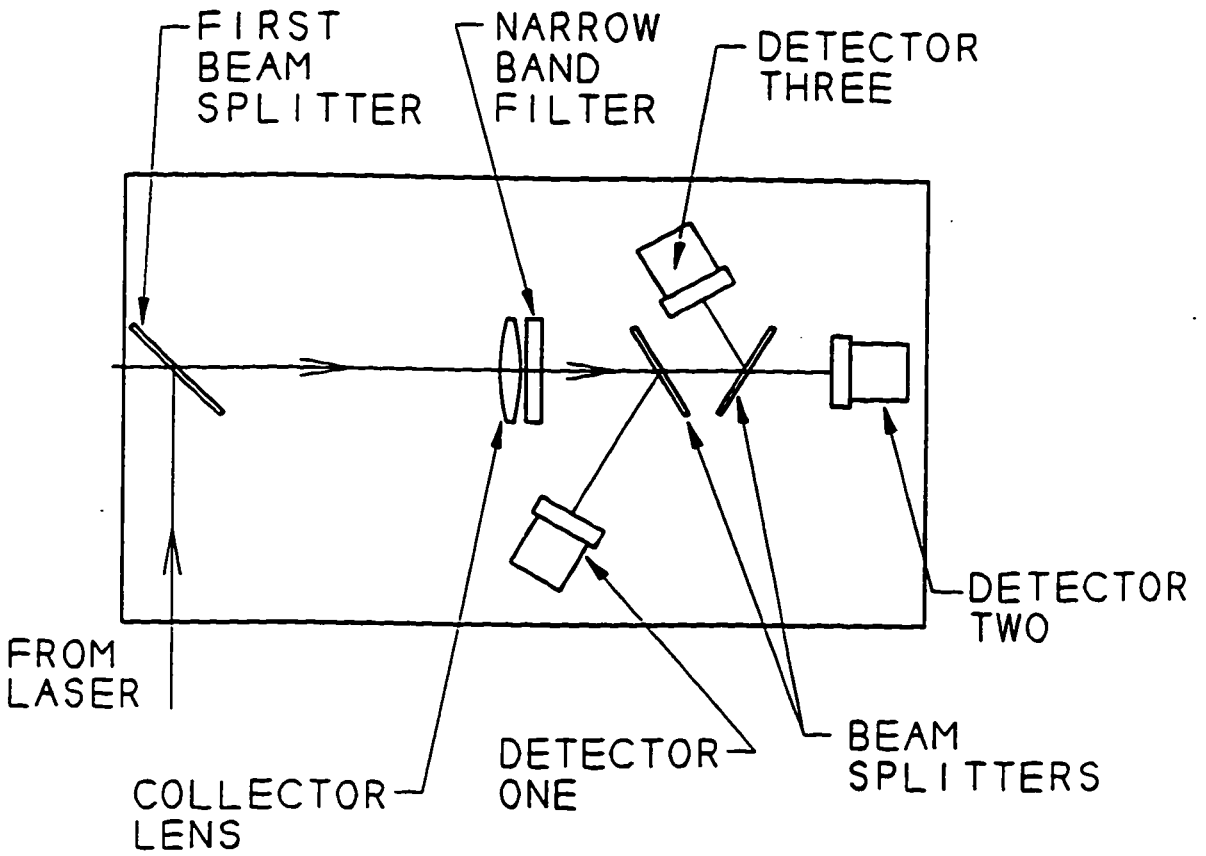


Figure 3.11 Top view of the optical detection system.

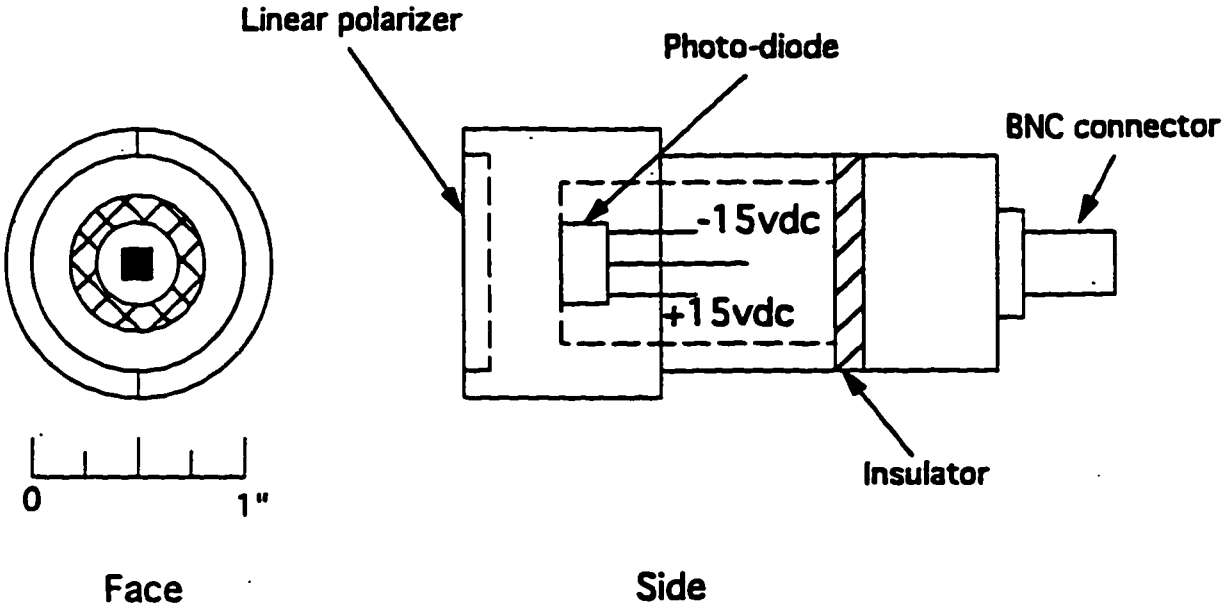


Figure 3.12 Drawing of detector.

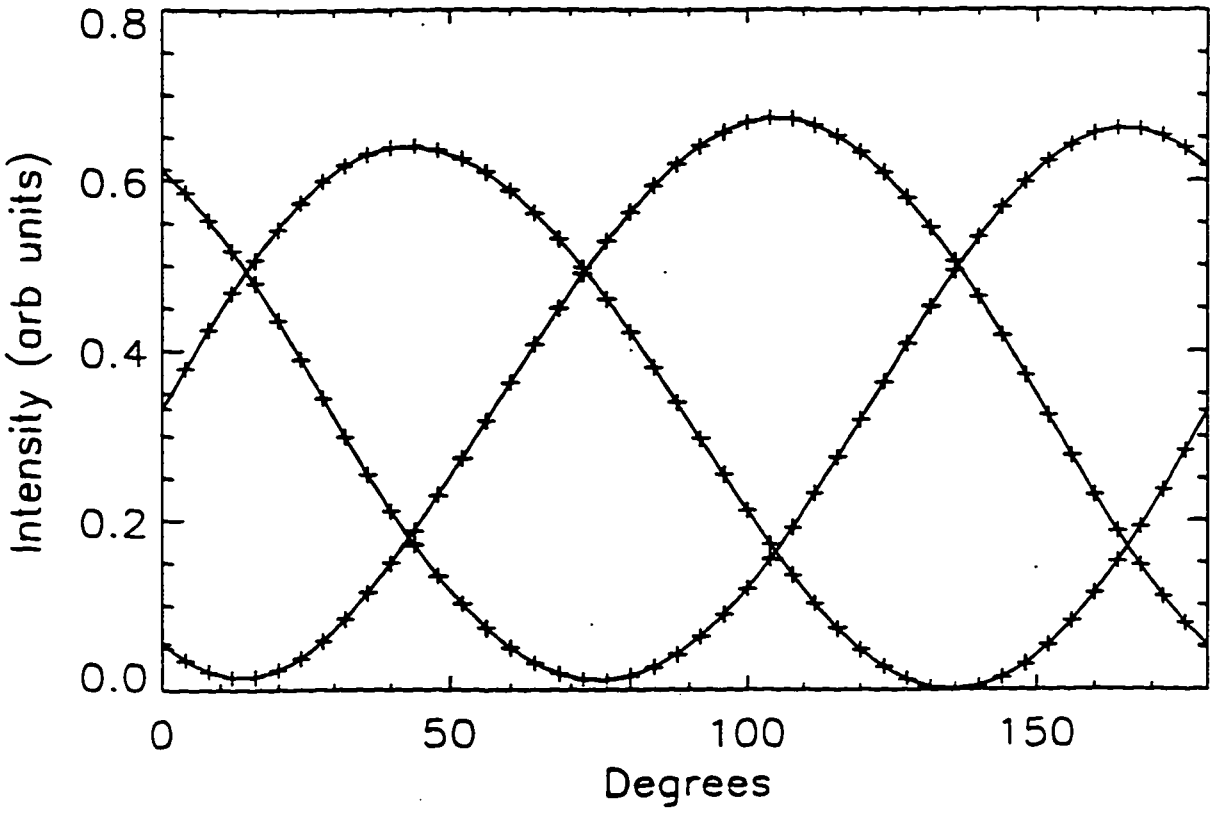


**Figure 3.13 Optical detection system calibration data plotted with 9th order polynomial curve fits.**

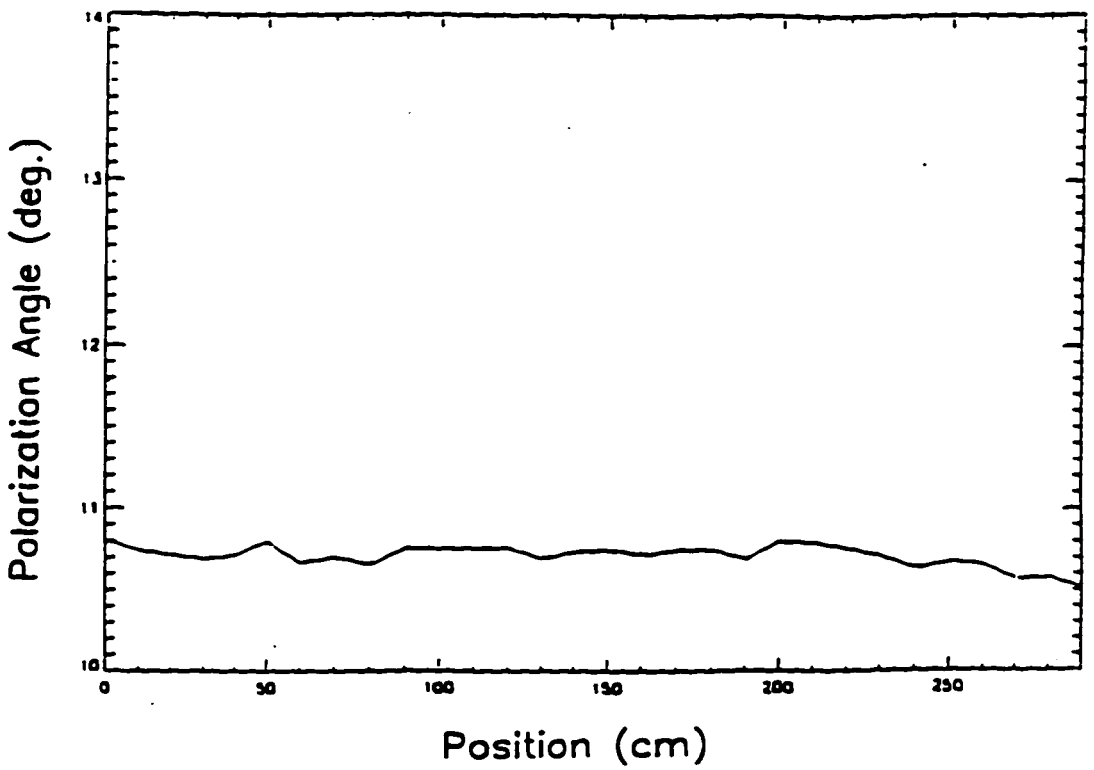


Figure 3.14 Variation in measured polarization angle for a fixed input polarization as a function of distance from optical detection system.

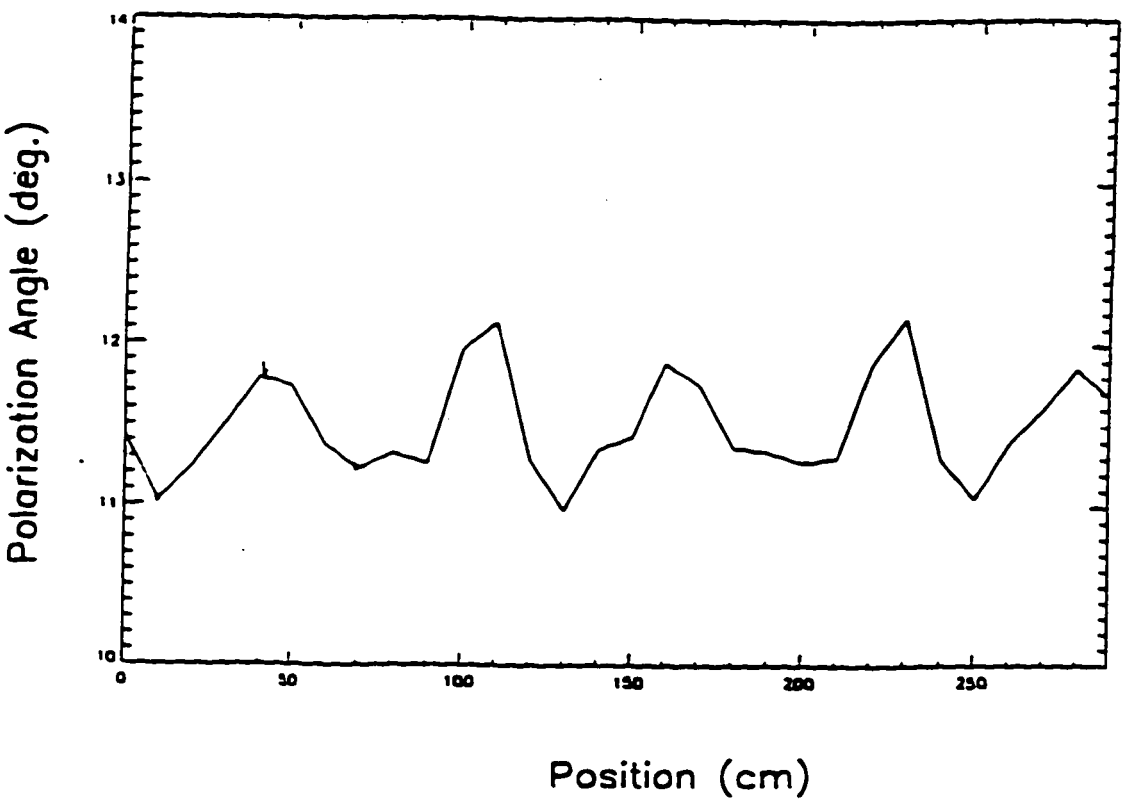


Figure 3.15 Variation in measured polarization angle for a probe rotated axially $30^0$ every ten centimeters of motion.

## 4. Diagnostic Operational Results

### 4.1 Gas Gun and Gas Interface System Performance

#### 4.1.1 Summary of Gas Gun Performance

Gas gun operation remained quite consistent throughout hundreds of shots taken over a 4 year period. Some significant modifications were made, however, to improve performance and facilitate launching optical probes. Initially a .30 caliber barrel intended to launch 2-3 mm (0.078-0.118") diameter probes was used to test gun operation. A series of shot cycles were conducted with this barrel. Using a driver tube pressure of 1600 psi and a He fill pressure of 40 psi resulted in a peak pressure pulse of 48,000 psi on average. Velocities of 2.7-3.1 km/ sec in air were achieved for projectiles weighing about 0.7g. It was this phase of shooting in which the coke bottle design of the sabot was developed as a means of successfully accelerating glass rod dummy probes.

The first major modification to the gun involved changing to a .45 caliber barrel. The decision to move from a .30 to .45 caliber barrel was done to accommodate the size of probe required to reflect sufficient signal back to the optical detection system. Coincident with the transition to the .45 caliber barrel, an effort was undertaken to find an improved operating regime for the gun. The result of this effort was a new pressure regime with the driver pressure and pump tube pressure raised to 1900 psi and 45 psi respectively. The new peak pressure was approximately 54,000 psi which accelerated a 1.9g projectile to 2.5 km/s in air on average.

Initial studies in sabot removal stripping were conducted with the .45 caliber barrel. Four methods were considered. The first was a constriction attachment to the barrel that allowed the probe to pass but not the sabot. This method was unsuccessful because of the inability to stop the sabot in a short

distance without destruction of the glass probe. Another method involved radial separation of a serrated sabot as shown in figure 4.1. Rifled barrels were obtained but testing was delayed because this method required rotating the probe which was deleterious to future plans to develop a probe that could measure all three components of the magnetic field. The radial separation scheme became a technique to resort to if other methods failed. Figure 4.2 shows a photograph of another sabot removal scheme in which a serrated sabot is peeled away from the probe by drag forces. This method was highly unreliable and rejected. Finally, evidence of gas dynamic stripping had been observed during previous shots. So another major modification to the gun was undertaken to test gas dynamic stripping as a viable sabot removal scheme. A second vented .45 caliber barrel was joined to the existing barrel to enhance the drag force differential across the sabot.

Evidence of reliable stripping was observed, but operation with two barrels proved highly undesirable. The transition joint often caused the probe to be destroyed despite significant effort to eliminate any vestiges of misalignment. Solving this problem required the gun to be de-rated and a new operating regime was found. The driver pressure remained at 1900 psi and the helium fill pressure was increased to 73 psi. Using the two barrel system, gas dynamic stripping, as discussed in section 3.3.2, was successfully demonstrated as a viable concept using the two .45 caliber barrels joined together. Ultimately, a .50 caliber barrel was chosen both to accommodate a wider sabot that permitted sufficient margin for sabot deflection and to eliminate the two barrel system. Table 4.1 shows historical data for various operating regimes obtained throughout the development of the diagnostic

Table 4.1 Summary of Gas Gun Operation Regimes

| Barrel Caliber | Driver Tube Press.(Kpsi) | Pump Tube Press.(Kpsi) | Peak Press (Kpsi) | Projectile Weight (g) | Speed (km/s) |
|---|---|---|---|---|---|
| 30 | 1600 | 40 | 48 | 0.7 | 2.5-3.1 |
| 45 | 1900 | 45 | 54 | 1.9 | 2.4-2.6 |
| 45 | 1900 | 73 | 35 | 1.9 | 2.0-2.2 |
| 50 | 1900 | 73 | 35 | 2.6 | 1.8-2.0** |

**Speed measured in vacuum

The final modification to the gas gun system was undertaken to remove stresses between the barrel coupling with the gas interface system and the barrel coupling to the pump tube. As described in section 3.1.2, a new axially locking coupler was installed to join the barrel to the pump tube and a bellows coupler was installed to replace the hard connection between the barrel and expansion tank. These modifications essentially removed all transverse stress to the barrel. These modifications did not significantly improve the flight stability of the probe as had been hoped, but they considerably improved ease of operation and enhanced the ability of the barrel to maintain alignment.

One remaining performance criteria for the gas gun involved the time required for the probe to be accelerated to maximum velocity. "Jitter" in the firing sequence was constrained to less than 1 msec. This constraint was driven by the short discharge length of the HIT plasma which is typically 7msec long with a 1-2 msec peak current flattop. Tests conducted to measure various operating times for the different steps in the acceleration process showed that virtually all of the jitter was associated with the opening of the firing valve. A custom-made firing valve was developed by joining an electronically actuated stepper motor to a high pressure ball valve. Bench tests were conducted testing the reproducibility of the actuation of the firing valve. These results are shown in figure 4.3. Jitter for these tests was less than the desired 1 msec. In conjunction with the demonstration experiments described below, measurements

of the delay time from electronic trigger pulse to "time on target" in the plasma chamber were recorded. The time required for the probe to reach the plasma chamber was 71.9 msec with a variation of 0.8 msec. Similar results were observed on shots taken on the Helicity Injected Tokamak. Table 4.2 tabulates these findings.

Table 4.2 Summary of Gas Gun Timing

| Test | Shots Recorded | Time on Target (msec) | Standard Deviation(msec) |
|---|---|---|---|
| 1st demo exp. | 20 | 53.2 | 0.73 |
| 1st HIT exp. | 5 | 53.4 | 0.63 |
| 2nd demo exp | 31 | 57.1 | 0.45 |
| 2nd HIT exp | 12 | 56.7 | 0.57 |

4.1.2 Summary of Gas Dynamic Sabot Stripping Results

Gas dynamic stripping was observed early in the initial shots involving acceleration of round glass dummy probes fired into air. As mentioned above, formal testing of gas dynamic stripping was begun with the addition of a second vented .45 caliber barrel joined to the existing barrel. Explanation of the testing program is given below.

An initial shooting cycle using round dummy probes in air confirmed the technique was viable. Extensive testing was then conducted using the auxiliary tank to control stripping pressures in the barrel while shooting square cross section dummy probes into moderate vacuum (20-50 mtorr). Stripping pressures of 10-20 psia air were used. Witness plates located a meter down range indicated about 30% of the probes remained straight 1 meter downrange. The two barrel system was deemed unacceptable and replaced with a .50 caliber system. Stability was improved with about 50% of all probes remaining acceptably straight 3 meters down range. At this point, the first in flight measurement of a magnetic field was achieved and the diagnostic was

configured to perform tests under high vacuum ($10^{-6}$ torr) in order to simulate conditions in the tokamak. During these tests, several shots were taken with the more dense faraday probes, which seemed to improve stability. This cycle resulted in approximately 60% stable flight. Following these shots the first attempts were made at measuring the magnetic field in the Helicity Injected Tokamak. Results on the tokamak were disappointing as only one successful measurement was achieved. 90% of the probes were unstable resulting in several collisions with vacuum components. The diagnostic was removed from the tokamak in order to investigate the tilting problem further.

For all of these shots the full complement of 120 1/8" diameter venting holes was employed. This number was chosen from "rule of thumb" scaling used in other gas gun experiments which suggested a venting surface area equal to approximately 10 times the barrel cross sectional area. The stripping process was effective, but probe stability was overestimated because the measuring point was not sufficiently far down range. Figure 4.4 is a plot of the stripping distance versus fill pressure for both light glass dummy probes and heavy faraday rotator probes. This data does provide some empirical scaling laws for various probe weights and fill pressures which can be used as a starting point to test new operating conditions.

The problem with the sabot stripping process was that the number of venting holes was far in excess of the number needed to axially separate the probe from the sabot. The initial scaling estimate for the number of holes was based on complete venting of the driving gas. But this is not necessary to begin separation of the probe and sabot. The probe was actually separating very near the beginning of the vent hole pattern. Once separated, the probe was no longer held straight by the sabot as it passed the remaining vent holes. The numerous vent holes provided a source of turbulence as the shock wave preceding the probe reflected off the vent holes and expanded into the auxiliary tank. This resulted in the random instabilities observed in the probe attitude.

The problem was corrected by carefully plugging the holes with very nearly flush mounted aluminum pins. Tests were conducted with various fill pressures and plugging fractions until only the first 24 of the original 120 holes remained unblocked. For these shots a new dummy glass material made of Schott glass SF-56 with a density and refractive index nearly identical to the faraday rotator materials was used along with faraday rotator probes. Once the hole pattern was reduced to 24 the results were quite encouraging with over 90% remaining stable 4 meters down range.

### 4.2 Field Measurements and Detection System Performance

In preparation for performing plasma measurements, a series of shots was conducted using the TIP diagnostic. These shots are called the "1st demonstration experiment" in table 4.2. This initial shot series involved using TIP to measure a permanent magnetic field inside a vacuum chamber. The purpose of these experiments was to integrate the various diagnostic systems into one diagnostic system and evaluate the overall performance. Specific criteria evaluated in this series of tests included probe spatial and magnetic resolution, probe flight characteristics, jitter in the 'time on target,' high vacuum compatibility, shot to shot cycle time, and system reliability.

Following successful completion of the demonstration shot cycle, the first attempt to make internal magnetic field measurements in the Helicity Injected Tokamak (HIT) was made in July and August of 1995. Tumbling of the probe caused this first attempt to be unsuccessful in achieving internal field measurements in a plasma, but a successful measurement of the vacuum magnetic fields was achieved and several issues of concern were eliminated.

The tumbling issue was addressed by removing the diagnostic from the tokamak and reconstructing the demonstration experiment to allow a directed effort at solving the problem. A few key design changes were made and tested resulting in a significantly upgraded diagnostic. The diagnostic was again

mounted on the tokamak and measurements of the internal toroidal magnetic field of the plasma were conducted. Results of all of the demonstration experiments are described in the following sections. Results of measurements on the tokamak are described in chapter 5.

### 4.2.1 Description of Demonstration Experiment Setup

The layout for the initial demonstration experiments is shown in figure 4.5. The permanent magnetic field consisted of two large horseshoe magnets with like poles opposing each other to create a large spatially varying axial field. These magnets were housed approximately two meters down range from the barrel in a 25 $\ell$ tank. A turbo pump was installed such that base pressures of less than $3 \times 10^{-6}$ were achieved. The remaining systems shown are those described in section 3.

Several diagnostics were used to evaluate the performance of the diagnostic. Probe speed and location was determined by detecting the interruption in a single HeNe laser beam that intersected the probe path in two locations. Beam separation distance was 72.9 cm +/- 0.1 cm. A CAMAC 8837 digitizer operating at 8MHz recorded the timing data. Uncertainty in the speed measurement was approximately 1%. Probe pitch and yaw was evaluated with a high speed image converting camera. A series of six photographs were taken each shot with a delay of 10 micro-seconds between frames. A pair of mirrors canted approximately $45^0$ with respect to vertical allowed the camera to observe both pitch and yaw. Vacuum baseline pressure data was obtained using ion gauges. Post shot pressure data in the expansion tank was recorded with a fast time response (<1 msec) Baratron® gauge. The final diagnostic consisted of the optical detection system itself. Optical data from the probe was used to detect tumbling in the probe and to determine the timing of key points in the shot by observing characteristic signatures in the reflected signal.

The changes in the demonstration experiment layout following the first attempt were relatively minor. As discussed earlier, the coupling system between the pump tube and barrel was changed along with the coupler between the barrel and expansion tank. Additionally, the overall length of the firing range was increased. This was done to replicate the flight path length associated with measurements in the tokamak. In the original demonstration experiments the amount of probe tilt was underestimated due to the abbreviated flight path. Finally, the most significant change, though not evident in the diagram, was the replacement of the ¾" O.D. tubing with 1½" O.D. tubing.

### 4.2.2 Summary of Demonstration Experimental Results

In the first demonstration experiment, a series of 24 shots using both glass 'dummy' probes and faraday rotator probes were conducted. Based on optical data, 16 of the shots were considered acceptable. Four of the eight unacceptable shots failed to separate fully from the sabot. This was determined to be due to insufficient stripping pressure in the auxiliary tank. Acceptable vacuum tank base pressures were consistently achieved with minimal maintenance required between shots. Four hour cycle time between shots was attained. A black residue was left on the inside of the expansion tank due to melting of the sabot. This residue was found not to measurably affect base pressure. But cleaning after approximately 10 shots was found to improve overall vacuum performance. Pressure measurements in the simulated plasma chamber increased by 7 mtorr indicating less than 0.4 torr-l of helium entering the chamber.

Optical data collected during the demonstration experiments was used to assess the performance of the optical detection system and the ability of the diagnostic to make magnetic field measurements. Figure 4.6 shows the complete detector data trace from just prior to probe acceleration to just after colliding with the breakable mirror. This shot was taken using a glass dummy

probe so that no magnetic field modulation is present in the signal. The complete trace is shown in order to display several characteristic signatures of a good data trace. Of first note is the loss of signal at time 53.6 milliseconds which probably occurs when the probe is accelerated. Shortly after the probe enters the vacuum chamber about 10 centimeters downrange, the signal is quickly regained at time 54.7 milliseconds. Ideally, if the probe does not tilt and the illumination beam is properly aligned, the signal intensity increases nearly linearly as the probe approaches the illumination source as shown. The signal abruptly ends when the probe hits the breakable mirror at time 56.5 milliseconds. These features are quite reproducible and can be used to check system timing.

As discussed in section 3.4.3, the quality of the reflected light profile has a significant effect on the accuracy of the detection system. Figures 4.7 and 4.8 show the raw data taken from two demonstration shots measuring the permanent magnetic field in the simulated plasma tank. The first shot has a continuously increasing intensity profile, whereas the second has a decreasing intensity profile at the end. The magnetic profiles derived from this data are shown in figures 4.9a,b. Overall the field measurement is better for the increasing profile of figure 4.9a, though some variation is observed over time. Figure 4.9b shows the measurement in which the probe was either tilted or the beam was slightly misaligned resulting in the decreasing intensity profiles. Analysis of this data shows a larger drift is observed in the baseline polarization angle resulting in a larger drift in the magnetic field profile. As mentioned previously, the mechanism which results in the polarization drift is not understood. This effect does not affect the ability of the probe to observe local fluctuations in a rapidly varying magnetic field, but it does significantly hinder the ability of the diagnostic to make absolute measurements of the magnetic field to the desired 20 gauss sensitivity over the entire three to four meter transit.

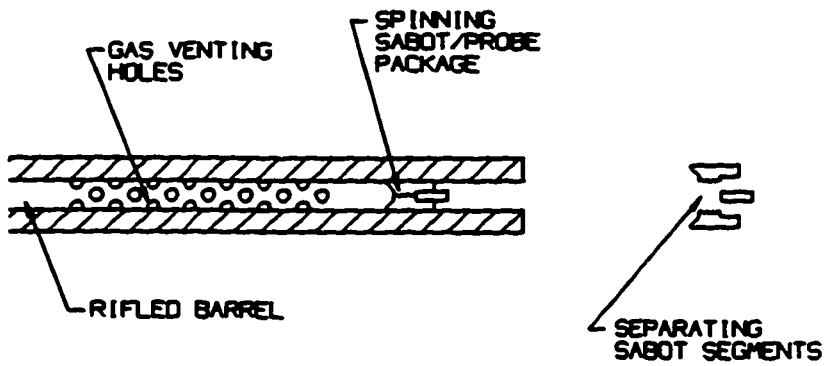


Figure 4.1 Schematic for radial sabot separation.

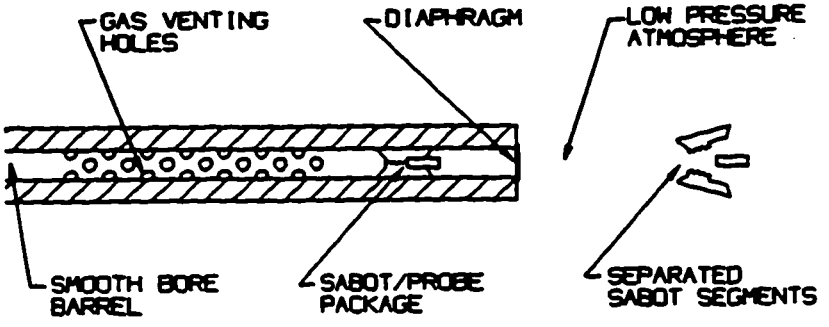


Figure 4.2 Schematic for serated sabot separation.

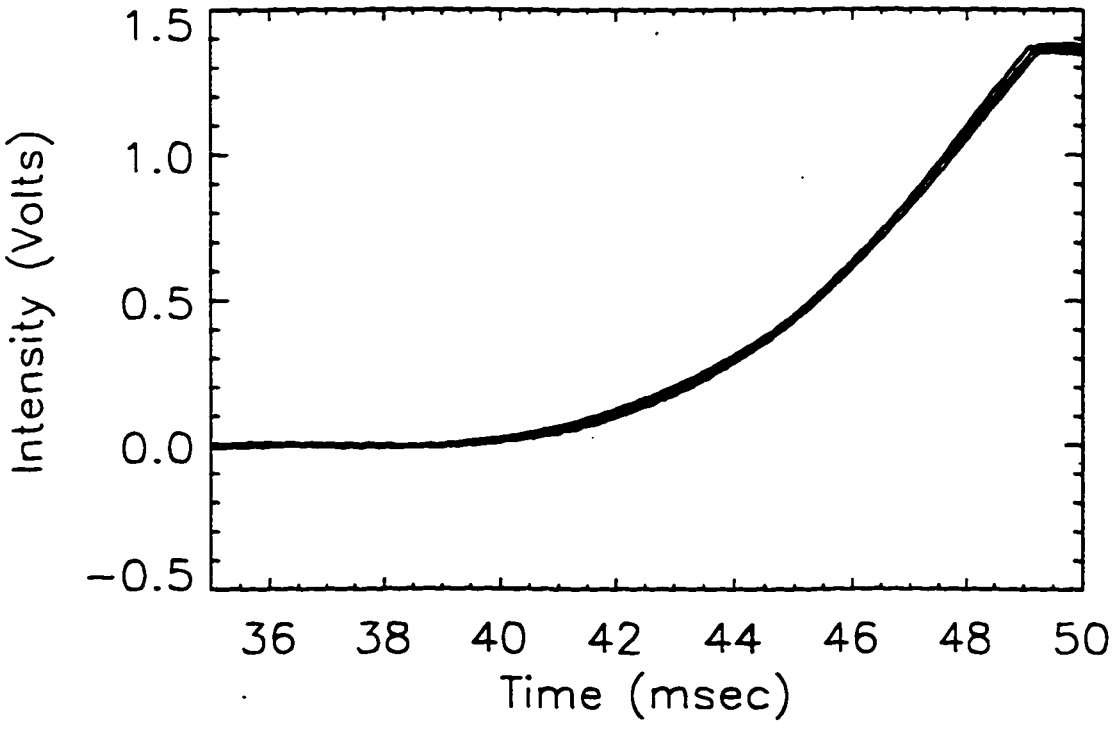


Figure 4.3 Plot of firing activation pressure vs. time for stepper motor driven firing valve

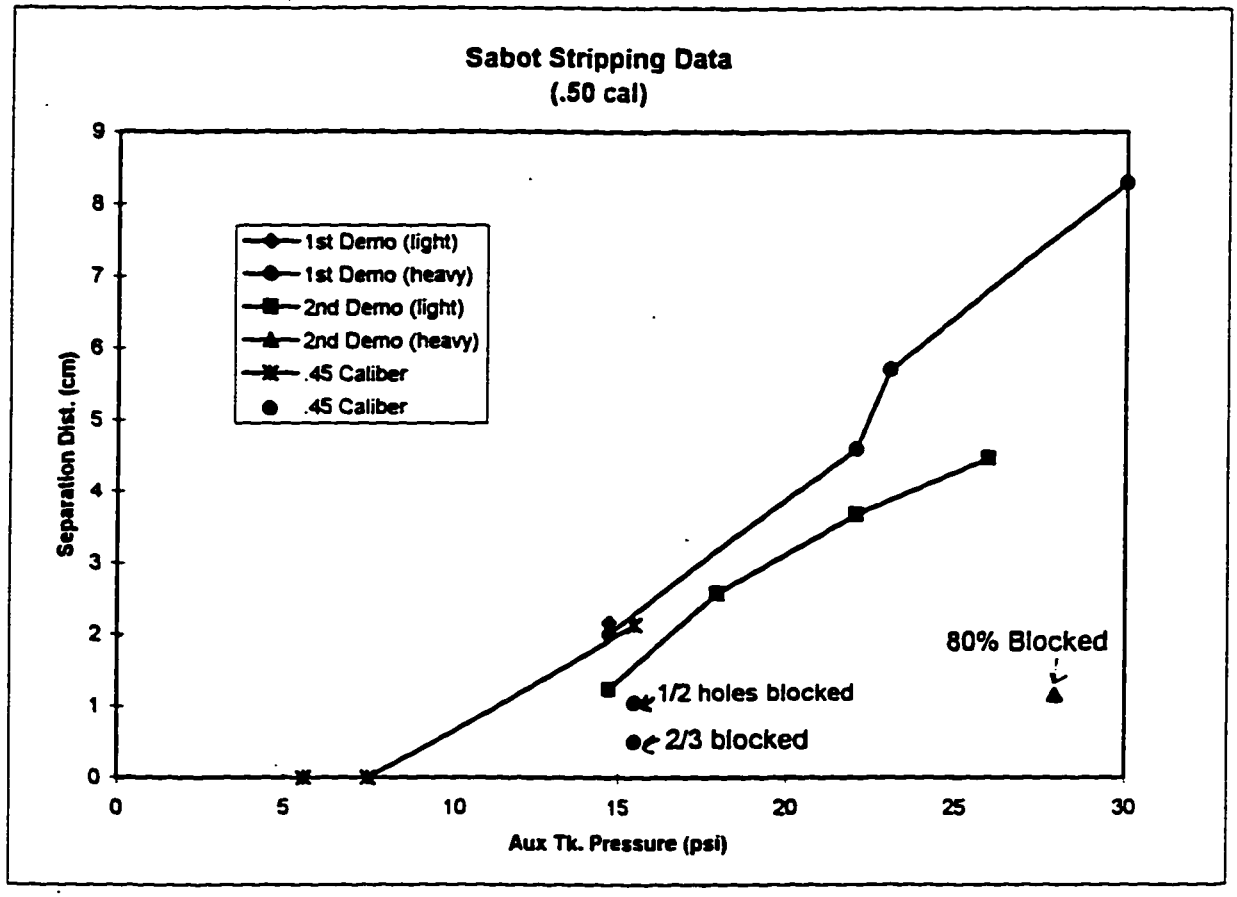


Figure 4.4 Plot of separation distance versus barrel fill pressure for different barrel sizes and stripping configurations

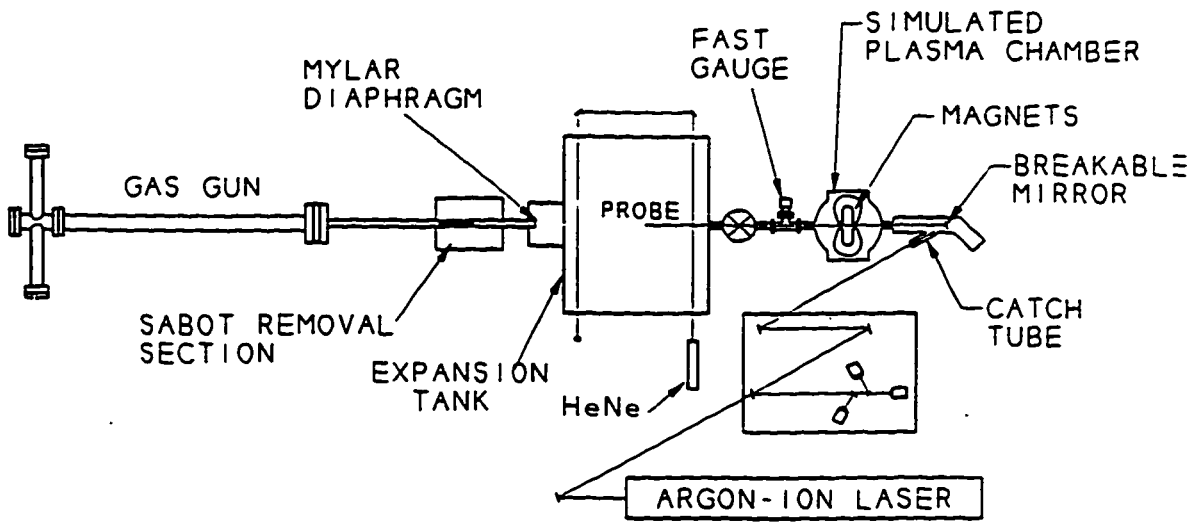


Figure 4.5 Diagnostic layout for demonstration experiments

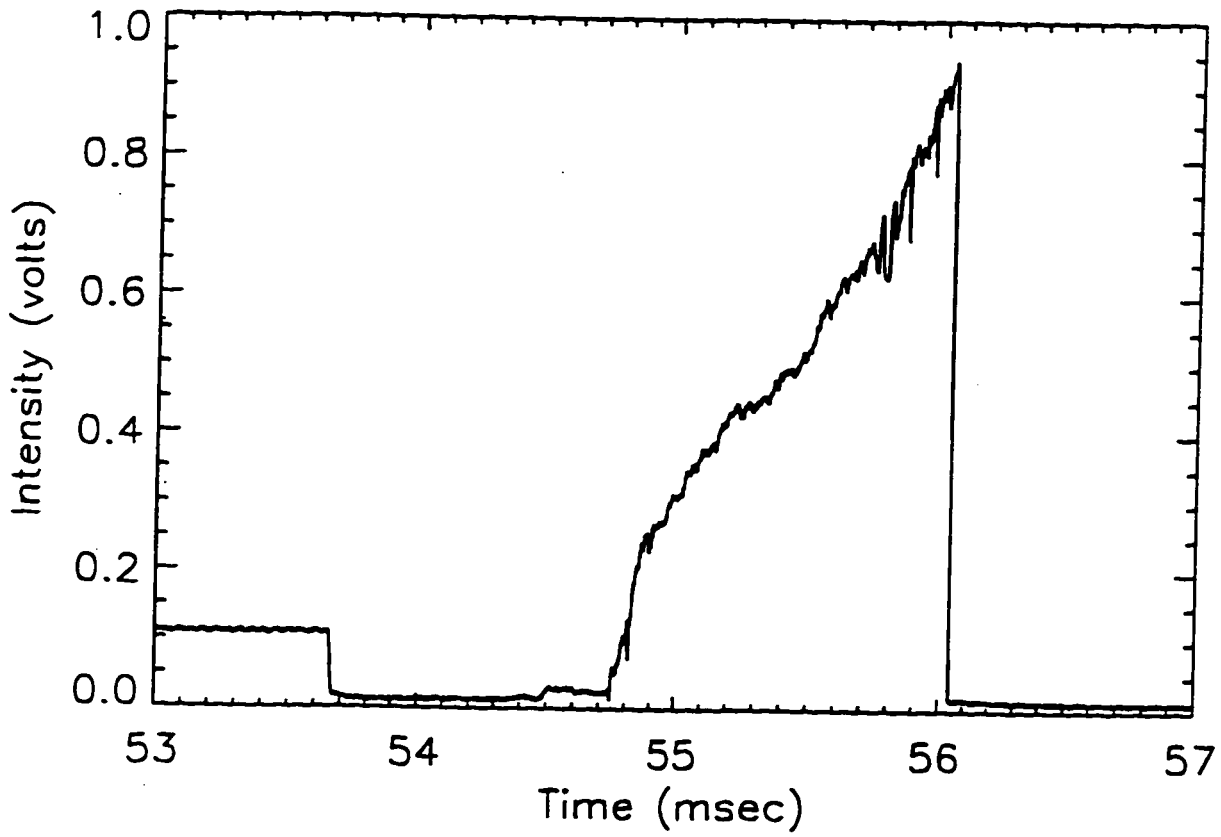


Figure 4.6 Light intensity recorded for detector one during entire flight profile.

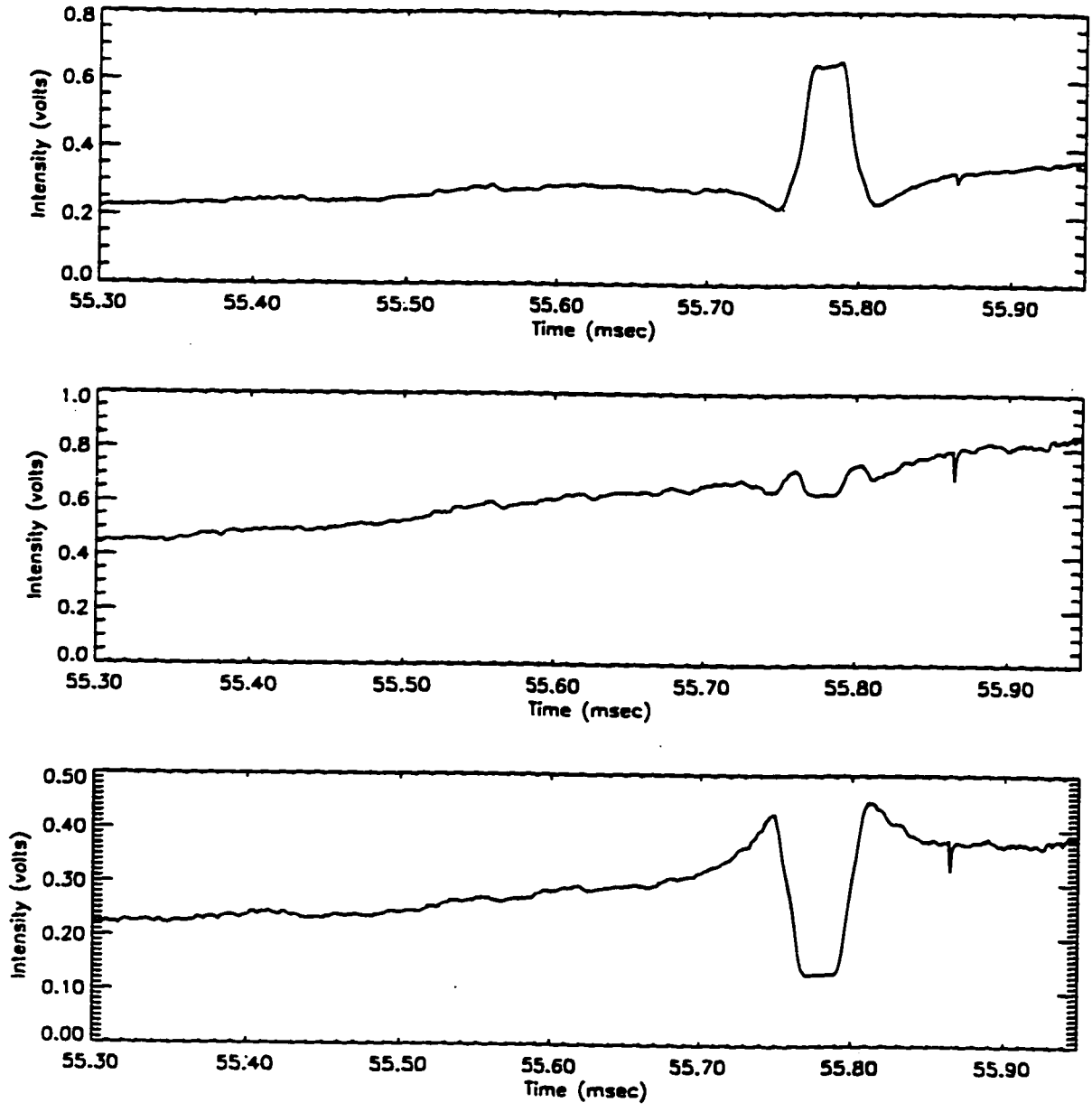


Figure 4.7 Demonstration experiment raw data recorded during measurement of permanent magnetic field profile with increasing light intensity.

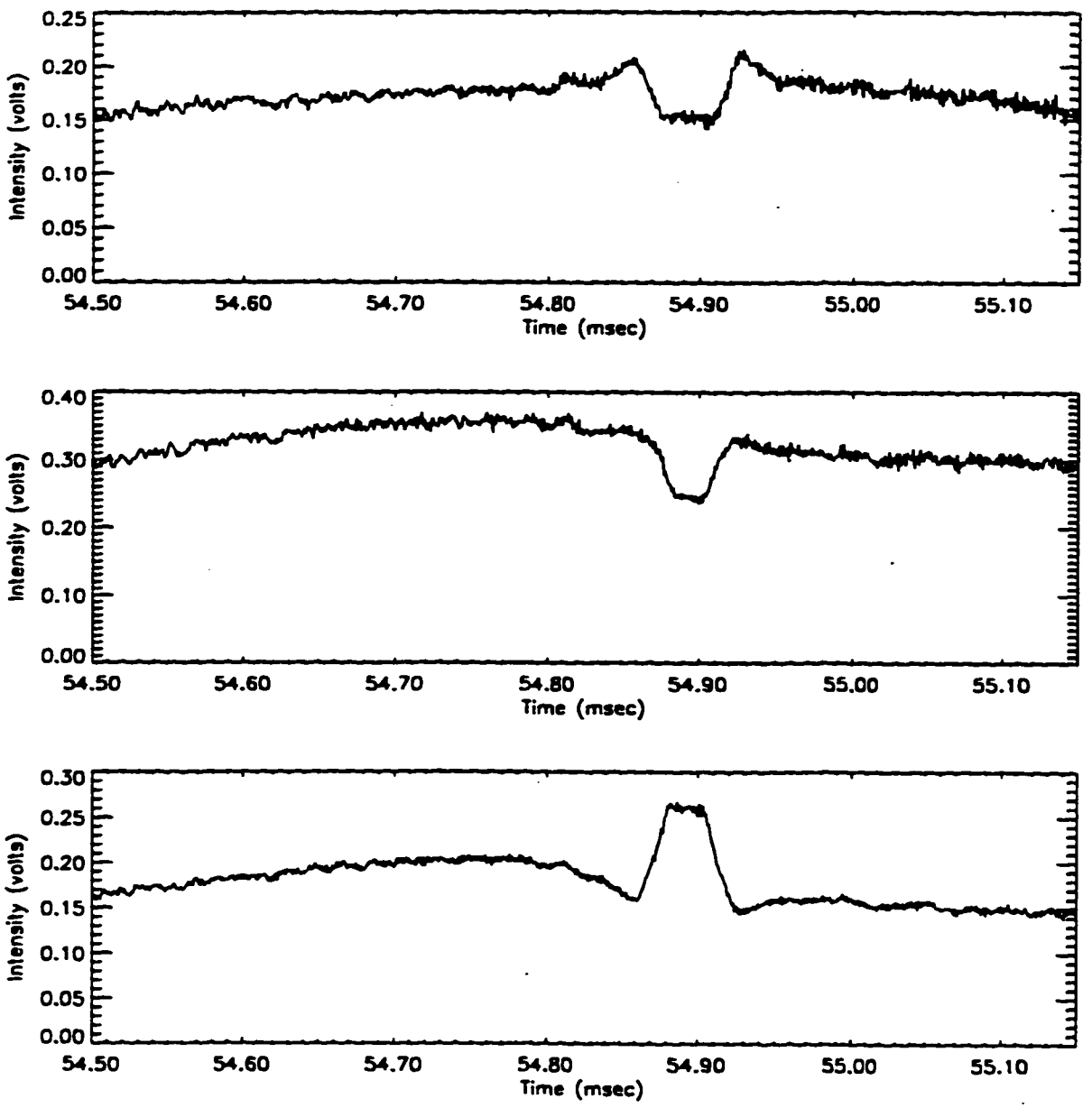


Figure 4.8 Demonstration experiment raw data recorded during measurement of permanent magnetic field profile with decreasing light intensity.

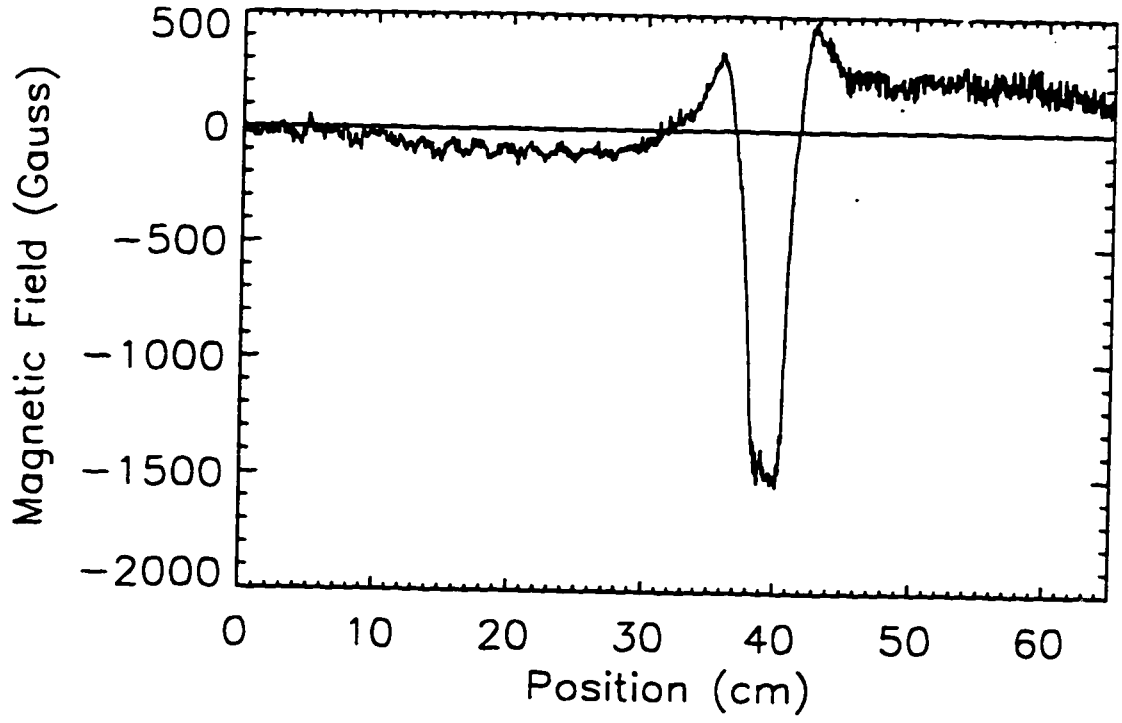


Figure 4.9a Demonstration experiment permanent magnetic field profile measured by TIP with decreasing light intensity.

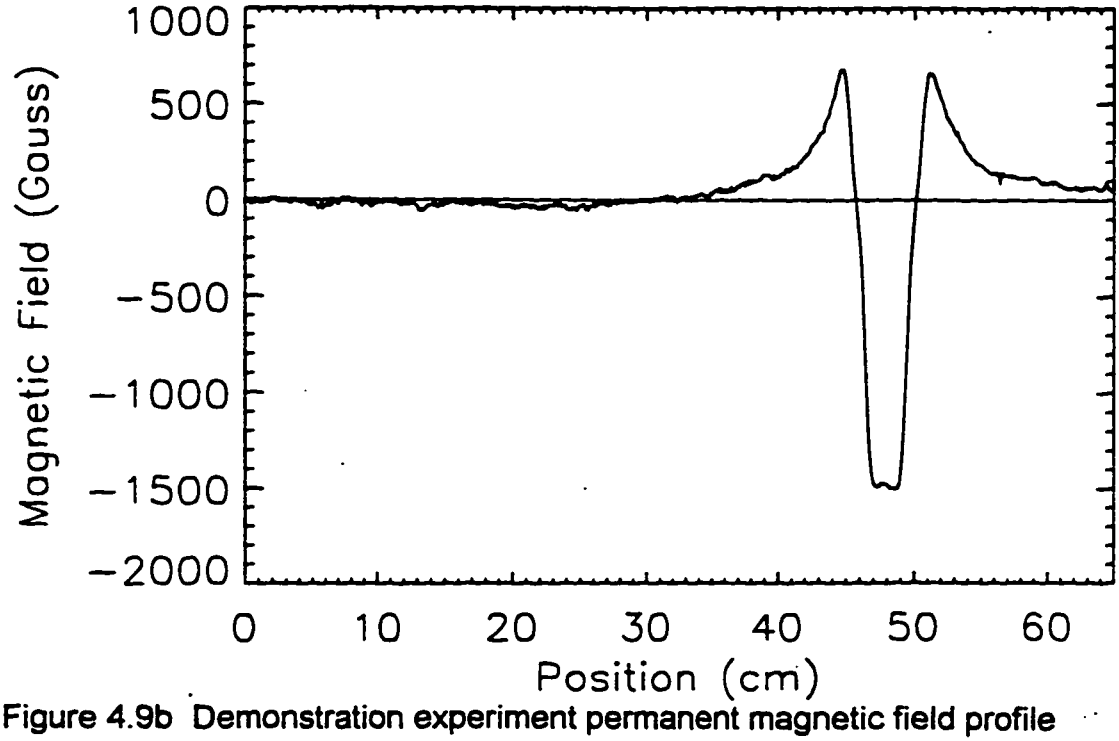


Figure 4.9b Demonstration experiment permanent magnetic field profile measured by TIP with increasing light intensity.

## 5. Application of the TIP Diagnostic to the HIT

### 5.1 The Helicity Injected Tokamak

#### 5.1.1 Description of the Helicity Injected Tokamak (HIT)

The Helicity Injected Tokamak [17] is a low aspect ratio (A=1.5) tokamak designed to investigate steady state current drive through helicity injection. Figure 5.1 shows the tokamak from above looking down. The major radius is 31 cm. A copper flux conserving shell used to stabilize high frequency external modes and support equilibrium fields has R=50 cm at the midplane. In order to allow diagnostic access, the shell is divided into two halves separated 5 centimeters apart by conducting bridges at the equatorial plane of the tokamak.

Formation of the plasma is shown in Figures 5.2a,b. Initially, the toroidal field coils are fired to develop the vacuum toroidal field, $B_0$, and the bias coils are fired to develop essentially radial magnetic fields in the injector region as shown in Figure 5.2a. A voltage is then placed across the injector, driving a radial current, called "injector current." This current experiences a J x B force with the toroidal field which pushes the radial magnetic field into the toroidal chamber as shown in Figure 5.2b. This poloidal flux links the injected toroidal flux to create helicity and drive plasma current. The process is sustained by maintaining the voltage across the injector. This voltage essentially pumps toroidal flux, and therefore helicity, at the rate given by,

$$\dot{K}_{inj}=2V_{inj}\psi_{inj} \qquad \text{Eq. 5.1}$$

Typically, plasma discharges last 7-10 msec. Peak plasma currents of 200 KA are routinely sustained for 1-2 msec periods. Plasma density is 5-10 $x10^{19}$ $m^{-3}$ and plasma electron temperature is around 40-80 eV.

### 5.1.2 Diagnostics on the Helicity Injected Tokamak

Many diagnostics are used to investigate important parameters on the tokamak. These diagnostics include external magnetic probes, rogowski coils, flux loops, VUV spectroscopy, Thompson scattering, and far infrared interferometry. Rogowski coils are used to measure currents in the toroidal field coil system and various capacitor banks. So called "bridge rogowski's" are used to measure current distribution in the flux conserver by measuring the current passing through the various bridges separating the flux conserver. Flux loops are positioned along the inside of the center conductor and around the outside of the flux conserver to provide flux information for constructing the plasma equilibrium. Two voltage probes measure electrode voltage at each end of the tokamak and two VUV spectrometers are used to look at OV and OVI lines in the plasma. Four $H_\alpha$ light detectors are used to look at $H_\alpha$ emission in four localized regions of the plasma. Density information is obtained using a far infrared interferometry system. A single point Thompson scattering system is normally used to determine electron temperatures, but space requirements forced its removal during operation of the TIP diagnostic.

Besides measuring just plasma parameters, vacuum integrity and purity were critical issues in the evaluation of the TIP diagnostic. Base vacuum pressure was monitored with an ion gauge and operating pressure was monitored with a convectron gauge. Composition of impurities in the tokamak was monitored before and after TIP shots using a residual gas analyzer.

## 5.2 TIP Diagnostic Layout for HIT Measurements

### 5.2.1 Basic Layout for all TIP Measurements on HIT

Figure 5.3 shows the basic physical layout for operation of the TIP diagnostic on HIT. Essentially all systems are the same as discussed earlier for the demonstration experiments, with the exception of some modifications to the

firing system, speed detection system and operational procedures. The firing system was modified in two ways. First, firing control of the gun was turned over to the HIT control system via an optical trigger pulse. Second, two isolation valves, H-1 and H-2, were installed to isolate the tokamak from the TIP vacuum systems. These valves were interlocked with the HIT firing system to prevent firing the gun while these valves were closed. In addition, the valves were interlocked with the TIP vacuum system to prevent opening the valves if pressure in the TIP vacuum tanks exceeded 50 mtorr. An interlock bypass system was also included to permit HIT operation independent of TIP.

The speed detection system was modified to improve accuracy and reliability. Two ports were installed to allow the speed trigger beam to intersect the probe path before and after transiting the tokamak. The position of these ports is shown in figure 5.3. Separation distance between these beams was 2.93 meters. Increasing the separation distance and having the beams bracket the plasma region reduced the uncertainty in the probe position to less than 0.5 cm in the tokamak. Reliability was improved by installing a cylindrical lens in the second speed trigger beam. This expanded the beam in the vertical plane insuring that the probe would intersect it. The procedures and checklists necessary for integrated operation of the diagnostic on the tokamak are included in appendix C.

### 5.2.2 Probe Pitch and Yaw Measurement System

An additional modification to those previously discussed was made to the TIP diagnostic for the second installation on HIT. This modification included the installation of two pairs of permanent magnets designed to detect pitch and yaw in the probe. The magnets simply consisted of two 1 inch diameter high performance permanent magnets held ½" apart by an aluminum frame. The predominant fields were oriented perpendicular to the flight path in the horizontal

and vertical planes. Peak field intensity perpendicular to the probe was nominally 3000 gauss. Figures 5.4a,b show the probe trajectory through the magnets. If the probe were tilted, it would pick up the transverse field as a function of the $B_{mag}$ times the sine of the tilt angle. By measuring the amount of faraday rotation in the probe as it passes through the permanent magnets, the amount of transverse field "seen" by the probe can be determined. The tilt angle can be calculated by adjusting the tilt angle such that the measured field matches the previously recorded field profile of the permanent magnets.

Unfortunately, the transverse profile was too highly peaked, making precise measurement of the tilt angle highly difficult. Additionally, operation near the tokamak resulted in enhancement of the field strengths in the magnets, further obscuring attempts to measure the tilt angles using comparisons to the previously measured values. Ultimately, only qualitative information was obtained concerning the direction and rough magnitude of probe tilt.

## 5.3 Measurements on the Helicity Injected Tokamak

### 5.3.1 Results of the 1st Measurements on the Helicity Injected Tokamak

A total of 14 shots were taken with the TIP system mounted on HIT. These are tabulated in table 5.1 at the end of this chapter. The first six shots were practice shots in which the probe was blocked from entering the tokamak. These shots allowed evaluation of the probe flight profile and operation of the optical detection system. Shots 1-4 showed significant probe tumble which was believed due to the interface between the vacuum tank and barrel. The stress in this interface was relieved and shots 5 and 6 were excellent.

Two shots were taken with the probe traveling through the tokamak with all coils firing, but no plasma in order to check TIP performance against the calculated vacuum magnetic fields. The first one, shot 7, collided with the

tokamak at the inlet probably due to an overall misalignment caused by improper gas pressure in the pneumatic mount for the tokamak. No tumbling was observed. The misalignment was corrected by hard mounting the tokamak to the floor at the proper height. Shot 8 passed through the tokamak cleanly and magnetic field profile data was obtained. The results of this shot will be discussed more in Section 5.3.3.

Shots 9-11 were fired into the tokamak with plasma. Two of these shots tumbled and collided with the exit piping leading from the tokamak and breached the vacuum system. The third shot tumbled and hit the seat of the isolation valve H-2 which had not fully retracted. Various intermediate steps were taken to improve alignment, which helped, but overall the clearance margin in the exit tubing was too small to reliably shoot the probe through the tube in the event the probe tumbled.

The possibility of the tokamak causing the instability in probe flight was investigated. Three test shots were fired with the probe blocked from entering the tokamak and no coils firing. Two of the three probes tumbled indicating that the problem was not the tokamak. The shot sequence was terminated and the diagnostic removed from the tokamak until the inlet and outlet ports could be enlarged to prevent further collisions with the vacuum system.

### 5.3.2 Results of 2nd Set of TIP Measurements

A total of 15 more shots were taken during the second shooting cycle on HIT. These are summarized in table 5.2 at the end of the chapter. The first two shots were successful in obtaining data and consisted of completely unclad probes fired through the plasma. Shot 3 was a successful vacuum shot. Difficulties in a variety of forms were encountered in shots 4-11. These shots were intended to address the problem of impurity introduction into the plasma due to surface impurities on the probe and ablation of the retro sheet.

Improvement was attempted by placing a stainless steel plate on the back of the probes and using special cleaning procedures to construct the probe. In the majority of the failed shots, the retro sheet and metal back came off of the probe.

Three sources of the failure were postulated based on correlation between failures and probe construction. First, these probes were not beveled on the face, thus limiting the surface area at the edge of the probe for the glue to adhere. Second, the residual cleaning solutions, alcohol and freon, left on the surface may have attacked the glue and weakened the bonds. Finally, the glue bottle may have been bad. Ultimately the faces were beveled, cleaning was limited to the surfaces away from the retro sheet, and the glue was replaced. Data were obtained from shot 12 in which the probe was fired through the tokamak with no plasma. Shots 13 failured with no data received, but good data was obtained from shot 14 in which a high current plasma was present. At this point, the shot cycle was terminated to allow the installation of a new optical detection system. These shots are summarized in table 5.3 as a reference for discussion of the probe effects on the plasma later in this chapter. Magnetic field measurement results from those experiments will be included in another dissertation by the designer of that detection system.

### 5.3.3 Hall Probe Vacuum Field Measurements

Evaluation of the diagnostic requires a highly accurate model of the vacuum magnetic field to compare with the measurements made by the TIP diagnostic. A model that treats each toroidal field coil as an infinite conductor was developed to perform this task. Figure 5.5 shows the trajectory of the probe through the tokamak and the relative position of the toroidal field coils. The field along the trajectory was simply calculated using the Biot-Savart law using the code "CALC_VAC" which is included in appendix E. If the coil locations are well known, this model is quite accurate, but small uncertainties in coil geometry on the order of millimeters result in unacceptable field uncertainty. Consequently, a

high accuracy, large bandwidth Hall probe was used to benchmark the vacuum field model. The hall probe was carefully positioned along the probe flight path in 1 and 2 centimeter increments and the toroidal field coils were fired at each location. This data was normalized to the toroidal field coil current and averaged over 20 milliseconds. The resultant profile was then used to benchmark the calculated profile.

This was done by adjusting the geometric location of the toroidal field coil bundles and the calibration factor relating toroidal field coil current to the voltage measured on the rogowski coil such that the output of the calculated fields matched the hall data. Figure 5.6a plots the Hall profile with the calculated field data and figure 5.6b shows the residual difference between the two. Unfortunately, the hall probe cord length was not sufficiently long to permit mapping across both return bundles. From this data, the exiting return bundle was found to be 5 millimeters further away from the center column than originally assumed and the rogowski coil calibration factor was off by approximately 5 percent.

### 5.3.4 Vacuum Field Measurements

Three measurements of the vacuum toroidal field profile were obtained using the TIP diagnostic. The first was obtained in the first shot sequence. The remaining two were taken during the second sequence (shots 3, and 12). The purpose of the vacuum shots was to evaluate the diagnostic performance and to provide a baseline vacuum magnetic field profile for comparison with plasma profiles along the same trajectory. The measured field profiles were compared with a calculated magnetic field model discussed in the previous section.

Results of the first TIP field measurement on the tokamak are shown in figures 5.7 and 5.8a,b. Figure 5.7 is the raw detector data. Figure 5.8a shows the analyzed data with the calculated vacuum magnetic field overlaid and figure 5.8b shows the residual difference between the measured and calculated

magnetic field profiles. The large variance in the data for figure 5.8a is due to probe tilt, uncertainty in the trajectory relative to the tokamak, and drift in the zero field polarization angle believed due to probe rotation and scattered light. By including probe tilt and location in the analysis code and fitting the data to regions of known magnetic field, the uncertainty in probe position and orientation can be significantly reduced and the accuracy of the measurement improved. In the case of vacuum shots, the data are attempted to be fit throughout the profile. For plasma shots, fitting is limited to regions outside the plasma chamber. This corresponds to four locations, the areas of zero field at the beginning and end of the transit, and the two small peaks near the toroidal field current return bundles.

Five geometrical fitting parameters are used as fitting parameters to correct the data to account for deviations in probe orientation and trajectory. The first two parameters are pitch and yaw. Each is modeled by assuming the probe exits the barrel perfectly straight and then rotates about the vertical and horizontal axes at a constant rate. The remaining three parameters take into account variations in the overall trajectory through the tokamak. Specifically, they are the impact parameter above the center column, the horizontal incidence angle relative to the center column with zero being perpendicular, and vertical incidence angles relative to the floor with zero being parallel to the floor. These five parameters are used to minimize the residual difference between the measured data and calculated data in the regions of known magnetic field. The actual fitting is conducted by manually adjusting the parameters using the interactive code "NEW_MAG.PRO" with "NEW_MAG_EVENT.PRO". Both are included in Appendix E. As the parameters are adjusted the residual difference is monitored and minimized. Emphasis was placed on minimizing the residual in the region where the raw signal intensity was increasing or steady. A numerical minimization code was not employed because systematic uncertainties that will be discussed later in this chapter resulted in large residual differences that could not be accounted for by the geometrical parameters.

Figure 5.9a,b shows the corrected measured field data from the first vacuum measurement. Vertical lines show the edges of the flux conserver. The TIP measurement through the first 2 ½ meters is excellent. The large drift in the polarization seen in the latter stages of the transit correlates with the rapidly dropping intensity profile. At time of impact, this probe was estimated to be tilted 29 degrees. Unfortunately, all three vacuum field measurements had poor intensity profiles due to probe tilt and beam misalignment. Figures 5.10 and 5.11a,b show the raw data and analyzed vacuum field data taken from the first vacuum field shot in the second shot sequence on HIT. The illuminating laser for this shot was oscillating severely, resulting in the large variations in the intensity profiles. These variations did not noticeably affect the measurement, only the overall decreasing trend had an effect. For this shot the probe was tilted 19 degrees at impact and the intensity profile was strongly decreasing as the probe was crossing the centerline of the tokamak. Fitting of this data to the calculated field was little better than 4%. The central peak shows a large variation from the calculated vacuum that is present in all shots taken during the second shooting cycle on hit.

### 5.3.5 Internal Plasma Profile Measurements

Three internal magnetic field measurements in the plasma were made on the Helicity Injected Tokamak. Plots of the plasma current versus time for each shot are shown in figures 5.12a,b,c. The time the probe was in the plasma is shown in by the vertical lines. Shot one occurred early in the formation portion of the discharge, shot two entered the plasma very near the end of the discharge, and the third plasma measurement (shot 15) entered at the peak of the discharge. The first plasma shot raw detector data is shown in figure 5.13. Again the intensity rises throughout the transit until it exits the flux conserving shell, where it begins to descend despite getting closer to the detection system.

The decrease in intensity for this shot can only be attributed to slight misalignment of the beams, because the tilt was only 4 degrees at final impact.

The analyzed magnetic field profile is portrayed in figure 5.14a with the calculated vacuum magnetic field overlaid and the residual difference in figure 5.14b. The raw signal data and analyzed data for the second and third plasma shots are presented in figures 5.15-5.18. Figure 5.19 shows the residual differences for all three plasma shots plotted together.

To first order, the probe measurement follows the vacuum magnetic field with 2.5% accuracy. But the characteristic variation from the calculated vacuum field observed in the vacuum shot is seen in each of the plasma shots. The intensity profiles are all similar and indicate a systematic misalignment as the probe moves out of the center of the illumination beam approximately near the point it exits the flux conserver. This results in the much discussed drift in polarization baseline. Locally, the probe still accurately measures variations in the field. This is seen in the first shot, figure 5.14b, at the 90 cm axial position, two small peaks are observed which correlate to the field created by some steel vacuum joints which concentrate the magnetic flux outside the tokamak. Consequently, the probe remains effective at measuring small local fluctuations in the field, despite the overall drift in baseline polarization which precludes fine scale determination of the overall equilibrium field structure. Section 5.5.1 provides a discussion of these measurements of the internal magnetic field profile of the Helicity Injected Tokamak.

## 5.4 Probe Effects on Tokamak Performance

### 5.4.1 Results of Probe Effect on Plasma Current

As discussed in chapter 2, interaction of the plasma with the probe results in the introduction of impurities through the process of sputtering and ablation.

The effect of these impurities was qualitatively investigated by observing various plasma diagnostics as the probe transited the plasma. Precise evaluation of the probe heating model was prevented for two main reasons. First, the removal of the Thompson scattering diagnostic to accommodate the TIP diagnostic prevented obtaining plasma temperature data during the TIP shots. Second, the previously described difficulties in obtaining optical data resulted in reverting back to probes with unprotected retro sheets which ablate instantaneously in plasmas above a few eV. Despite these impediments, useful information concerning the effect of probes on the plasma was obtained.

The most dramatic effect of the probe on the plasma was observed in the plasma current versus time profiles. On the majority of shots, a significant drop in plasma current occurs approximately 200 micro-seconds into the plasma. This correlates to a radial position in the tokamak of R= 19.5 cm (8.5 cm before closest approach to the center column). Figure 5.12 shows the plasma current versus time for the three plasma shots discussed earlier and figures 5.20-5.27 show current profiles of an additional eight different shots through the plasma in which optical data was received from the retro-reflecting sheet. In all ten of these shots a drop in current is observed.

Figure 5.28-5.32 shows the data for shots taken in the plasma in which no optical data was received because the retro-reflecting sheet was believed separated from the probe. In these shots, the current drop is not consistent. Shot 9279 in figure 5.28 the current drop is indeterminant because it occurs at the end of the shot as is the case in shot 9289. Figure 5.30 showing shot 9306 has the characteristic current drop, but shots 9354 and 9398 remain constant or increase. Figure 5.33 shows the effect on the plasma when the bullet collided with the inlet tube due to a failure in the sabot removal system. Finally, the effect of the small amount of muzzle gas entering the tokamak was investigated by shooting a sabot without a probe such that only the escaping muzzle gas entered the tokamak. The plasma current profile for this shot is shown in figure

5.34 and does not show any abnormal drop in plasma current. A discussion of these results pertaining to the probe's effect on the plasma is given in section 5.5.2.

### 5.4.2 Results of Probe Effect on Plasma Density and Other Parameters

Reliable density data using the far infrared interferometer was obtained only on shots 9231 (first plasma measurement) and shot 9403 taken after installation of the new optical detection system. This data is shown in figures 5.35a and 5.35b. The density does not appear to show any response to the presence of the probe.

Additional plasma data taken from the third plasma shot (shot 9363) is shown in figures 5.36a,b,c,d portraying the plasma OV and OVI emission intensity, the OV to OVI ratio, and $H_\alpha$ from one detector. $H_\alpha$ measurements showed an expected sharp peak as the probe passed through the viewing cone of the detector, but background emission showed no changes. The OV intensity is not changed but the OVI data drops quite quickly upon the probes entrance into the plasma.

Another concern for the TIP diagnostic was its effect on the tokamak base pressure which routinely operated between $8 \times 10^{-9}$ torr and $3 \times 10^{-8}$ torr. Alignment of the TIP diagnostic requires open connection between the tokamak and the TIP vacuum systems for periods up to several minutes. These periods were found to have little effect on tokamak base pressure, raising it a few $10^{-8}$ torr and immediately following isolation base pressure was re-established. The content of the impurities was investigated with a residual gas analyzer before and after several TIP shots. The results showed no significant changes in long term baseline impurities. Overall, performance of the tokamak was not diminished as a result of TIP operation.

## 5.5 Discussion of Plasma Measurements

### 5.5.1 Discussion of TIP Magnetic Field Profile Measurements

The internal field profiles measured on the Helicity Injected Tokamak were taken along a chord in the direction of the toroidal field. This location was largely determined by the access available on the machine. Mapping the field in this direction had many advantages and one significant disadvantage. The advantage of this geometry was that it allowed the diagnostic to be tested by measuring the toroidal field which is well known analytically. Additionally, the probe sampled the majority of flux surfaces in the plasma twice on each transit. Ideally, the equilibrium current profile of the tokamak could be determined by evaluating the modification to the vacuum toroidal field due to the current distribution in the plasma. Computer model calculations predicted the modulation in vacuum toroidal field profile at R = 18 cm between a peaked current profile and an edge dominated profile to be on the order of 50-100 gauss or 0.25% of the vacuum toroidal field. Appendix F provides a summary of these calculations. This high degree of resolution represents the highest resolution attained during bench testing of the optical detection system in which uncertainties of less than 20 gauss absolute were achieved.

The TIP magnetic field measurements on the Helicity Injected Tokamak were accurate to approximately 2.5% of the measured values. This is a high degree of accuracy for any plasma diagnostic, and is significantly better than other techniques used to measure magnetic fields in plasmas. But it was not sufficient to make conclusions about the current profile distribution.

The observed uncertainty is comprised of random baseline uncertainty of roughly 50-100 gauss peak to peak, and a 200-300 gauss systematic error that is accentuated in the regions of high field. The increased random error is not unexpected since the baseline bench measurements were done under ideal conditions. Polarization measurements for the bench tests were conducted by taking 1024 data points at 1 MHz at a fixed location and averaging over the

entire millisecond of data. The probe was then moved to a new location and the process repeated. The profile measurements taken in flight consisted of a single data point taken every microsecond representing 1.9 mm of travel. This reduction in samples for a given location significantly affects the random error.

Many sources are likely contributors to the magnitude of the systematic uncertainty in the measurement. As discussed earlier in section 3.4.2, the motion of the probe changes the light signal received by the detection system. Despite normalization, these effects can subtly affect the measured polarization over distance. Additionally, rotation of the probe was shown earlier to clearly affect the output polarization. Another likely contributor to the uncertainty is damage to the retro-reflector sheet sustained during acceleration. The probe experiences acceleration on the order of a mega-g. As the sabot is driven forward, the retro-sheet is compressed into the glass probe. Reflectivity tests of retro-sheet material compressed using a mechanical press showed that the retro-reflector material remained functional, though the reflected intensity was reduced. This test was essentially a static test relative to the time scales of the experiment, thus the dynamic response of the retro-sheet could be different. Since uncompressed retro-sheet has many non-ideal properties in terms of preserving polarization, this additional damage likely makes the reflected light more elliptic. All of these sources of error are magnified as the probe tilts to increase the incidence angle of the illuminating beam. As the probe travels, the amount of tilt increases and the drift in polarization angle increases with distance.

### 5.5.2 Discussion of TIP Diagnostic Effect on Plasma

The results of the TIP plasma measurements support the model described in chapter 2 that is used to determine the plasma conditions under which the diagnostic can operate effectively. For shots without a retro-sheet, the model predicts belief times of 100 to 1000 micro-seconds for plasma temperatures of

80 to 40 eV respectively. The TIP probe was in the plasma for approximately 500 microseconds, making it susceptible to ablation according to the model. Generally, degradation was not observed on shots in which the retro-sheet was believed not to have entered the plasma chamber (figures 5.28-5.32). This is particularly evident in figures 5.31 and 5.32. This data supports the conservative stance taken by the model. Shot 9306 (figure 5.29) showed a severe drop in current, but this may be an indication that the retro-sheet was following close behind the probe as it entered the plasma. Unfortunately, no confirming data is available to determine the location of the retro-sheet when no reflected signal is obtained.

When a signal is obtained, the retro-sheet is known to be on the probe. For probes with a retro-sheet, degradation of plasma current is consistently observed (Figures 5.20-5.28). The drop in current is delayed until approximately 200 micro-seconds of probe transit. This extended delay time was likely due to the mitigating effects of the ablation cloud which are not included in the model. Equally significant, sputtering of the surface, which occurs immediately, was not seen to affect plasma behavior indicating that the impurity loading to the plasma was not harmful. These observations are encouraging in that measurements of significantly more energetic plasmas could be undertaken with diamond protected probes, but these conclusions are qualitative.

### 5.5.3 Discussion of TIP Diagnostic Operation

The TIP diagnostic met the desired objectives of the research and development program. Several successful measurements of the internal toroidal field profile of the Helicity Injected Tokamak were achieved. As a result of this research, many new technologies and techniques were developed including a highly reliable gas gun acceleration system, compatible with tokamak operation, a new fast response polarimeter, and a refined gas dynamic sabot removal process. The combined result of these developments yielded a versatile

diagnostic able to measure magnetic fields in a plasma at two kilometers per second with a magnetic resolution of 2-3% over several meters, and a local resolution of +/- 20 gauss absolute. Time response of 10-100 Mhz depending on plasma conditions is possible with proper electronics.

Table 5.1 Summary of first TIP shots on HIT

| Ref. Number | Shot Number | Shot Description | Comments |
|---|---|---|---|
| 1 | n/a | Practice shot into exp. Tank | probe tumbled |
| 2 | n/a | Practice shot into exp. Tank | probe tumbled |
| 3 | n/a | Practice shot into exp. Tank | probe tumbled |
| 4 | n/a | Practice shot into exp. Tank | probe tumbled |
| 5 | n/a | Practice shot into exp. Tank | stable flight |
| 6 | n/a | Practice shot into exp. Tank | stable flight |
| 7 | 1045 (8113) | Vacuum shot into tokamak | probe hit inlet tubing, no tilt observed |
| 8 | 1047 (8120) | Vacuum shot into tokamak | Received data, tilt observed ~19 degrees |
| 9 | 1054 (8252) | Plasma shot into tokamak | Probe collided with exit tubing, severe tilt, no data obtained |
| 10 | 1071 (8277) | Plasma shot into tokamak | Probe collided with exit tubing, severe tilt, no data obtained |
| 11 | 1077 (8293) | Plasma shot into tokamak | Probe collided with exit tubing, severe tilt, no data obtained |
| 12 | n/a | Practice shot into exp. Tank | stable flight |
| 13 | n/a | Practice shot into exp. Tank | stable flight |
| 14 | n/a | Practice shot into exp. Tank | stable flight |

*Shots in parentheses refer to HIT log numbers

Table 5.2 Summary of second TIP shots on HIT

| Ref. Number | Shot Number | Shot Description | Comments |
|---|---|---|---|
| 1 | 9231 (1) | Plasma shot into tokamak | Stable probe flight, good data obtained, arrived early in plasma |
| 2 | 9238 (2) | Plasma shot into tokamak | Stable probe flight, good data obtained, arrived late in plasma |
| 3 | 9239* | Vacuum shot into tokamak | Probe tilted, but data obtained, strong laser oscillations |
| 4 | 9272 | Plasma shot into tokamak | Metallic backing on probe, no data , retro-sheet likely off |
| 5 | 9279 | Plasma shot into tokamak | Metallic backing on probe, no data , retro-sheet likely off |
| 6 | 9289 | Plasma shot into tokamak | Laser blocked preventing probe illumination |
| 7 | 9306 | Plasma shot into tokamak | No metallic backing, still no data, retro-sheet likely came off |
| 8 | 9313 | Vacuum shot into tokamak | Sabot separation system leaked and probe destroyed in exp. tank |
| 9 | 9320 | Vacuum shot into tokamak | No metallic backing, still no data, retro-sheet likely came off |
| 10 | 9324 | Vacuum shot into tokamak | No metallic backing, still no data, retro-sheet likely came off |
| 11 | 9327 | Vacuum shot into tokamak | Laser illumination power dropped to nil at time of fire |
| 12 | 9334* | Vacuum shot into tokamak | Severe probe tilt, but data obtained |
| 13 | 9354 | Plasma shot into tokamak | No metallic backing, still no data, retro-sheet likely came off |
| 14 | 9363 (3) | Plasma shot into tokamak | Stable flight, data obtained, probe entered plasma at current peak |
| 15 | 9370 | Plasma shot into tokamak with no probe | Sabot only shot |

*Vacuum shots in which data was obtained.

**Bold numbers refer to the three plasma shots where data was obtained.**

Table 5.3 Summary of shots taken on HIT with new Optical Detection System

| Ref. Number | Shot Number | Shot Description | Comments |
|---|---|---|---|
| n/a | 9389 | Plasma shot into tokamak | Data obtained, but late |
| n/a | 9398 | Vacuum shot into tokamak | No data, retro sheet likely came off |
| n/a | 9403 | Plasma shot into tokamak | Stable flight, data obtained, probe entered plasma at current peak |
| n/a | 9407 | Vacuum shot into tokamak | Poor illumination data not obtained |
| n/a | 9413 | Plasma shot into tokamak | Good data obtained, probe entered plasma near peak current |
| n/a | 9416 | Vacuum shot into tokamak | Poor illumination data not obtained |
| n/a | 9318 | Vacuum shot into tokamak | Some tilting, but vacuum data obtained |
| n/a | 9425 | Plasma shot into tokamak | Poor illumination but data was obtained |
| n/a | 9458 | Plasma shot into tokamak | Good data obtained |
| n/a | 9479 | Plasma shot into tokamak | Extremely low reflected intensity, status of retro-sheet unknown |
| n/a | 9511 | Plasma shot into tokamak | Sabot stripping system leaked and probe did not strip |
| n/a | 9540 | Plasma shot into tokamak | Good data obtained, but probe entered plasma late |
| n/a | 9548 | Plasma shot into tokamak | Data obtained but illumination was poor |

NOTE: These shots are included for discussion of probe effects on the plasma. Measurement results from these shots will be included in separate papers and reports by Micheal A. Bohnet.

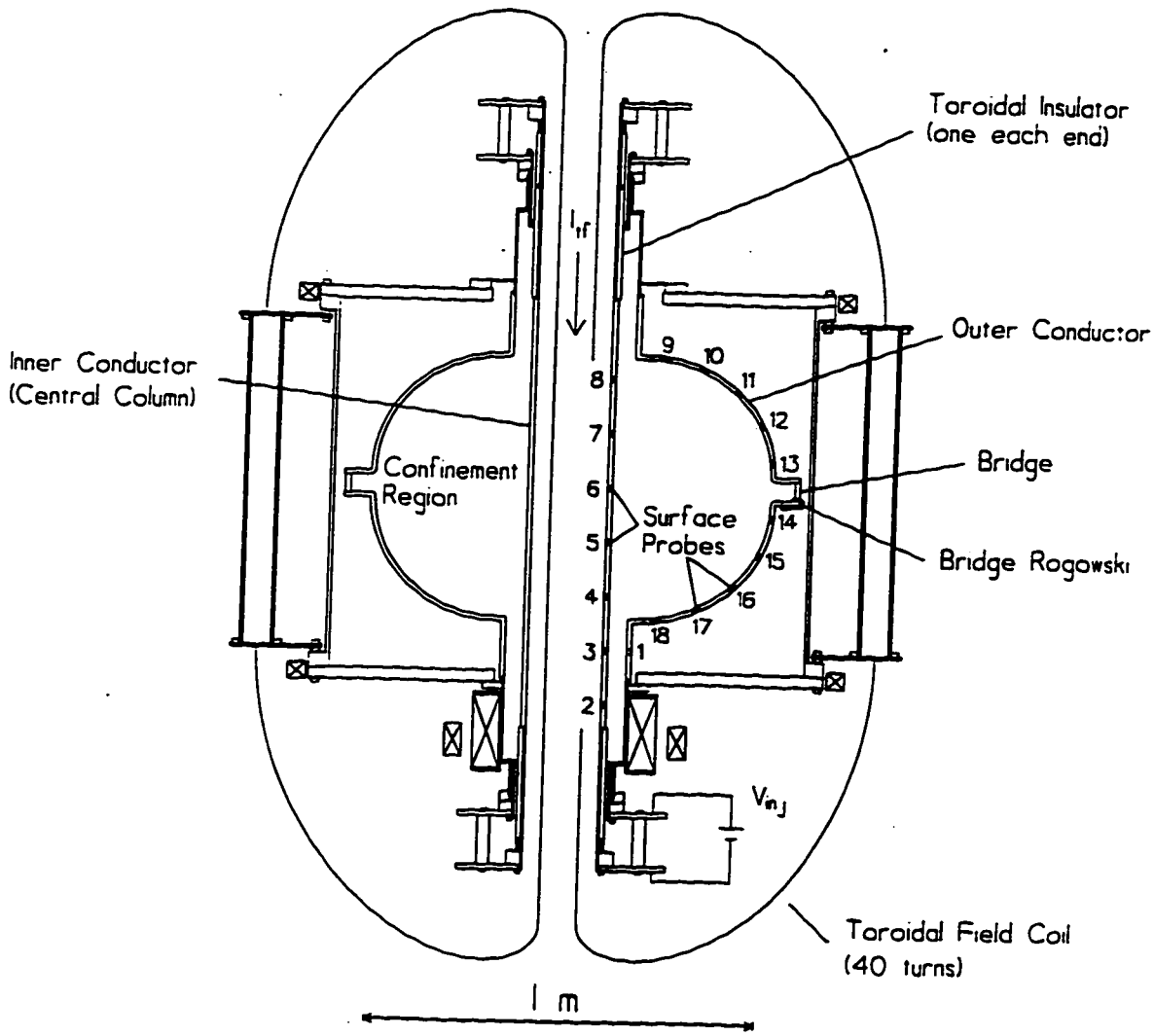


**Figure 5.1 Top view of Helicity Injected Tokamak.**

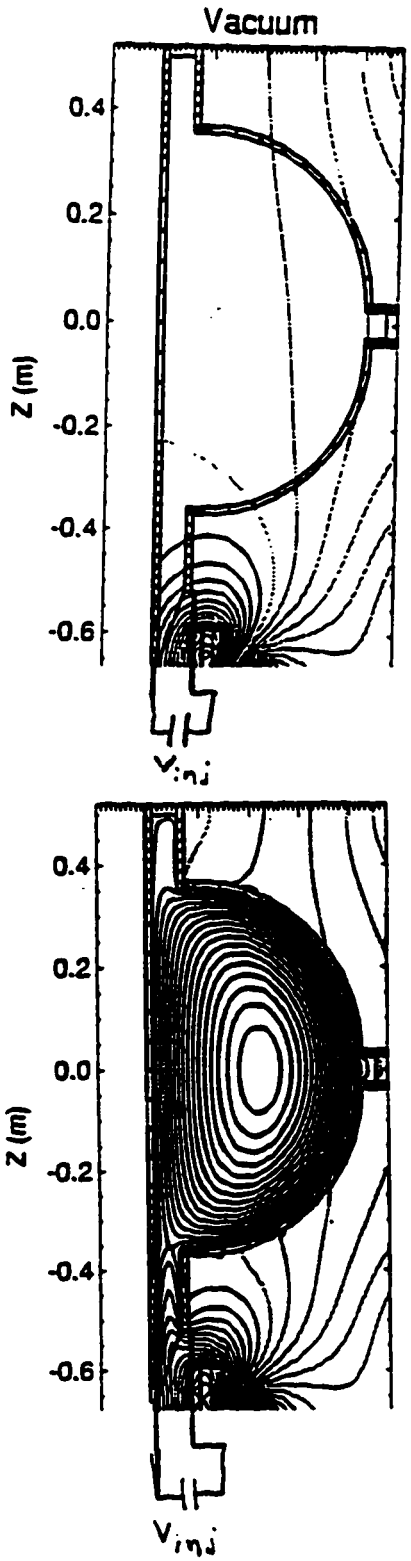


Figure 5.2a,b Plasma formation and sustainment in HIT.

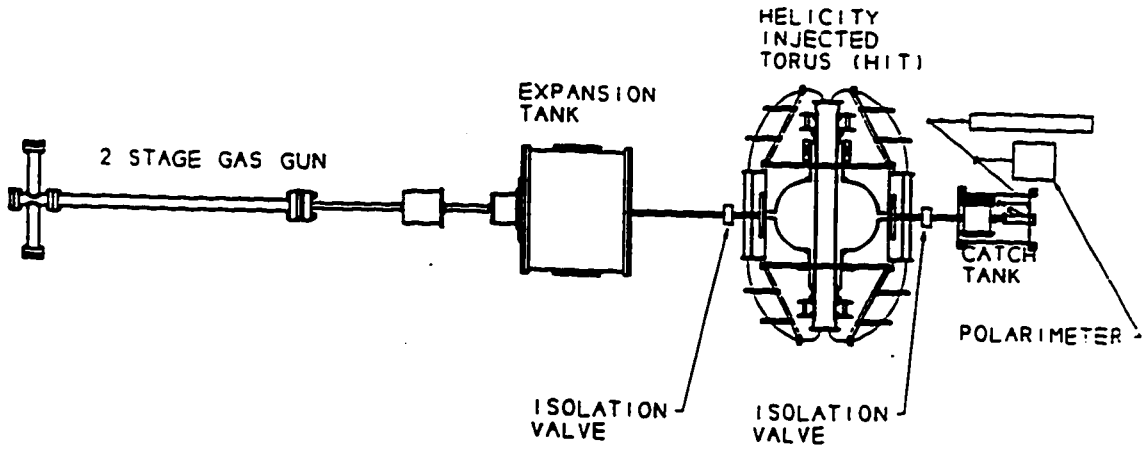


Figure 5.3 Schematic of TIP diagnostic installed on the Helicity Injected Tokamak.

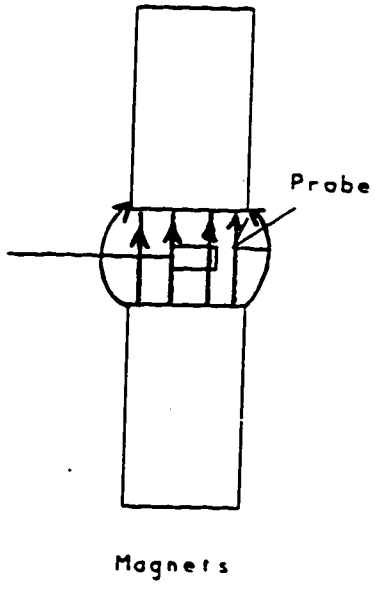


No tilt, probe "see's" only fringe fields

(a)

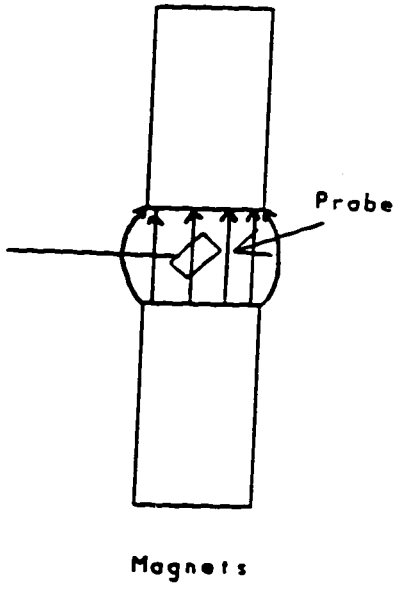


Probe tilts and sees large transverse field

$B_{meas} = B_{mag} Sin(\theta)$, $B_{mag}$ ~3000 G.

(b)

Figure 5.4 Diagram of cross field magnets used to determine probe tilt and yaw. (a) No tilt, probe "sees" only fringe fields at as it enters and exits magnets. (b) Probe tilted

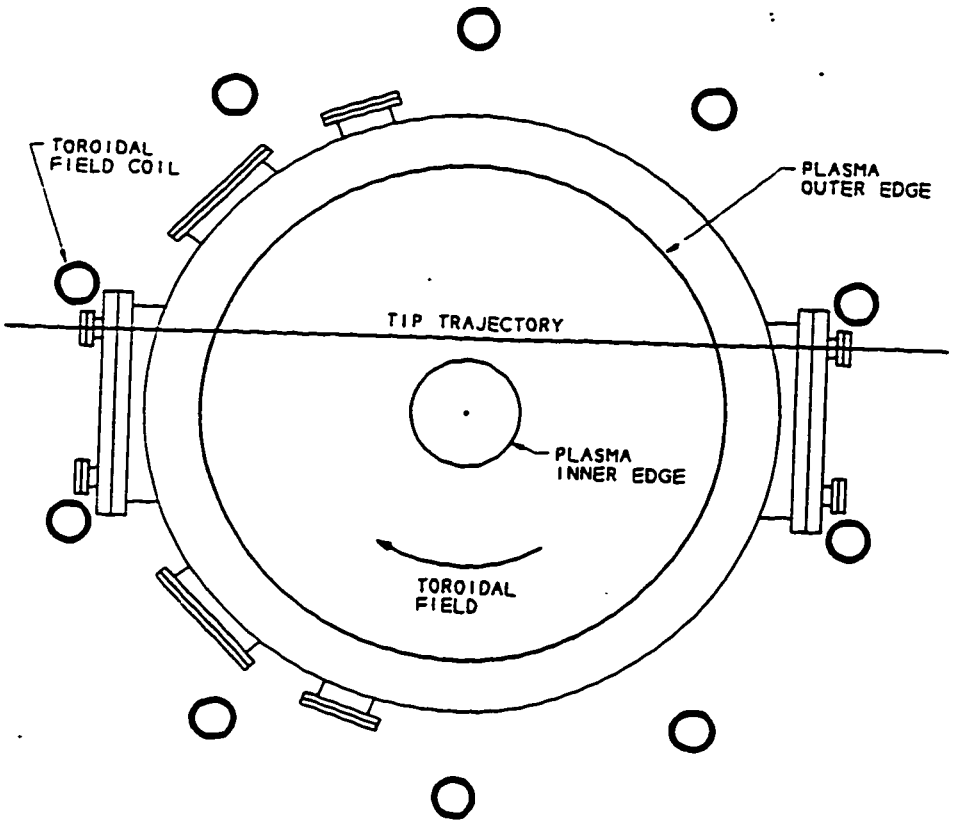


Figure 5.5 Trajectory of TIP probe as it passes through the tokamak showing the relative position of the torroidal field coils and return bundles.

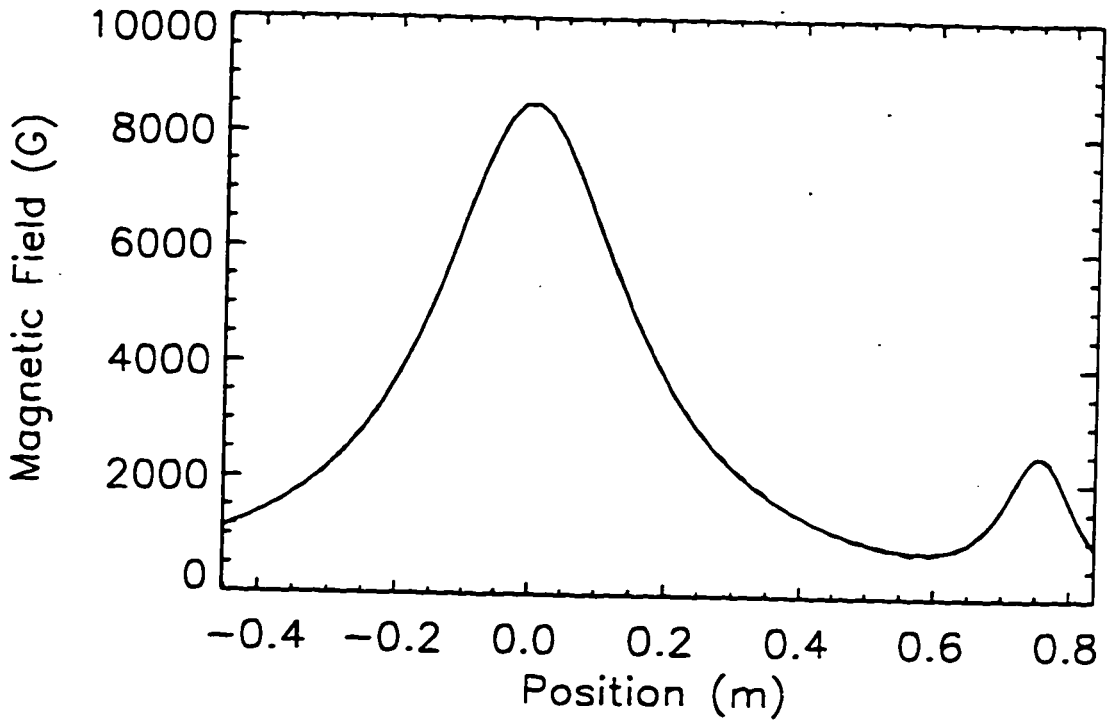


Figure 5.6a Plot of vacuum toroidal magnetic field measured with Hall probe with calculated vacuum field overlaid. .

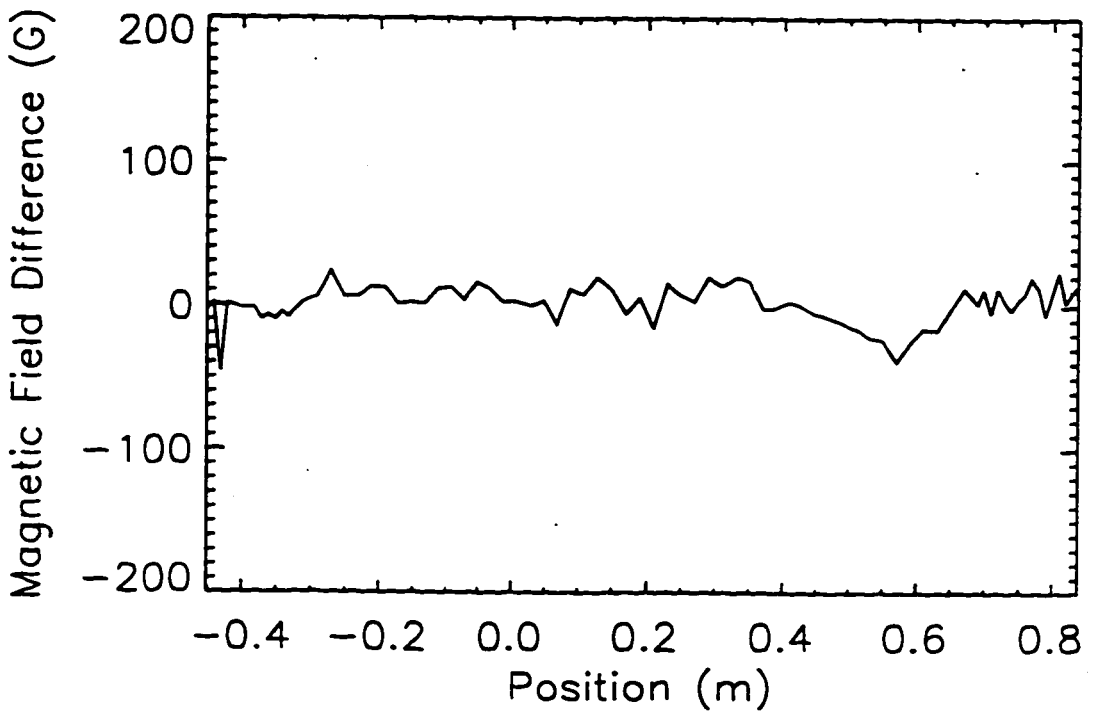


Figure 5.6b Residual difference between Hall probe data and calculated magnetic field.

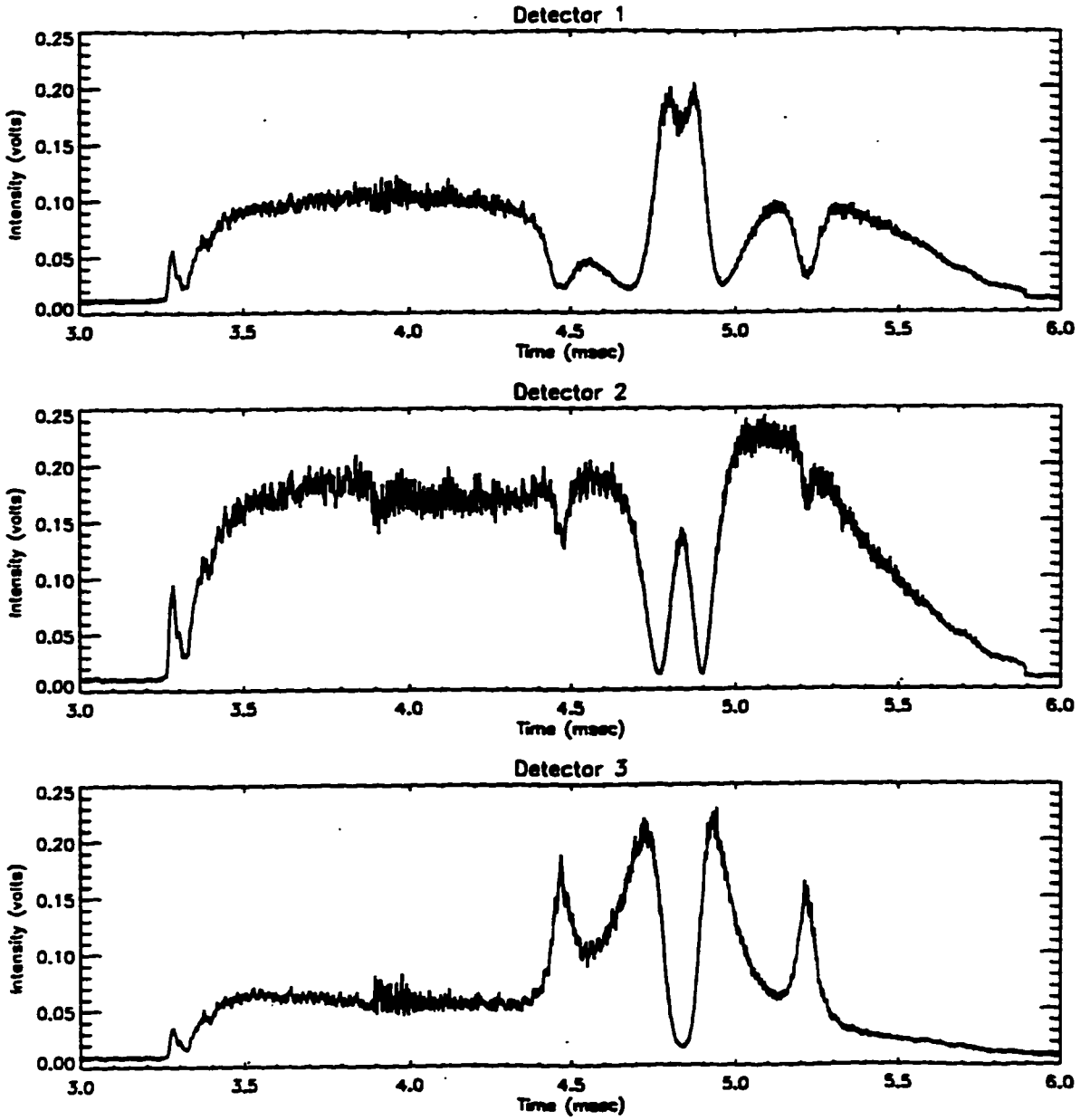


Figure 5.7 Raw data recorded during 1st measurement of vacuum magnetic field using the TIP diagnostic

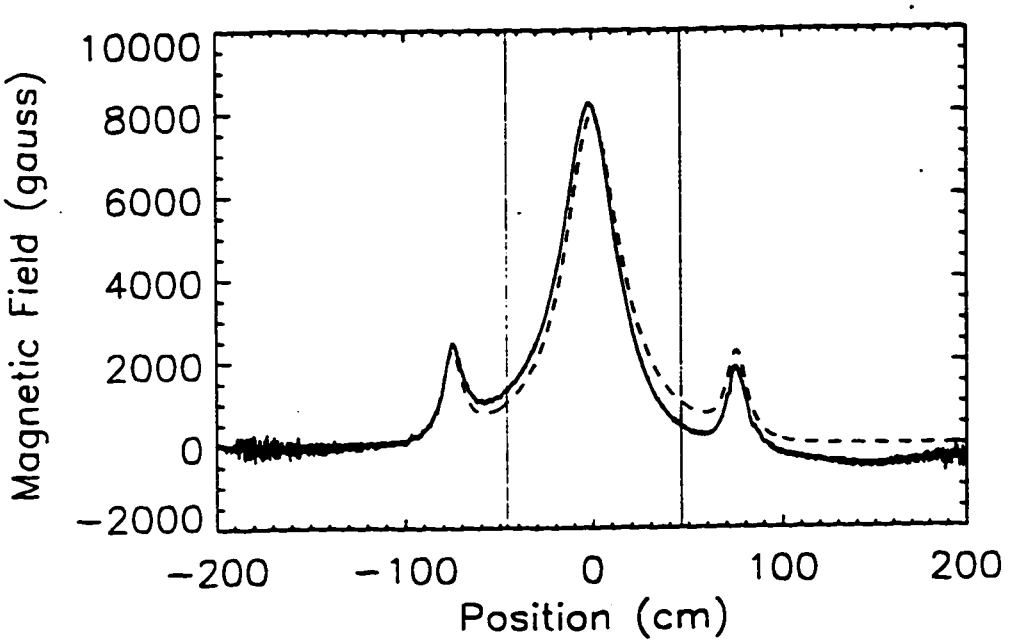


Figure 5.8a Plot of uncorrected 1st TIP measurement of vacuum magnetic field with calculated vacuum field overlaid.

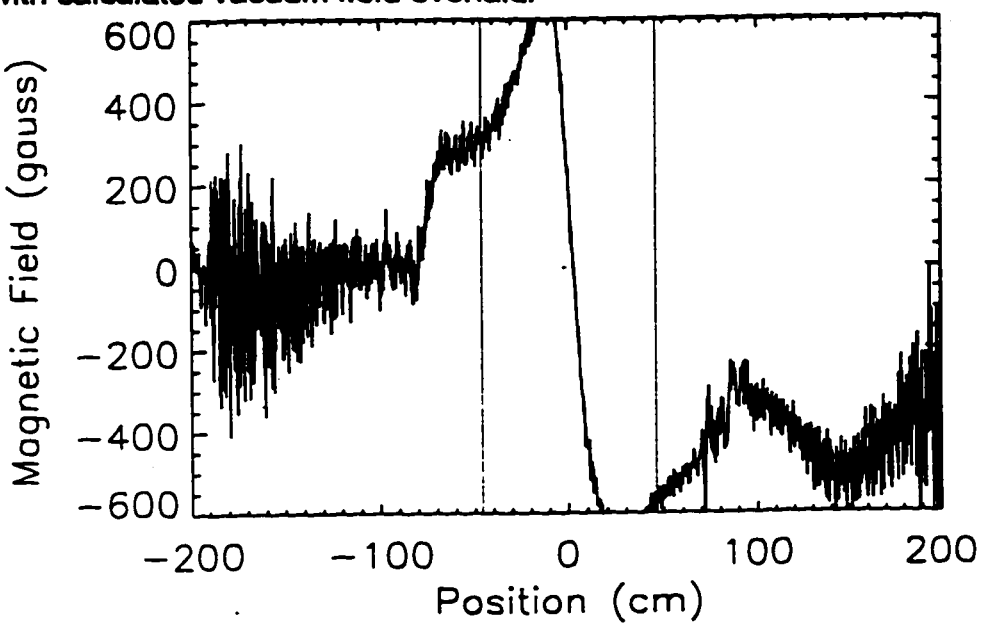


Figure 5.8b Residual difference between uncorrected 1st TIP measurement and calculated magnetic field.

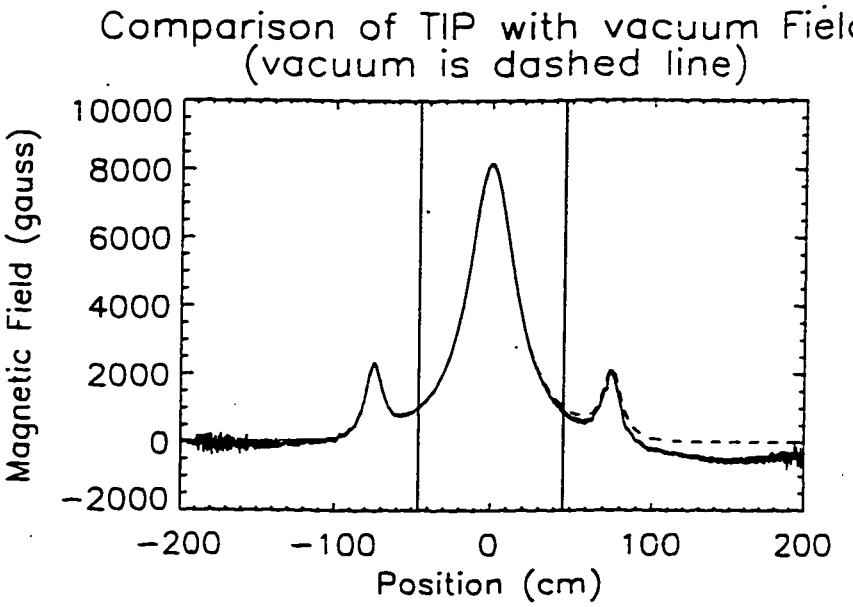


**Figure 5.9a Plot of corrected 1st TIP measurement of vacuum magnetic field with calculated vacuum field overlaid.**

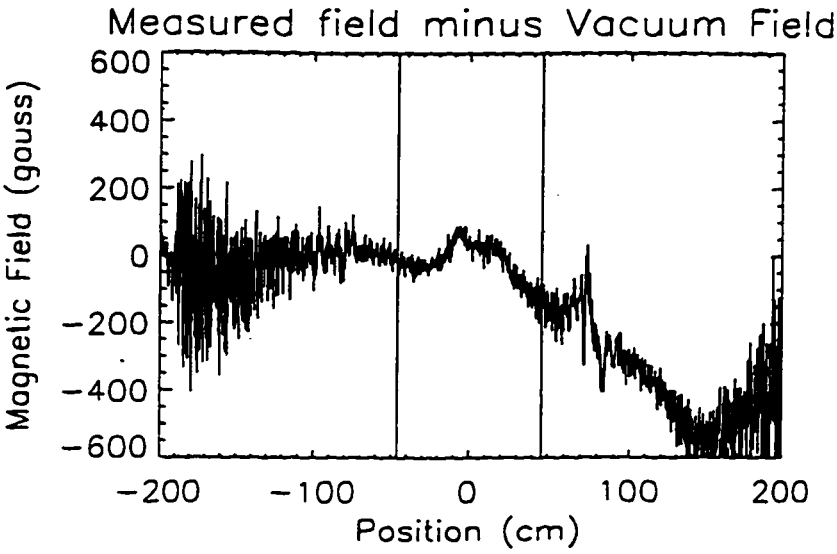


**Figure 5.9b Residual difference between corrected 1st TIP measurement and calculated magnetic field.**

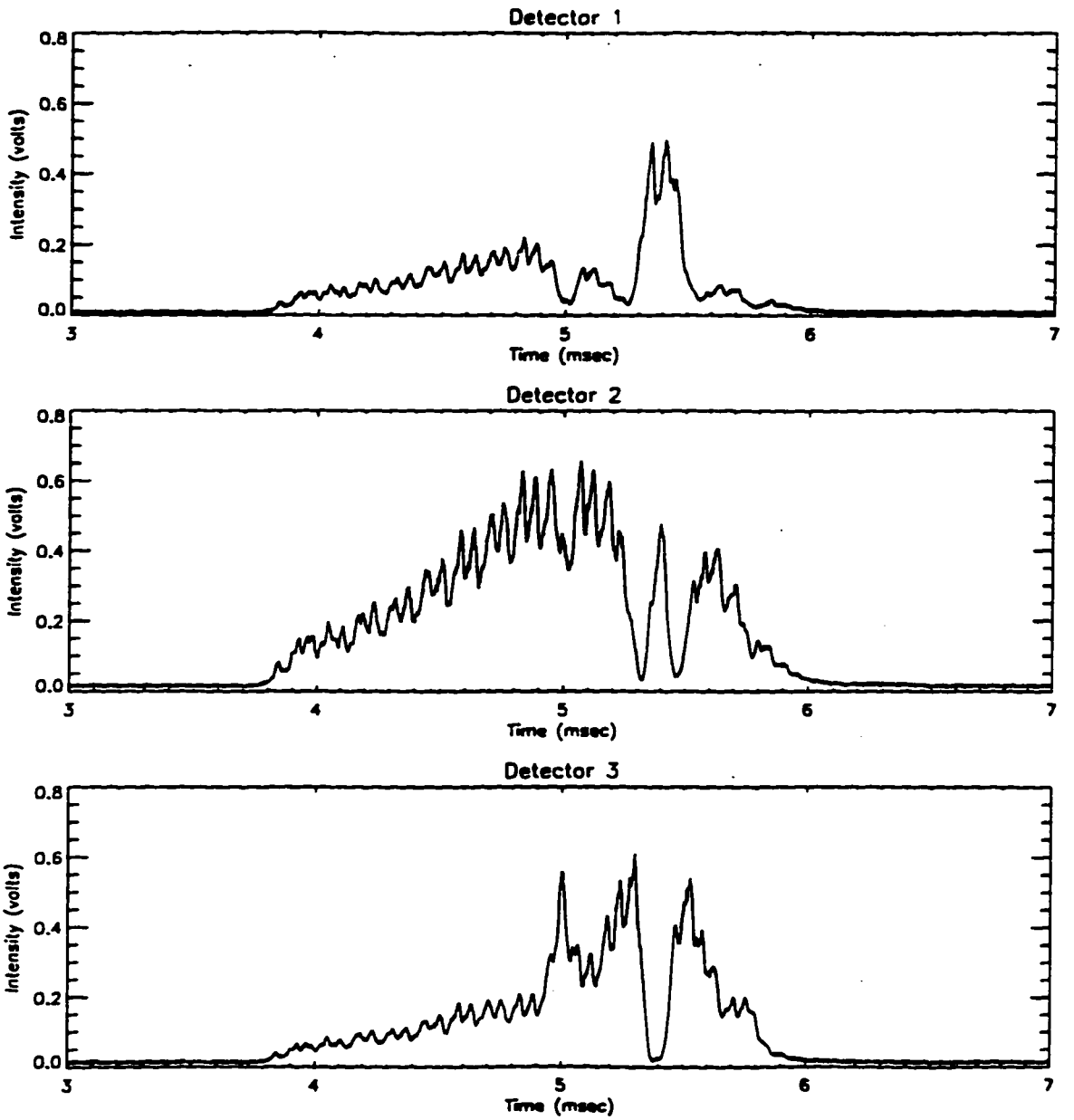


Figure 5.10 Raw data recorded during 2nd measurement of vacuum magnetic field using the TIP diagnostic

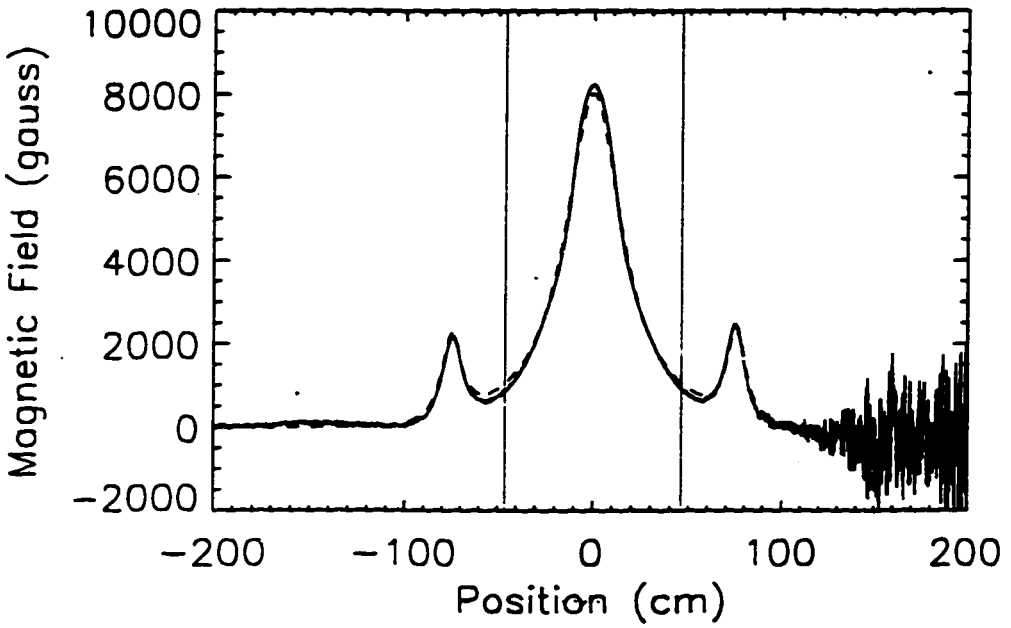


Figure 5.11a Plot of corrected TIP measurement of 2nd vacuum magnetic field with calculated vacuum field overlaid.

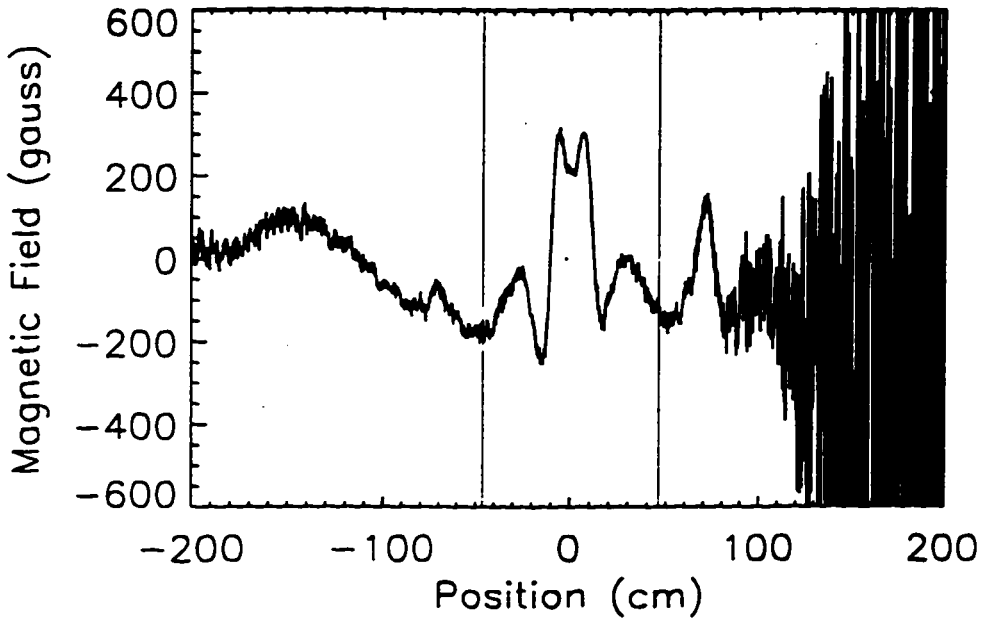


Figure 5.11b Residual difference between corrected 2nd TIP measurement and calculated magnetic field.

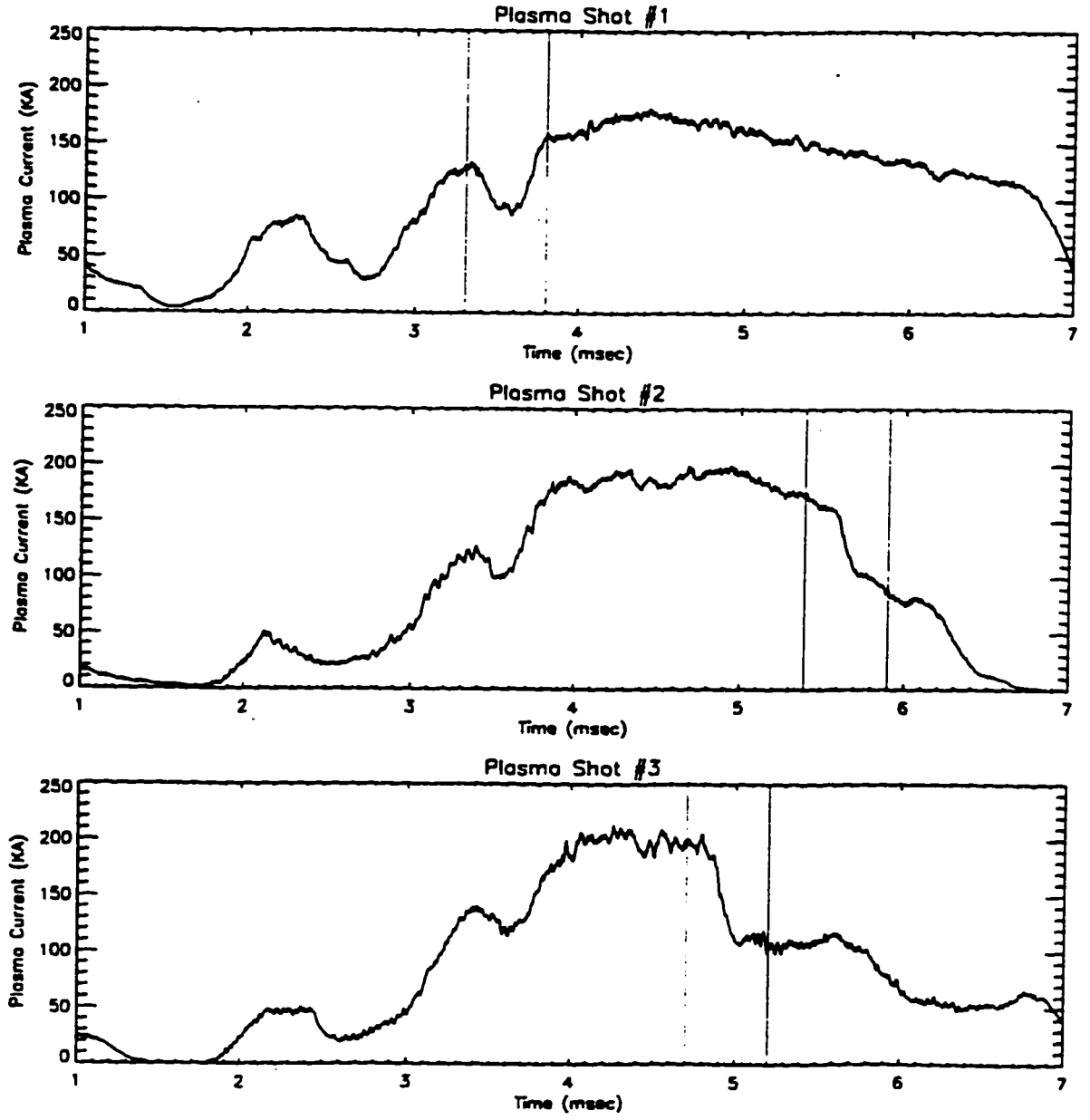


Figure 5.12a,b,c Plot of plasma current versus time for each of three TIP measurements in the plasma. Vertical lines depict probe presence in plasma.

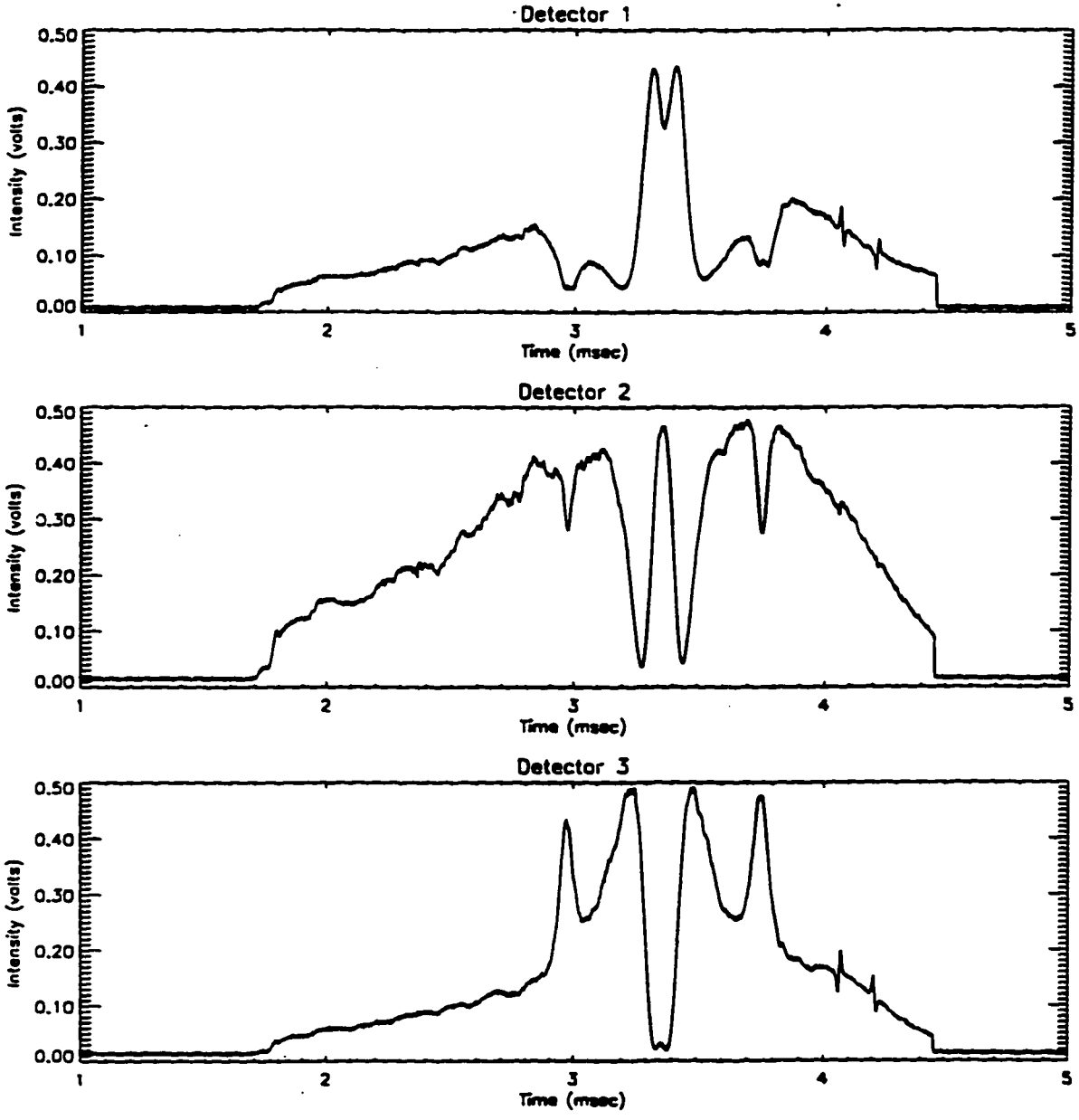


Figure 5.13 Raw data recorded during 1st measurement of plasma magnetic field using the TIP diagnostic

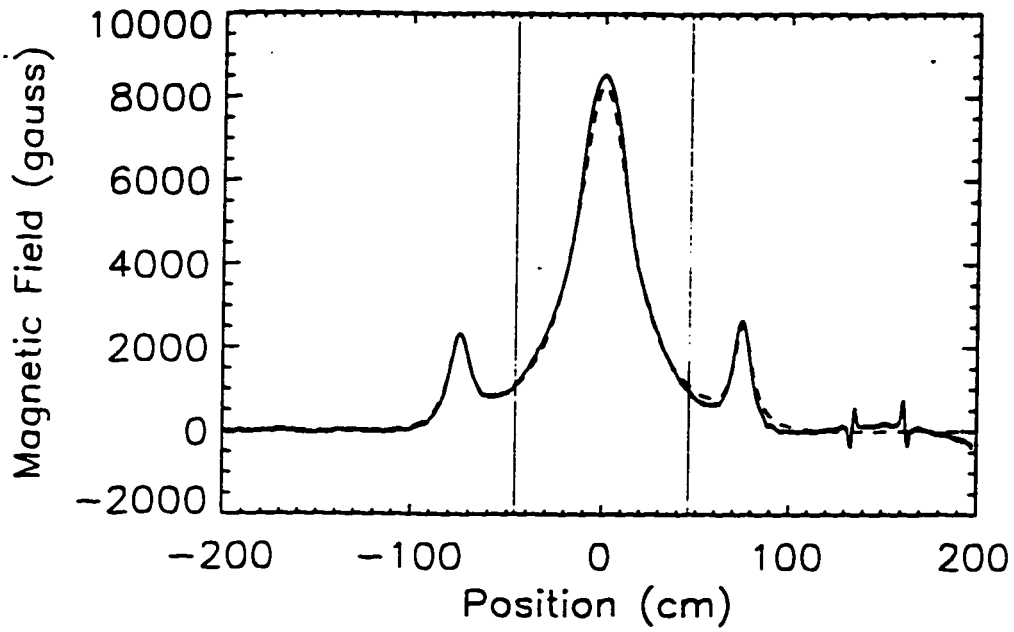


Figure 5.14a Plot of corrected 1st TIP measurement of plasma magnetic field with calculated vacuum field overlaid.

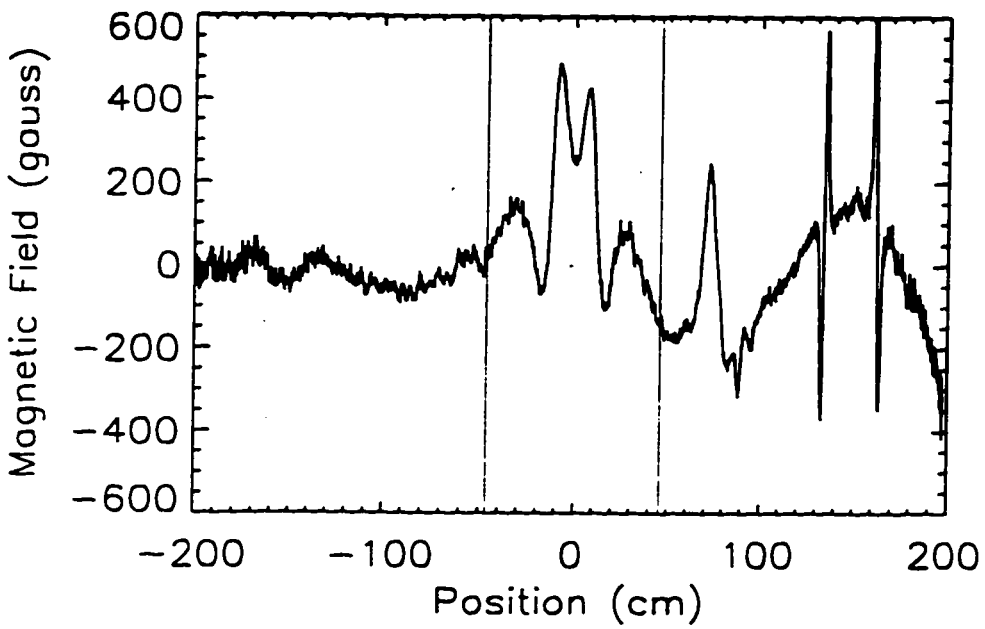


Figure 5.14b Residual difference between corrected 1st TIP plasma measurement and calculated magnetic field.

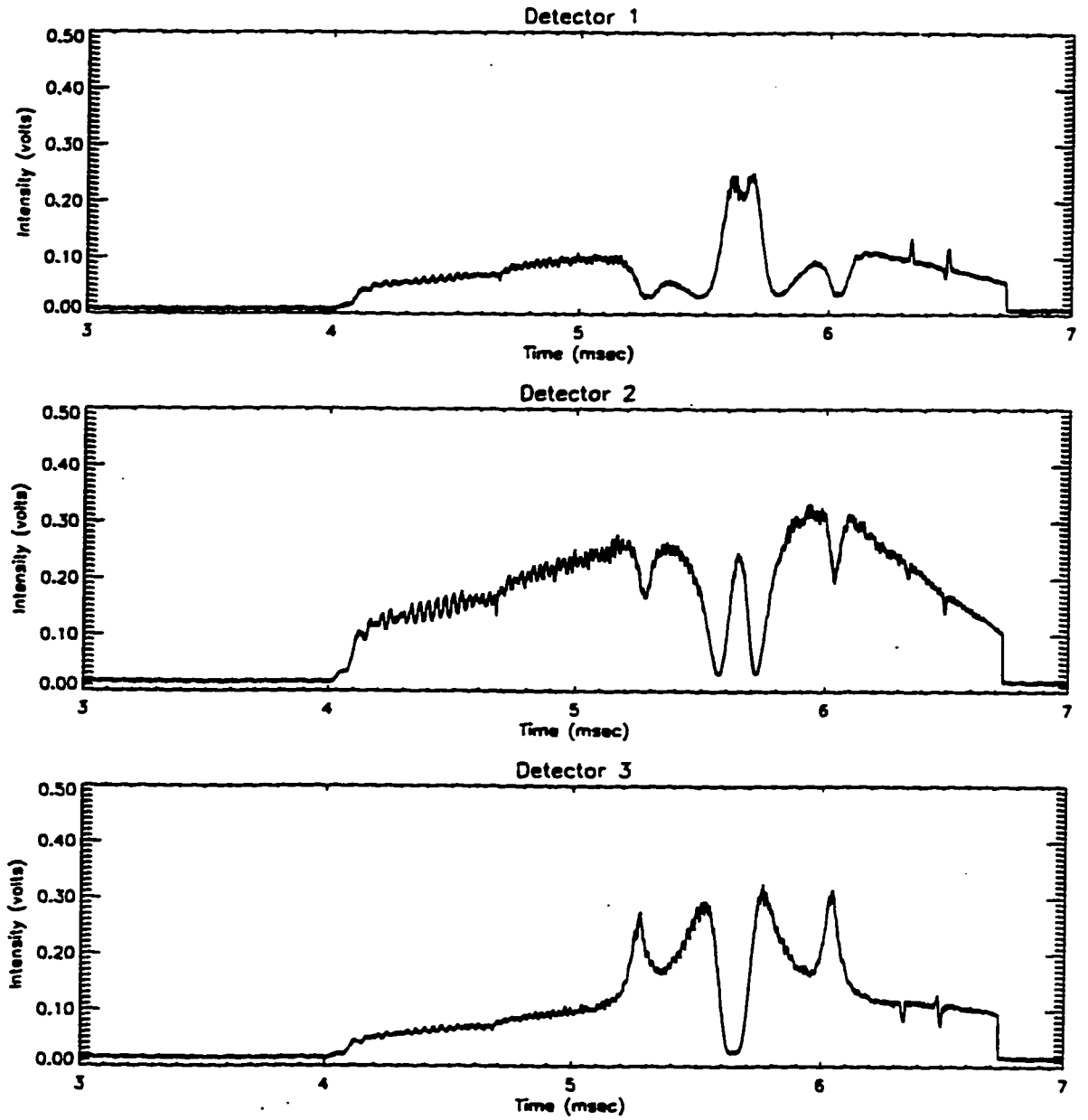


Figure 5.15 Raw data recorded during 2nd measurement of plasma magnetic field using the TIP diagnostic.

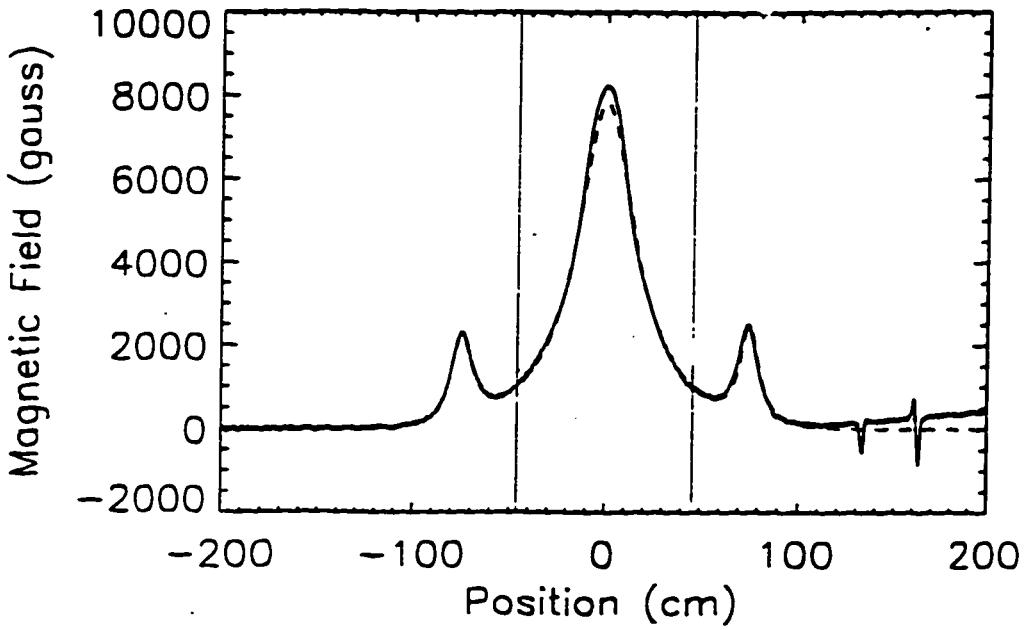


**Figure 5.16a Plot of corrected TIP 2nd measurement of plasma magnetic field with calculated vacuum field overlaid.**

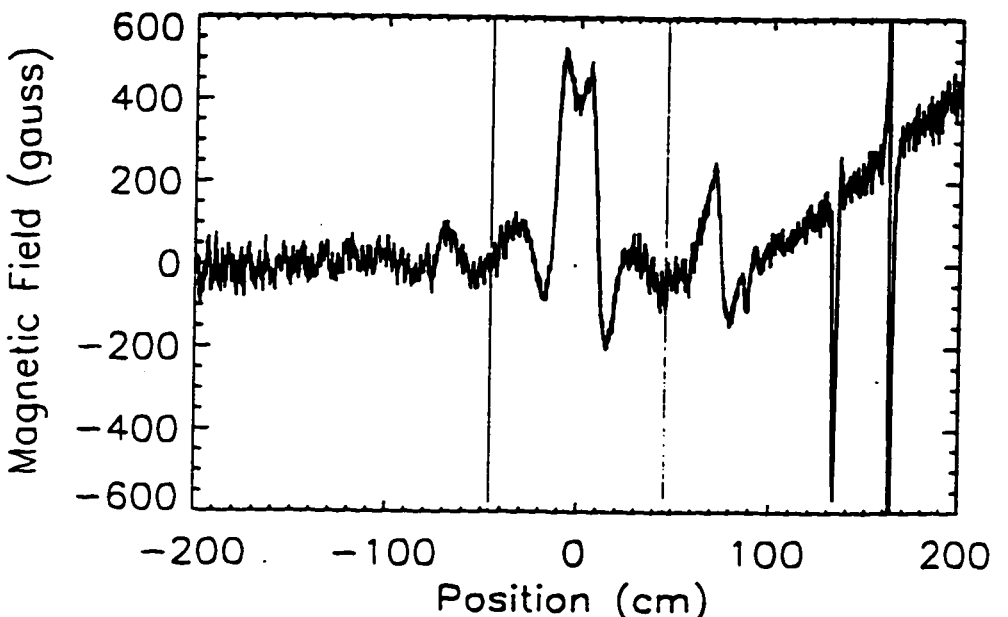


**Figure 5.16b Residual difference between corrected 2nd TIP plasma measurement and calculated magnetic field.**

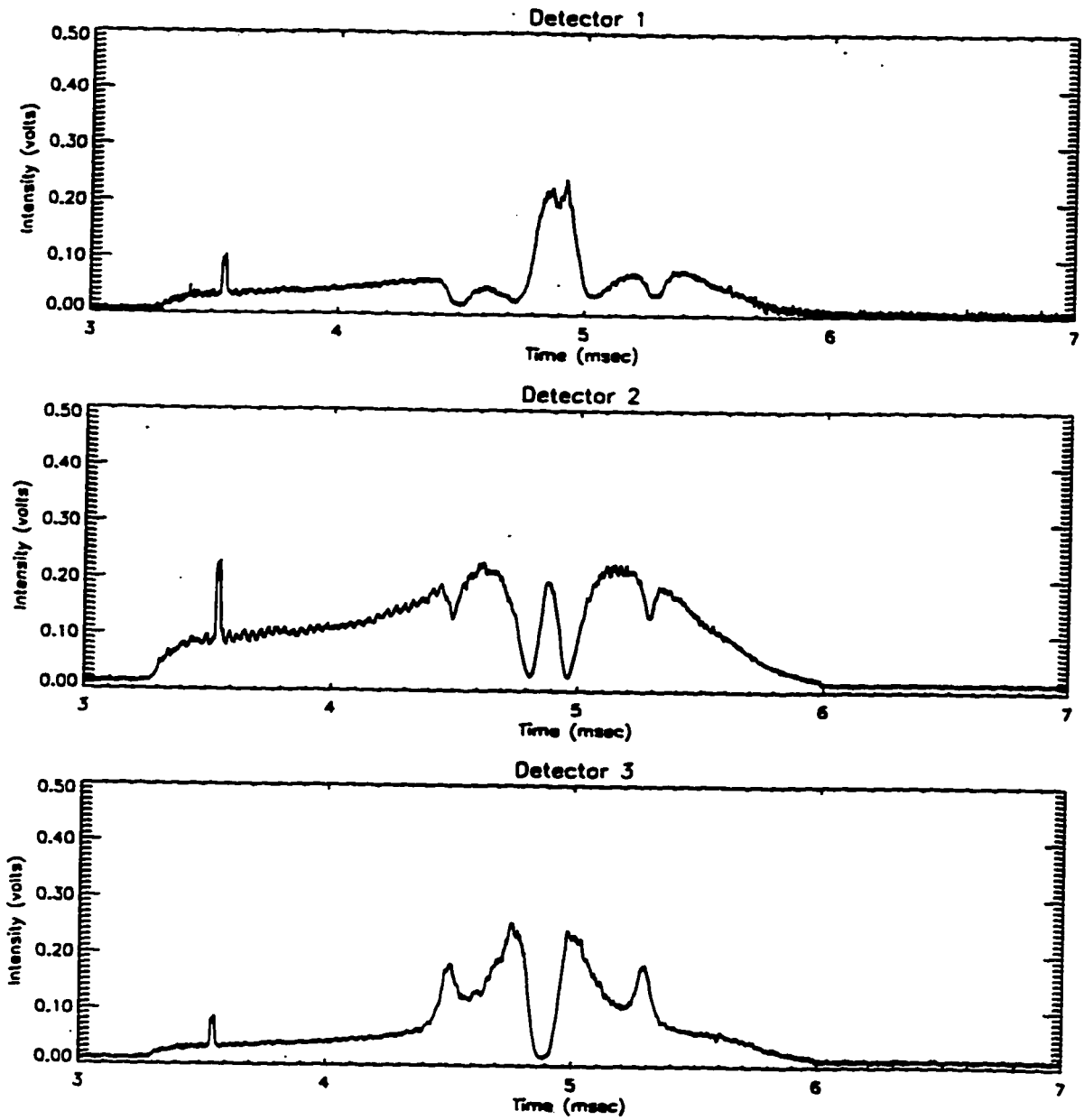


Figure 5.17 Raw data recorded during 3rd measurement of plasma magnetic field using the TIP diagnostic.

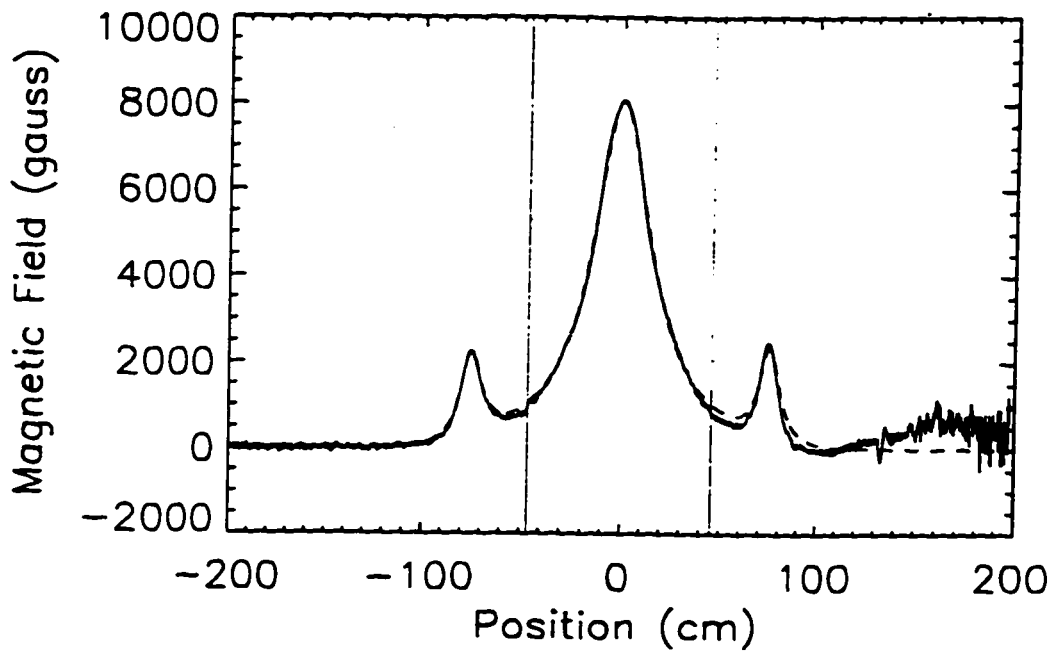


Figure 5.18a Plot of corrected TIP 3rd measurement of plasma magnetic field with calculated vacuum field overlaid.

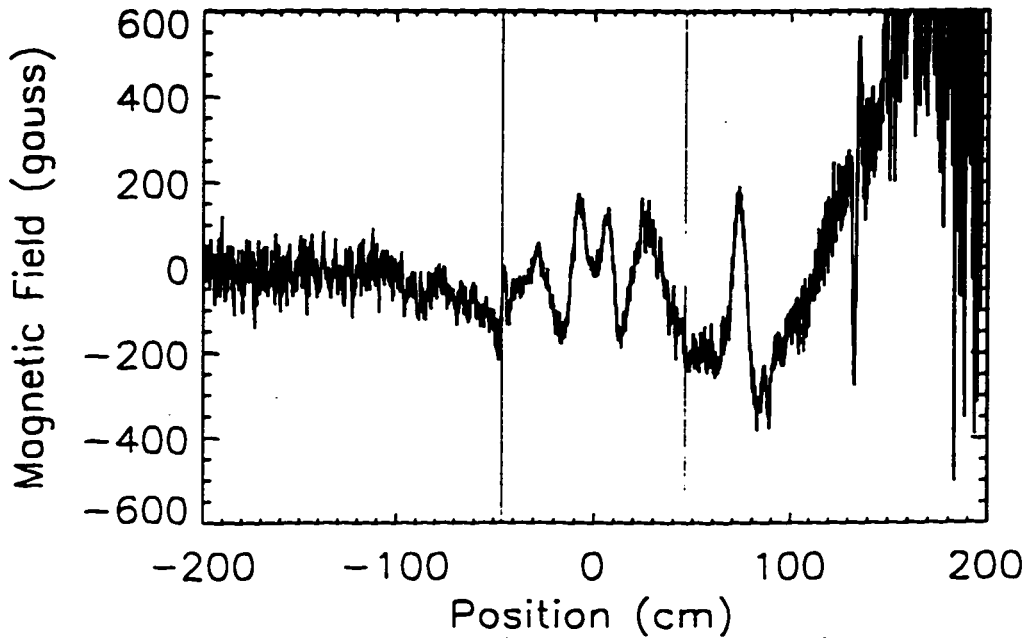


Figure 5.18b Residual difference between corrected 3rd TIP plasma measurement and calculated magnetic field.

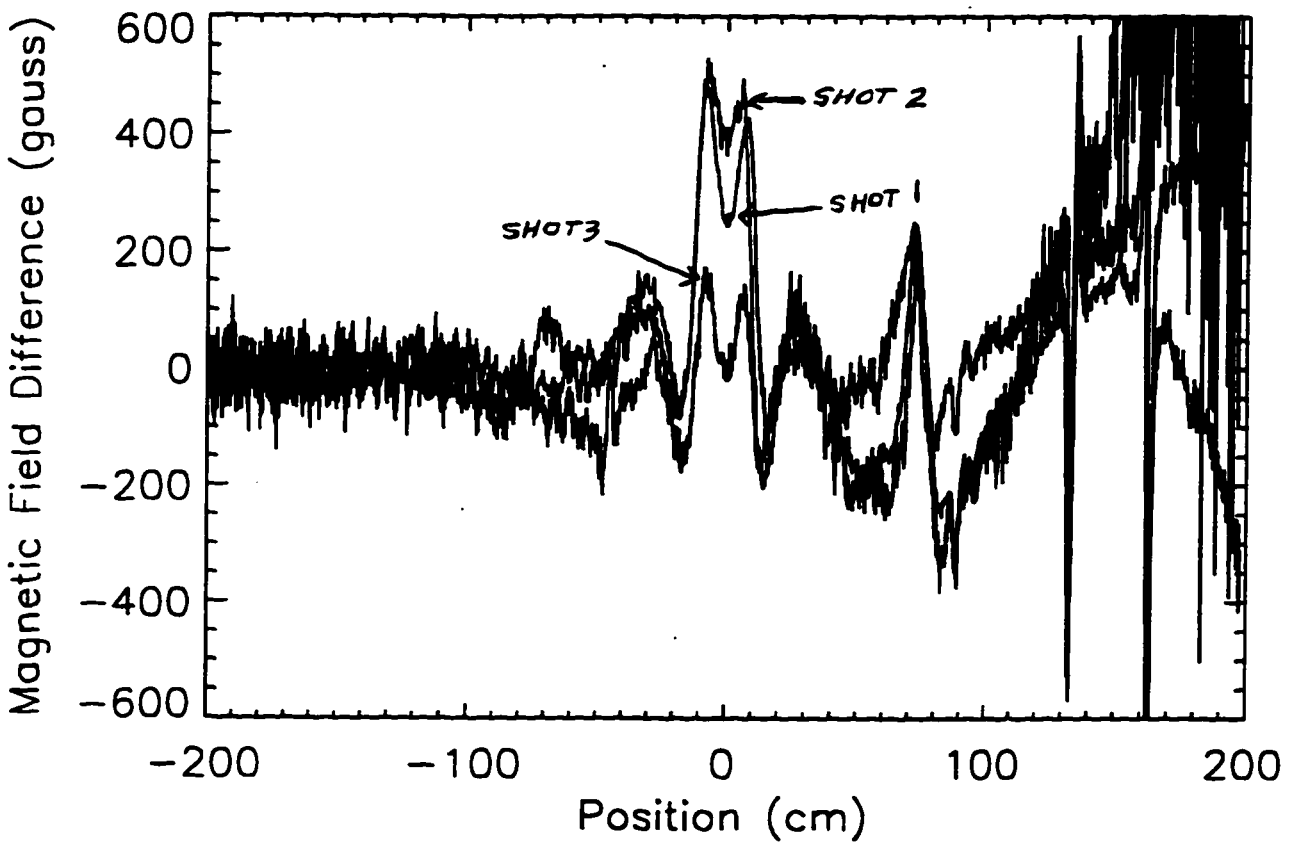


Figure 5.19 Plot of all three plasma measurement residual differences from the calculated vacuum magnetic field.

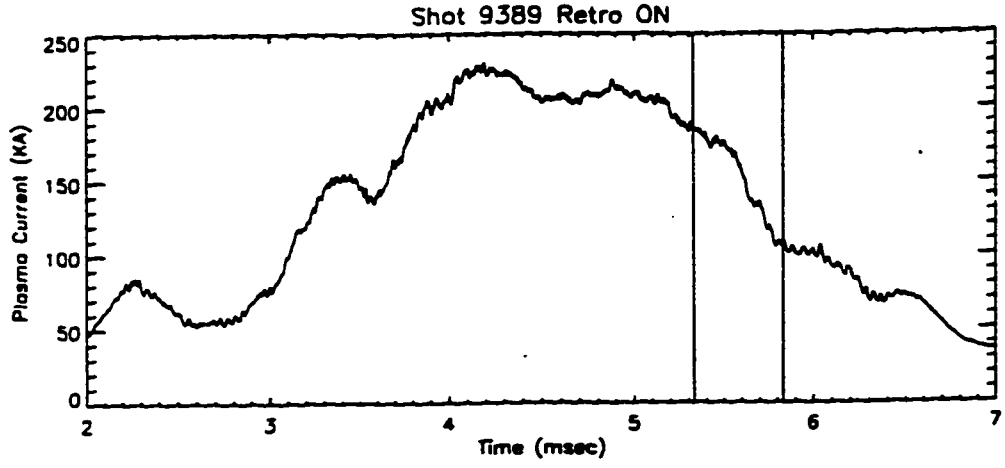


Figure 5.20 Plasma current versus time for shot 9389 for probe in plasma with retro-reflecting sheet.

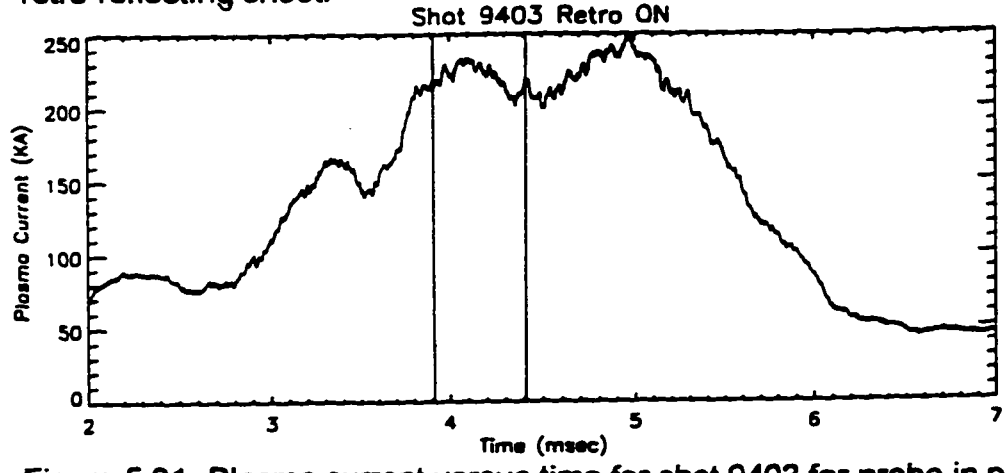


Figure 5.21 Plasma current versus time for shot 9403 for probe in plasma with retro-reflecting sheet.

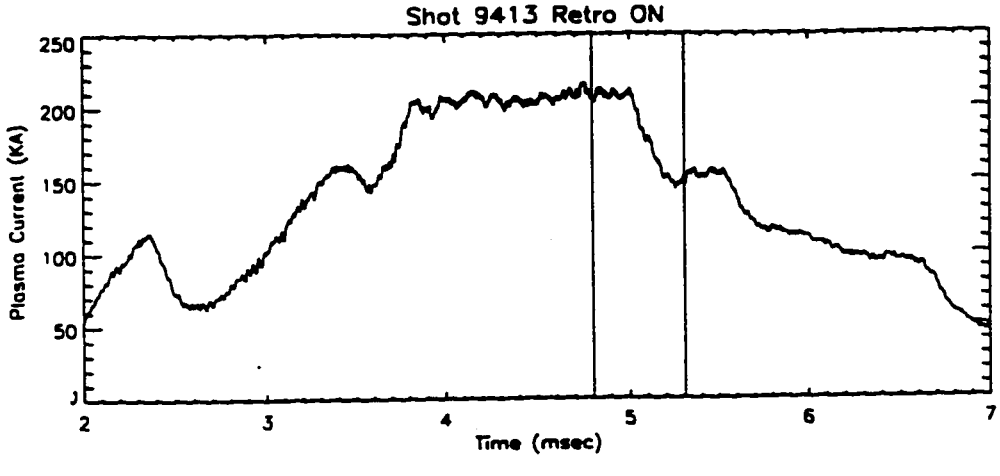


Figure 5.22 Plasma current versus time for shot 9413 for probe in plasma with retro-reflecting sheet.

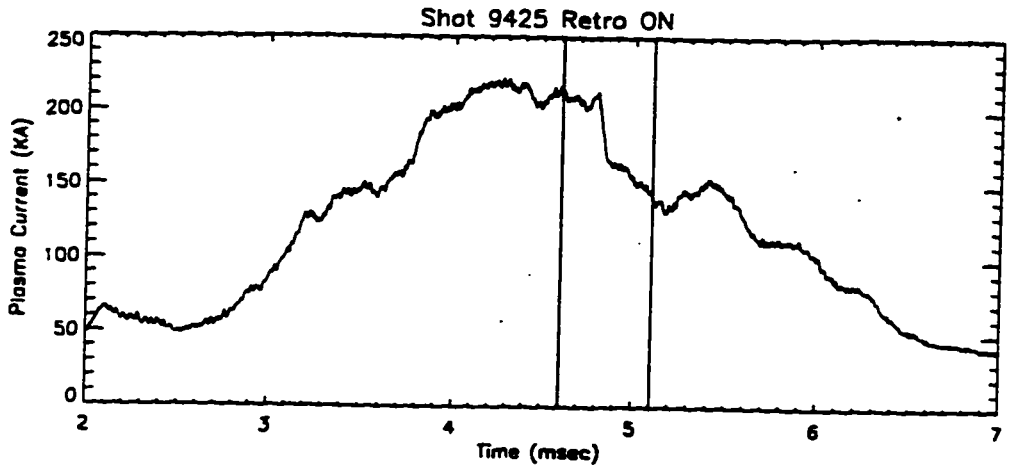


Figure 5.23 Plasma current versus time for shot 9425 for probe in plasma with retro-reflecting sheet.

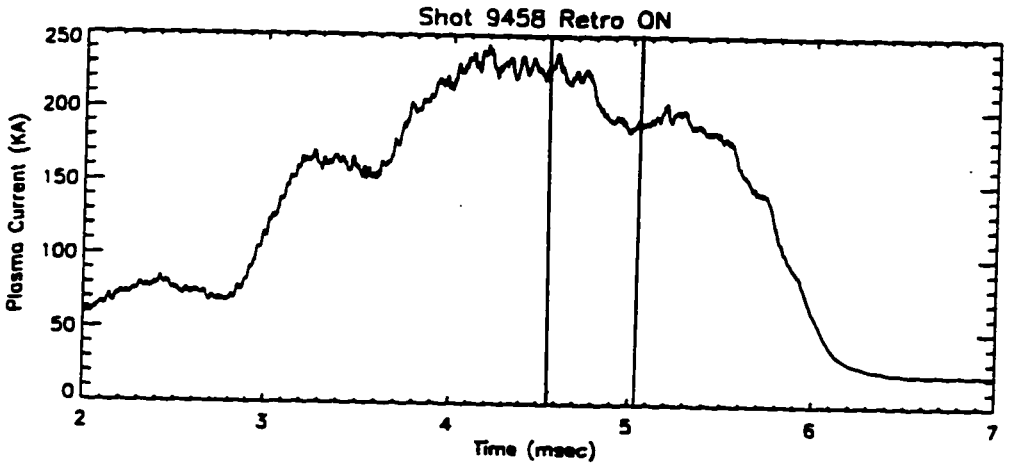


Figure 5.24 Plasma current versus time for shot 9458 for probe in plasma with retro-reflecting sheet.

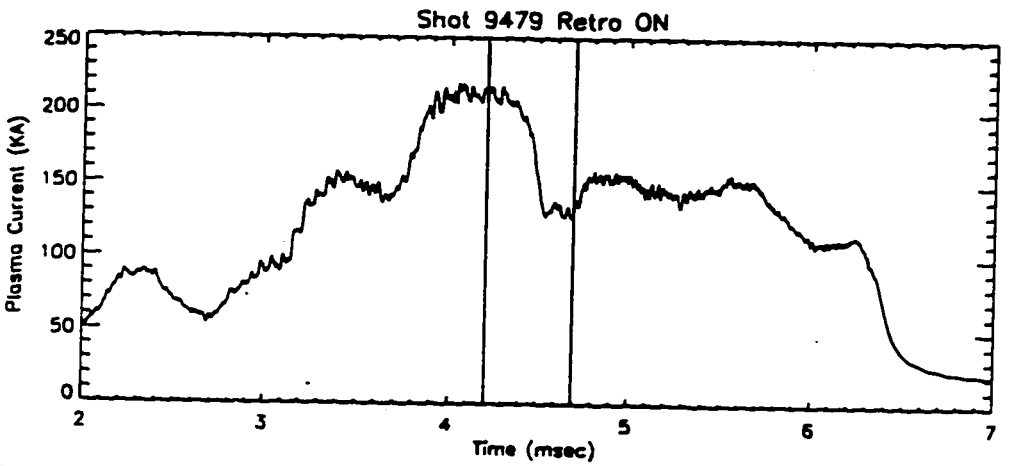


Figure 5.25 Plasma current versus time for shot 9479 for probe in plasma with retro-reflecting sheet.

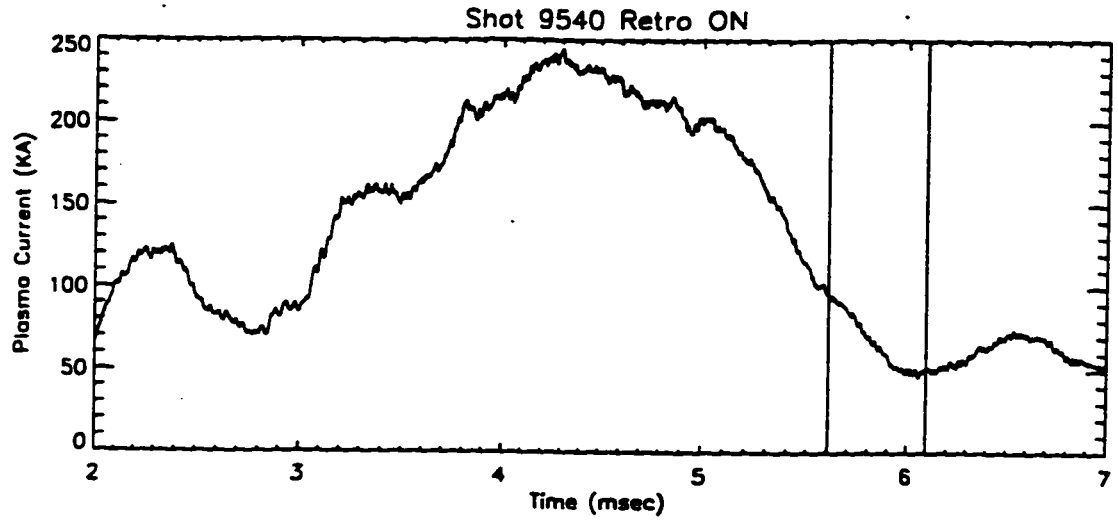


Figure 5.26 Plasma current versus time for shot 9540 for probe in plasma with retro-reflecting sheet.

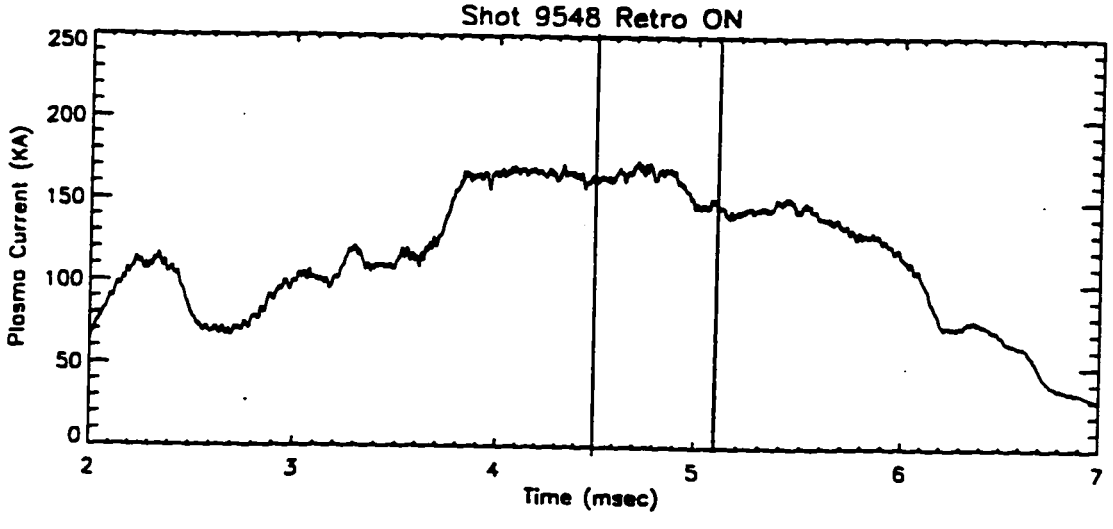


Figure 5.27 Plasma current versus time for shot 9548 for probe in plasma with retro-reflecting sheet.

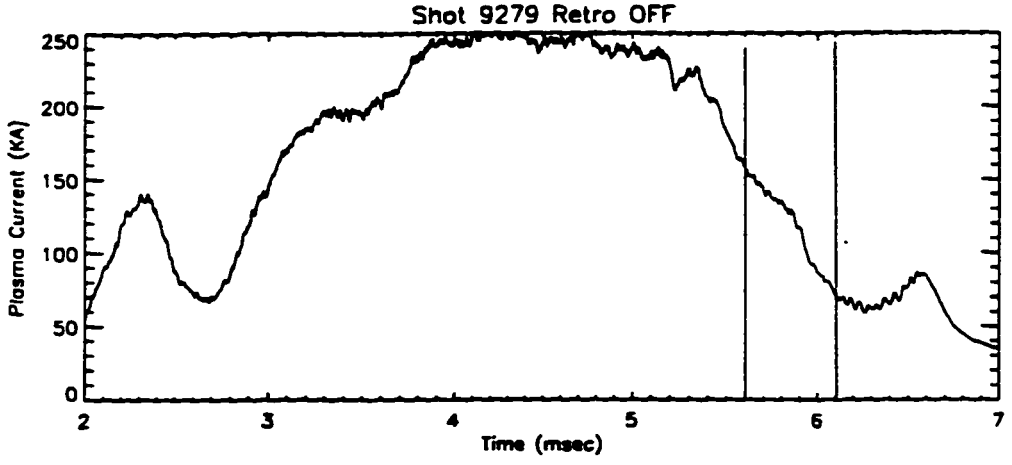


Figure 5.28 Plasma current versus time for shot 9279 for probe in plasma with no retro-reflecting sheet.

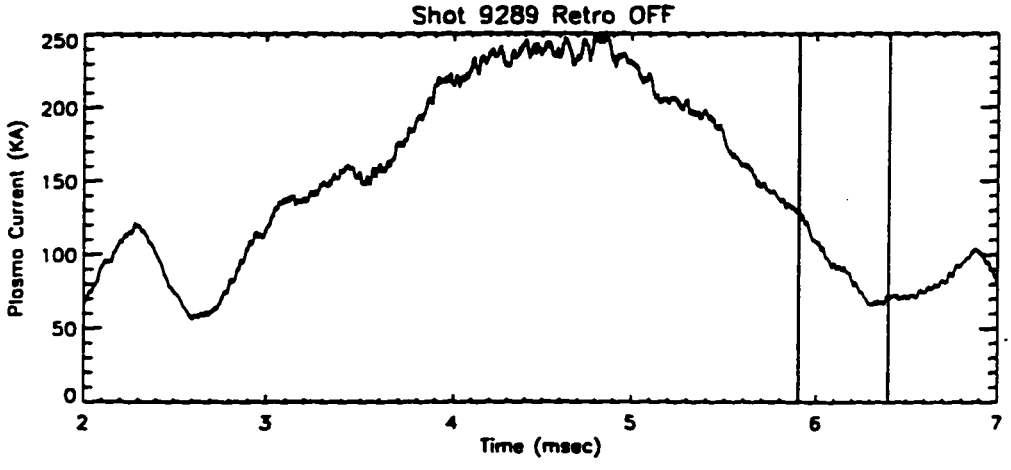


Figure 5.29 Plasma current versus time for shot 9289 for probe in plasma with no retro-reflecting sheet.

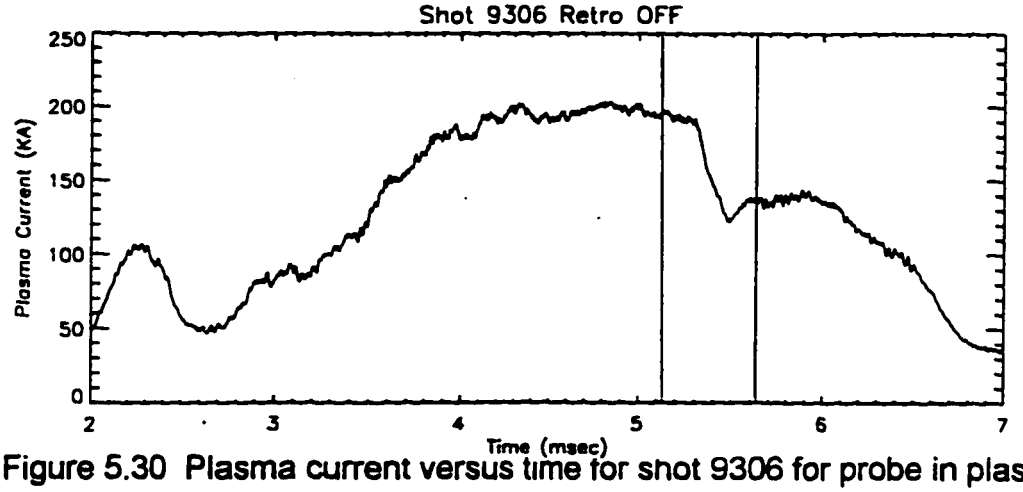


Figure 5.30 Plasma current versus time for shot 9306 for probe in plasma with status of retro-reflecting sheet unknown.

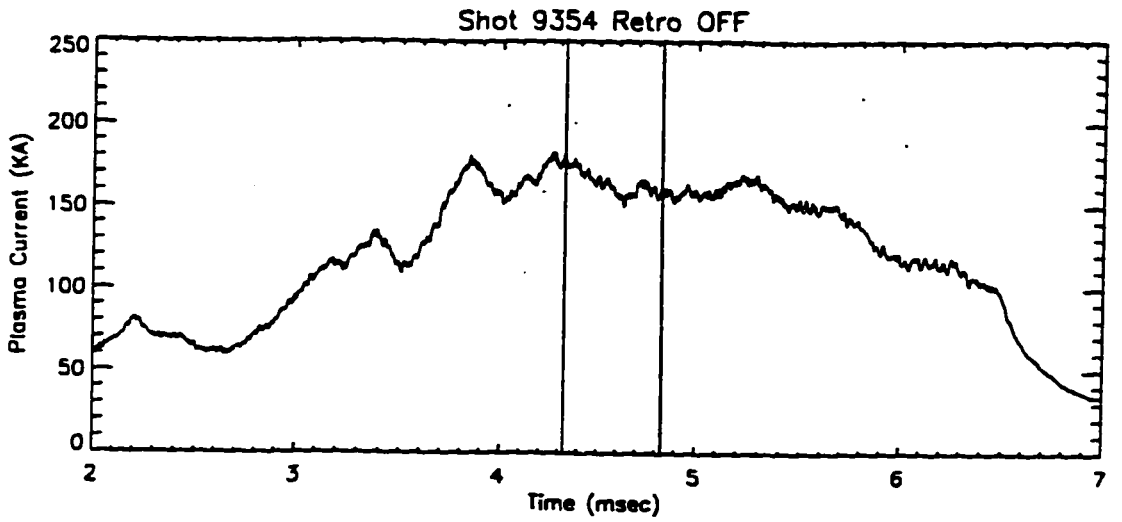


Figure 5.31 Plasma current versus time for shot 9354 for probe in plasma with no retro-reflecting sheet.

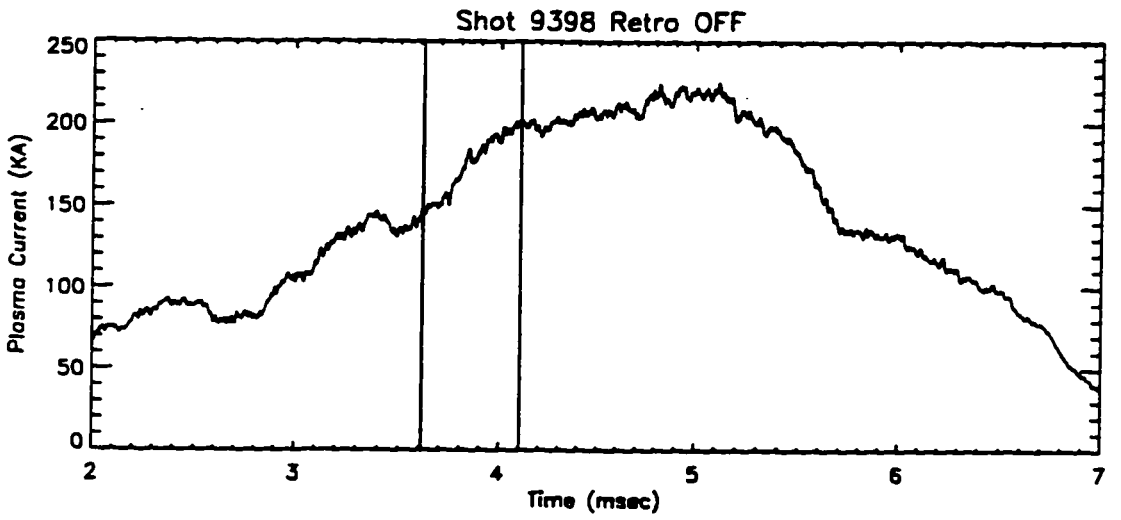


Figure 5.32 Plasma current versus time for shot 9398 for probe in plasma with no retro-reflecting sheet.

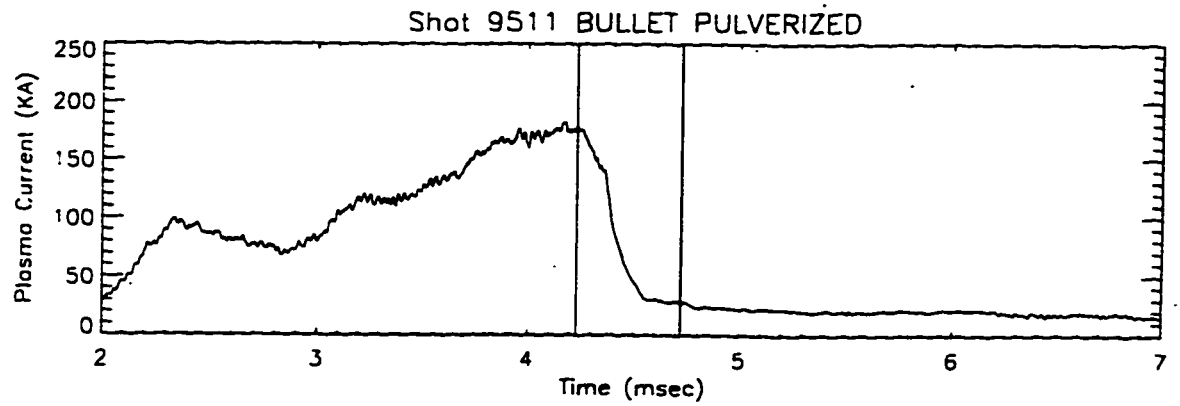


**Figure 5.33 Plasma current versus time for shot 9511 for probe that was pulverized prior to entrance in plasma due to a failure of the sabot stripping system.**

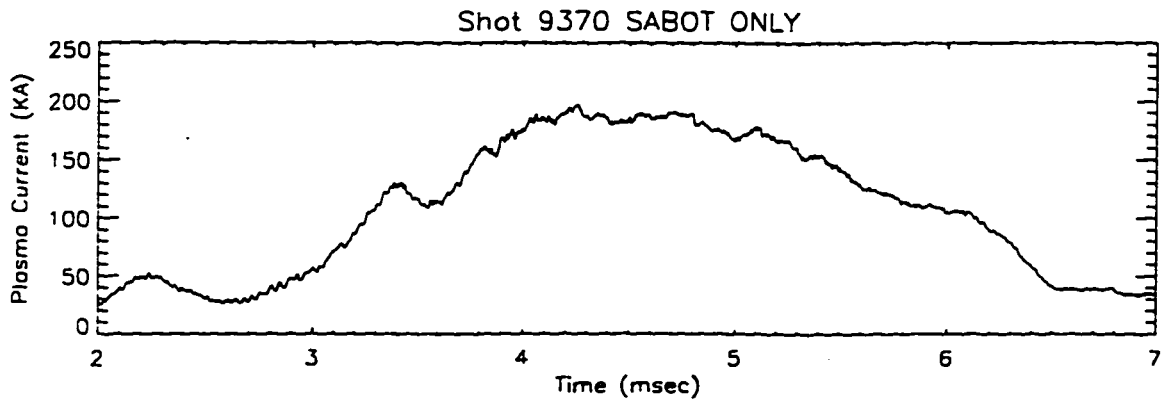


**Figure 5.34 Plasma current versus time for shot 9370 in which only a sabot was launched with no probe.**

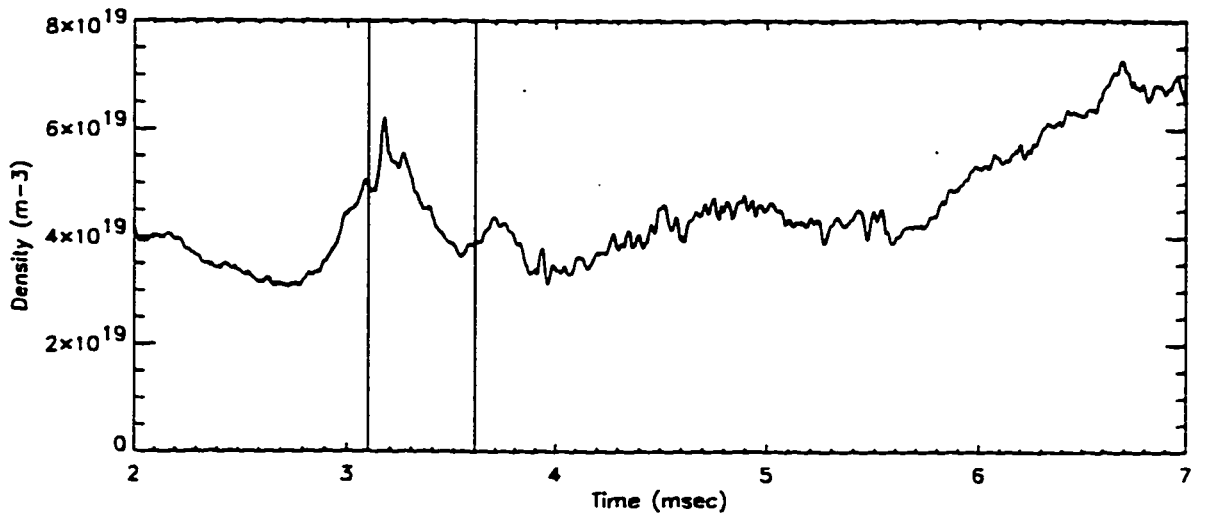


Figure 5.35a Plasma density versus time for 1st plasma shot (shot 9231).

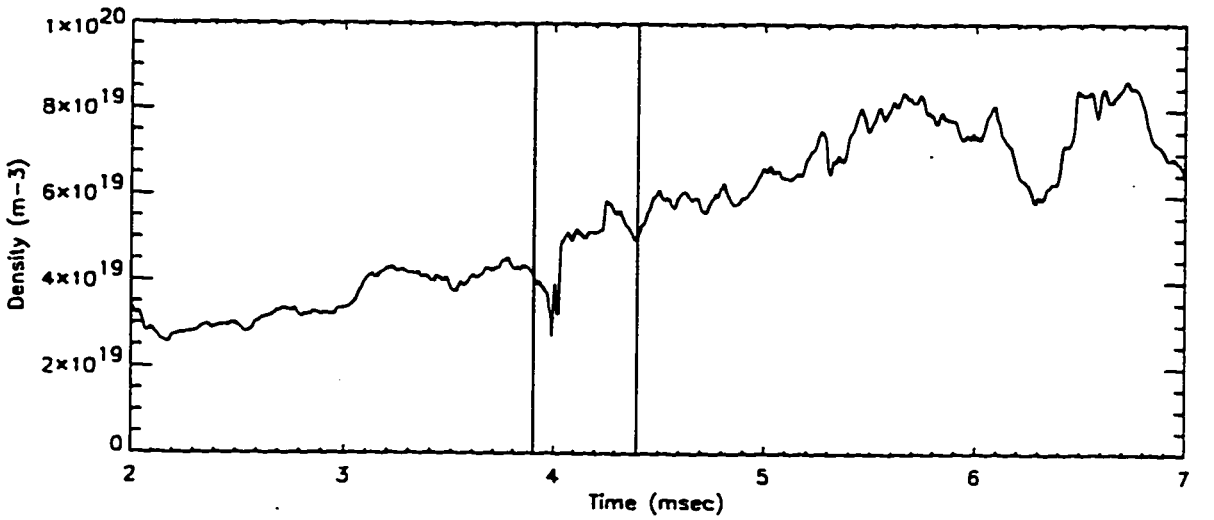


Figure 5.35b Plasma density versus time for shot 9403.

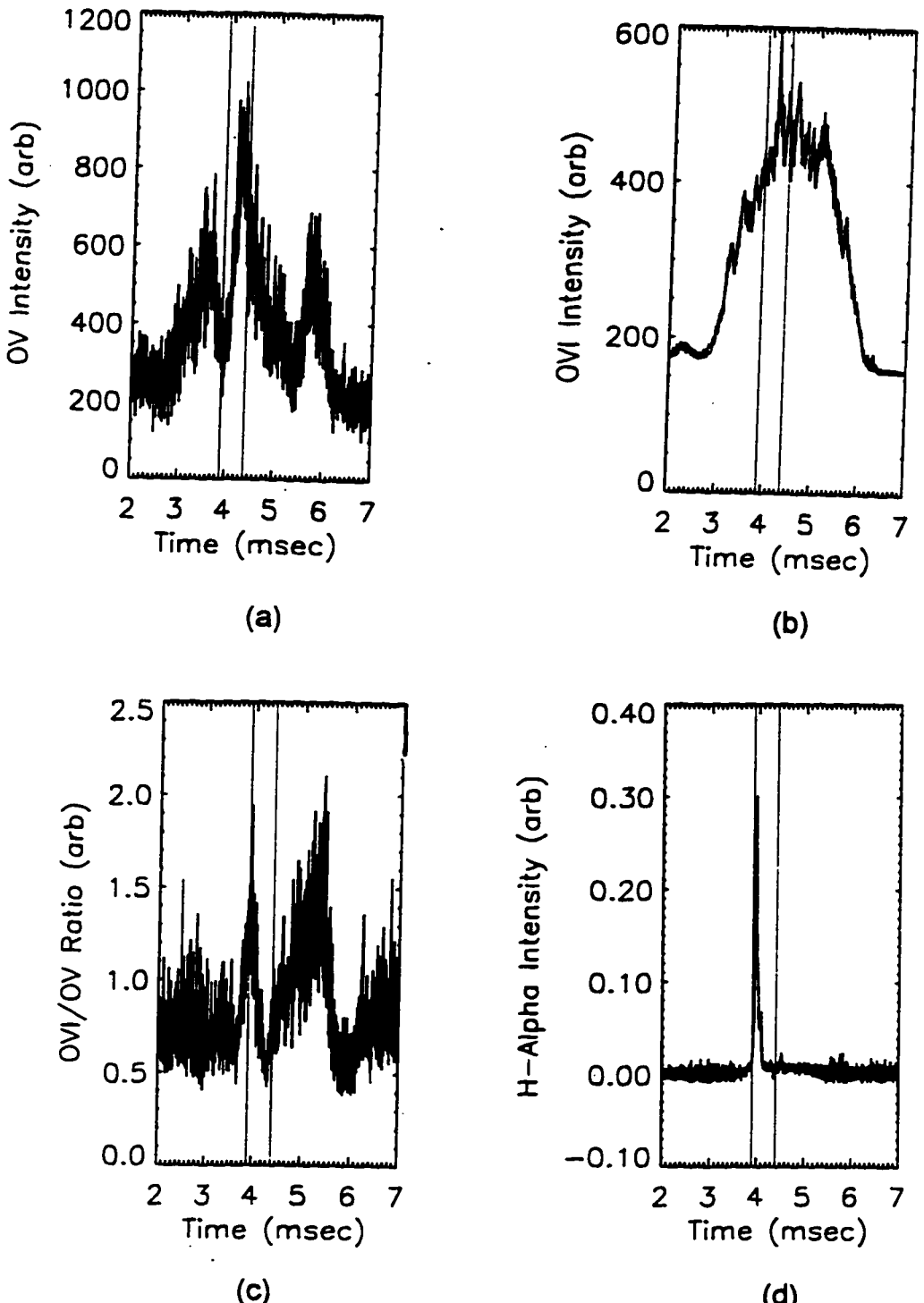


Figure 5.36 (a) OV VUV spectroscopy data, (b)OVI VUV spectroscopy data (c)OVI/OV ratio, (d)and H-alpha data versus time for probe in plasma with retro-reflecting sheet.

## 6. Future Research and Development

### 6.1 Future Probe Research and Development

The TIP diagnostic has demonstrated the ability to make high speed magnetic field measurements in a plasma. But more research and development is required in order to realize the full potential of the diagnostic concept. This development can be broadly categorized into probe improvements targeting enhanced thermal and optical performance, and system improvements targeting automation and reliability.

Three areas of improvement exist for the faraday rotator probes. The first area is elimination of the corner cube reflector sheet. The sheet has proven functional, but the non-ideal behavior of the corner cubes makes high resolution polarimetry extremely difficult. The retro sheet could be replaced by installing a lens on the front of the probe and silvering the rear surface of the probe. By using a flat mirror reflector, the polarization of the incident light would be preserved for all orientations. Additionally, acceleration would not damage the optical performance. A metallic reflective surface would also be less temperature sensitive.

The second area of future probe development involves thermally protecting the probe with diamond. Presently, unclad faraday probes are limited to probing plasmas with temperatures less than 100 eV . Probing 1 keV plasmas requires a 1 mm thick diamond coat. This could be done either through "potting" the probes in prepared diamond boxes or using chemical vapor deposition techniques to coat the probes. Once suitably protected probes are obtained, research is required to accurately test and model the ablation behavior, along with observing the optical performance of the probe during heating and ablation.

Finally, the current probe design only measures the component of the magnetic field in the direction of the probe flight path. A probe that could measure the field perpendicular to the flight path would be much more effective. Using a probe of this type, a probe launched in the toroidal direction could perform a scan of the poloidal field directly. In this case, an accuracy of a few percent would be more than sufficient to determine the current profile. Ideally the transverse probe concept could be extended to simultaneously measure more than one component of the field making the probe valuable for any plasma geometry.

### 6.2 Future Diagnostic System Development

Four upgrades are needed for improved performance and compatibility with laboratory plasma experiments. First, development of a new gas gun is required in order to reach the desired velocity of 5 km/s. A longer, less peaked pressure pulse is necessary to achieve the higher velocities and is also more desirable because it places less stress on the probe during acceleration. More research is required to better understand the sabot stripping process. Scaling laws are necessary to properly predict the number of venting holes required to separate the probe and sabot thus eliminating unnecessary holes which cause instabilities in flight. Additionally, research should be conducted to investigate the potential for using the sabot to crush a constricting baffle to seal muzzle gases from proceeding downrange. This would allow elimination of the expansion tank and fast valve, which would significantly reduce the overall size of the diagnostic and reduce cycle time between shots.

The gas handling and diagnostic control system needs to be fully integrated into one remotely operated system. During the development process, each system was built to operate independently. Present operation requires significant manual operation with considerable potential for equipment damage in the event of operator error. A comprehensive control system with appropriate

interlocks coupling the vacuum systems, optical detection system, and fire control system is needed to improve reliability and make the diagnostic amenable to varied plasma experiments.

Finally, further research is necessary to improve the optical detection system and eliminate the systematic errors degrading the accuracy of the diagnostic. An ellipsometer developed after this report was begun removes the linear light assumptions of the optical detection system discussed in this report. But more work is required to determine the cause of the subtle drift in the baseline polarization angle measurement.

Incorporating these improvements would result in an extremely powerful new diagnostic for measuring internal magnetic field profiles and fluctuations. With this diagnostic, previously undiagnosed internal profiles of magnetically confined plasmas with temperatures up to a keV and any geometry could be investigated.

## 7. References


[1]J.Ferron, L. Lao, T. Taylor, Y. Kim, E. Strait, D. Wroblewski, *Physics of Fluids B*, **5**, 2532 (1993).

[2]C. Kessel, J. Manickam, G. Rewoldt, W. Tang, *Physical Review Letters*, **72**, 1212 (1994).

[3]F. Levinton, M. Zarnstrorff, S. Batha, M. Bell; R. Budny, C. Bush, Z. Chang, E. Fredrickson, A. Janos, J. Manickam, A. Ramsey, S. Sabbagh, G. Schmidt, E. Synakowski, G. Taylor, *Physical Review Letters*, 75, 4417 (1995).

[4]F. Levington, G. Gammel, R. Kaita, H Kugel, D. Roberts, *Review of Scientific Instruments*, **61**, 2914 (1990).

[5]D. Wroblewski, K. Burrell, L. Lao, P. Politzer, W. West, *Review of Scientific Instruments*, **61**, 3552 (1990).

[6]V. Simcic, K. Connor, T. Crowley, R. Hickok, A. Wooten, X Yang, Y. Yang, *Review of Scientific Instruments*, **61**, 3061 (1990).

[7]H. Soltwitch, H. Koslowski, *Plasma Physics and Controlled Fusion*, **37**, 667 (1995).

[8]B. Rice, E. Hooper, *Nuclear Fusion*, **34**, 1 (1994).

[9]J. Terry, E. Marmar, J. Snipes, D. Garner, V. Sergeev, *Review of Scientific Instruments*, **63**, 5191 (1992).

[10]J. Terry, E. Marmar, R. Howell, M. Bell, A. Cavallo, E. Fredrickson, A. Ramsey, G. Schmidt, B. Stratten, G. Taylor, M. Manual, *Review of Scientific Instruments*, **61**, 2908 (1990).

[11]W. West, J. McChesney, M. Thomas, X. Zang, *Review of Scientific Instruments*, **61**, 2929 (1990).

[12]J. Galambos, M. Bohnet, T. Jarboe, A. Mattick, *Review of Scientific Instruments*, Acepted for publication in Jan 1997.

[13]J. Galambos, M. Bohnet, T. Jarboe, A. Mattick, *Review of Scientific Instruments*, **67**,469 (1996).

[14]M. Bohnet, J. Galambos, T. Jarboe, A. Mattick, *Review of Scientific Instruments*, **66**, 1197 (1995).

[15]G. Spanjers, J. Galambos, M. Bohnet, T. Jarboe, W. Christiansen, G. Wurden, B. Wright, R. Smith, *Review of Scientific Instruments, 63, 5148 (1992).*

[16]M. Bohnet, J. Galambos, T. Jarboe, A. Mattick, 1995 IEEE International Conference on Plasma. June 5-8, Madison, Wiscconsin.

[17]B. Nelson, T. Jarboe, D. Orvis, L. McCullogh, J. Xie, C. Zhang, L. Zhou, *Physical Review Letters*, **72**, 3666 (1994).

[18]R. Lovberg, *Plasma Diagnostic Techniques*, edited by R. Huddlestone and S. Leonard, 1965.

[19]I. Hutchinson, *Principles of Plasma Diagnostics,* 1987.

[20]P. Stangeby, Physics of Plasma Wall Interactions, Edited by D. Post and R. Berisch, 1984.

[21]K. Shirashi, S. Takamura, Contributions to Plasma Physics, **32**, 243 (1992).

[22]L. Schwager, Physics of Fluids B, **5**, 631 (1993).

[23]Franklin, W. Han, Plasma Physics and Controlled Fusion, **30**, 771 (1988).

[24]Pedgley, G. McCracken, Plasma Physics and Controlled Fusion, **35**, 397 (1993).

[25]Woods, B. Hopkins, G. Matthews, G. McCracken, P. Sewell, H. Fahrang, Journal of Applied Science, 5-8 June, Madison WI.

[26]R. Langley, J. Bohansky, W. Eckstein, P. Mioduszewski, J. Roth, E. Taglauer, E. Thomas, H. Verbeek, K. Wilson, "Data Compendium for Plasma Surface Interactions," *Special Issue of Nuclear Fusion*, (1984).

[27]L. Swager, W. Hsu, D. Tung, Physics of Fluids B, **5**, 621 (1993).

[28]B. Kuteev, V. Sergeev, L. Tsendin, *Soviet Journal of Plasma Physics*, **10**(6), 675 (1984).Physics, **20**, 1136 (1987).

[29]J.G. Laframboise, UTIAS Report, June 1966, No. 100.

[30]L. Thomas, *Heat Transfer*, 1993.

[31]P. Parks, J. Leffler, R. Fisher, *Nuclear Fusion*, **28**, 477 (1988).

[32]T. Kawamura, T. Ono, Y. Yamamura, *Journal of Nuclear Materials*, **220-222**,1010 (1995).

[33]J.Huba, *NRL Formulary*, Revised 1994 (Naval Research Laboratory Washington, D. C. 1994).

[34]M. Bohnet, "Design of a Two Stage Light Gas Gun for the Transient Internal Probe Diagnostic," Masters Thesis, University of Washington, Aug 1993.

[35]J. Galambos, "Remote Magnetic Field Measurements Using an Optically Coupled Moving Probe," Masters Thesis, University of Washington, Jan 1993.

[36]J. Taylor, *Reviews of Modern Physics*, 58 741 (1986).

## Appendix A Probe Assembly

### A.1 Probe Fabrication

The fabrication process for the probes consists of three processes. First, the base Faraday glass material must be cut and ground to the desired specifications. In parallel, the Lexan sabots must be cut. Finally, the retro-sheet is attached to the probe, and the probe is installed in the sabot for firing in the gun. If necessary, the probe is calibrated prior to placement in the sabot.

Cutting and grinding of the probes has been done both by hand and contracted out to Veeco Custom Optics Co. in Santa Clara, California. Contracting out is much preferred. The specifications for cutting of the material are shown in figure A.1. The overall size of the probes is somewhat arbitrary and likely could be reduced to 3 mm x 3 mm. As mentioned in chapter three, the length determines the magnetic field resolution of the probe and inversely the spatial resolution of the probe. 1 centimeter is a good compromise. As specified in the drawing, the faces of the probe should be beveled. This reduces stress in the material and aids the application of the retro-reflector sheet. Polish quality and dimensional tolerances are also shown in figure A.1. The most significant tolerance is the angle between the base face and the side walls. Unfortunately, this is also the most difficult dimension to grind. Most optical applications are concerned with parallelism between faces and not perpendicularity. Typically, upon receipt of the probes, the face closest to perpendicular is chosen as the base. Standard cutting time for the probes is two weeks, although rush orders in less than a week are possible.

While probes are being cut, the protective sabots should be made according to the drawing shown in figure A.2. The material used most successfully is polycarbonate known by the trade name LEXAN. Many gas gun

applications use ULTEM which is a stronger material with a higher melting temperature than LEXAN. ULTEM was tested and rejected as being too brittle and difficult to machine to justify the modest performance improvements. But, higher velocity TIP shots may show UTLEM to be a better material. Traditionally the sabots have been cut by the local professional instrument makers, but strong consideration should be given to contracting production to an outside CNC machining source, provided the specified tolerances can be maintained. Particular emphasis should be placed on ensuring the hole is concentric with the outer diameter. Assuming a minimum order of 12, a professional instrument maker can produce the sabots at a rate of 3/ hour.

Once the sabots and probe materials have been cut, assembly of the probe can take place in a relatively short time period. (~1hr/probe) The first step is grinding the probe to fit the sabot. This should be done while wearing powder free examination gloves to minimize oil residue on the probe. 600 grit sandpaper is the preferred grinding surface. Using long slow strokes, the long edges of the probe should be ground so that the cross dimensions of the probe face is slightly greater than the hole diameter. The fit should be tight, such that the probe requires significant force to "snap" into the sabot. Tolerance between the diagonal dimensions is less than 0.0005". This is achieved by grinding slowly and measuring each diagonal dimension on both ends of the probe following each grinding stroke. Figure A.3 shows the probe before and after grinding.

Once the probe is ground the retro-reflector sheet should be installed. The sheet should be cut into a square fitting slightly greater than the probe face. The retro-sheet is then glued to the back of the probe using relatively fresh (less than two week old) Elmer's Superglue®. Once the glue has dried the back edges of the retro-sheet are ground flush with the probe sides and the four corners are ground back to insure they do not interfere with the sabot. If desired, a 2-4 mill stainless steel back plate can be applied in the same manner

as the retro sheet, except that it should be clipped at the corners to insure no interference with the sabot occurs. The probe is then pressed into the sabot and is ready for shooting. If necessary, the probe can be removed without damage from the sabot by applying a small amount of Acetone. The Acetone causes severe cracking in the stress points of the sabot allowing easy extraction of the probe. Note: removal of the paper backing from the retro-sheet prior to application of the stainless steel back plate is desired, but extreme care must be observed to avoid damaging the corner cube surface. Shots with and without the paper have been conducted with varying degrees of success. On some occasions the metal backing pulled away from the probe along with the paper backing. Data was still obtained, but no protection of the retro-sheet in the plasma is achieved. Note: The probe and sabot design discussed above is for the standard direct fitting axial probe.

Another concept has been investigated with some success to deal with more complex optics. The concept involves potting the optical components in an epoxy plug which is then either coated or surrounded with a refractory material. Figure A.4 shows the sabot design. Essentially it is the same as figure A.2 except with a larger hole. A complex glass probe potted in ULTEM was flight tested successfully, but significant work is still required to find an appropriate potting epoxy and design to fly complex optical configurations.

## A.2 Determination Of Probe Verdet Constant

In some cases, the verdet coefficient of the material used to fabricate the probes is not well known. Determination of the verdet coefficient is then necessary. The procedure for making this determination is quite straight forward. Probes are simply placed in a known magnetic field and the amount of Faraday rotation is measured using a polarimeter. The key to the procedure is having a known magnetic field of sufficient spatial homogeneity and strength to

accurately determine the verdet coefficient properly. Magnetic Resonance Imaging (MRI) magnets provide the ideal test field and were used for the experimental verification. An MRI coil set was chosen that had a 4 inch homogeneous axial field measuring 2.00956 +/- 0.00001 tesla. The polarimeter was calibrated using the procedure described in Appendix B. Once calibration was complete, measurements of the faraday rotation for each probe were conducted. Shown below are the results of the measurements for the Kigre and Hoya materials.

| Material | Rotation | Verdet (deg/cm g) |
|---|---|---|
| Kigre M-32 | $380.3^0$ +/- 0.3 | 0.00946 +/- 0.00001 |
| Hoya FR-5 | $287.8^0$ +/- 0.3 | 0.716 +/- 0.00001 |

All Dimensions +/- 0.001"
Angular tolerance +/- 0.5 °
Polish to 1/4 λ.

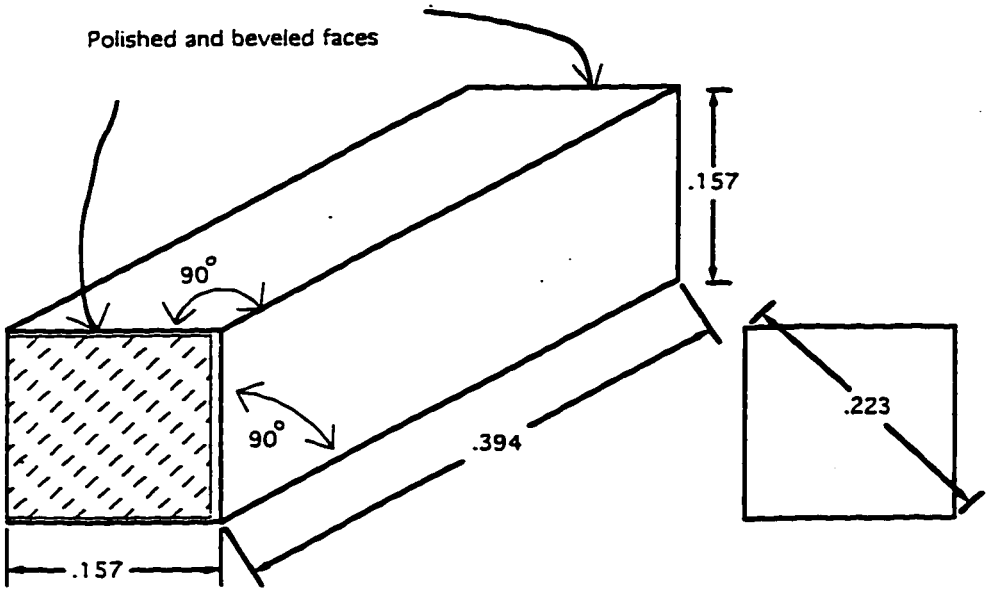


Figure A.1 Schematic of faraday glass probe

Standard Sabot

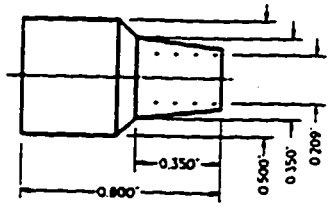


Tolerances

| | | |
|---|---|---|
| Diameters | +/- | 0.0005" |
| Lengths | +/- | 0.005" |
| Angles | +/- | 5 degrees |

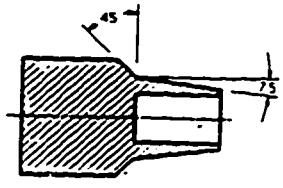


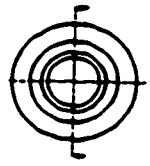

Figure A.2 Schematic of Lexan Sabot.

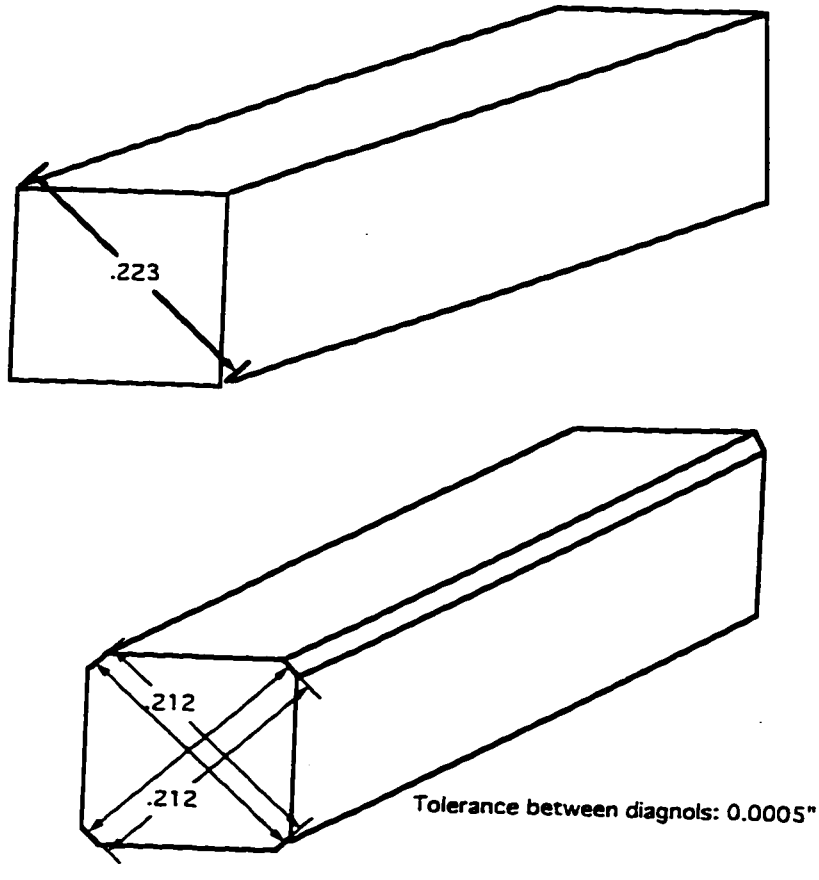


Note: Dimensions shown are an example
and should be ground specific to the sabot

Figure A.3 Schematic of faraday rotator probe after grinding.

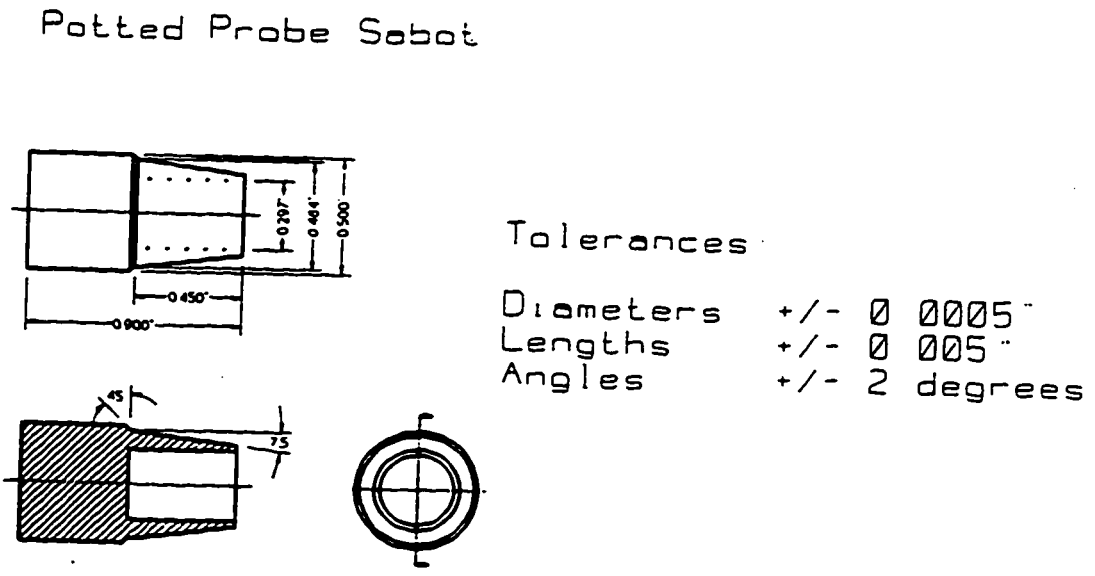


Figure A.4. Schematic of potted Lexan sabot.

## Appendix B Optical Detection System Alignment and Calibration

### B.1 Alignment Procedures

Two procedures are required to align the ODS for calibration and diagnostic operation. The first procedure involves imaging the individual detectors such that they act as one detector and variations in light intensity are observed equally by all three detectors. The second procedure involves aligning the illumination laser with the probe flight path. Figure B.1 shows the overall diagnostic alignment components and figure B.2 shows the pertinent components of the optical detection system used for alignment.

**Precautions:**

Wear safety glasses at all times when operating illumination laser.
Control access to room while operating illumination laser.

#### B.1.1 Initial Optical Detection System Alignment

The first step in the process involves proper initial positioning of the steering mirrors and illumination laser. These will be fine adjusted after the initial ODS alignment procedure is complete.

1. Establish HeNe alignment beam concentric with gas gun barrel per appendix D and position ODS system as shown in figure B.1.
2. Adjust illuminating laser beam expander to provide circular ~1cm diameter beam 8-10 meters down range.
3. Filter the laser to reduce power to an acceptable detector output level.
4. Install a mirror (or corner cube) to retro-reflect the laser back to the ODS.

5. Adjust optical tables and mounts so that illumination laser does the following:

- Intersects steering mirrors #1 and #2 essentially in the center.
- Intersects the first beam splitter in line with detector 2 and the center of the collecting lens.
- Remains essentially horizontal.

6. Adjust the height of the collecting lens and detector 2 so that the reflected beam passes through the center of the lens and is focused on the center of detector 2.
7. Measure distance from the collecting lens to detector 2 and position detectors 1,3 the same distance away.
8. Using detector output voltages, center detectors 1,3 on the reflected beam. Adjust beam splitter angles as necessary.

Enough adjustment should remain to use the two steering mirrors near the catch tank to make the illumination laser and HeNe alignment lasers coincident. At this point rough alignment is complete and the table adjusts and optical mounts should be firmly secured along with the beam expander and steering mirror #1. Fine positioning of the ODS proceeds as follows:

9. Use steering mirror #2 to shine the illumination laser on a white background 3-5 meters away. Mark this position with a heavy black dot.
10. De-energize the laser and darken the room completely.
11. Use mounted flashlights to individually back light the detectors to form an image on the screen. Adjust position (NOTE: This likely will require considerable finesse).
12. Carefully adjust detector position and angles such that all three images overlay.

13. Secure detector mounts and replace ODS cover.

### B.1.2 Alignment Of Illumination Beam With Flight Path

This procedure is required prior to each shot due to the destruction of the breakable mirror. Because of the highly critical nature of this alignment, it should be conducted as near to time of fire as possible.

**Initial Conditions**

- HeNe laser aligned with barrel and probe NOT installed.
- High Vacuum established in both catch tank and expansion tank.
- Illumination laser warmed up and operating at desired power.

**Procedure**

1. Verify proper vacuum and open isolation valves to allow HeNe beam to reach ODS.
2. Use steering mirrors #1 and #2 to roughly make HeNe and illuminating laser coincident.
3. Observe beam overlap at barrel breech and fine adjust illumination laser using mirrors #1 and #2 to make beams coincident.
4. Double check beam overlap at laser source and breech of barrel.
5. Install probe and verify detector voltages are reading properly.

## B.2 Calibration Procedure And Codes

As discussed in section 3.4.2 calibration of the optical detection system is critical to accurate measurement of the magnetic field. The procedure involves

inputting light of known polarization states into the detection system by using a half-wave plate and recording the functional response of the detection system.

### B.2.1 Calibration Procedure

1. Install the half-wave plate as shown in figure B.3.
2. Suspend a faraday probe with retro-sheet in the illumination beam in region of negligible magnetic field surrounded by a black background.
3. Adjust laser power to the desired level, such that detector voltages do not exceed ~750 mV at any input polarization.
4. Prepare digitizers to take ninety one 1 K segments at 1MHz.
5. Carefully rotate half-wave plate in 2 degree increments through 180 degrees (Note this will rotate polarization $360^{o}$).
6. Once all rotations are complete block the laser beam at the catch tank and record detector offset voltages.
7. Record data at each increment.
8. Run program JPOLAR.PRO.
9. Remove half-wave plate and suspended probe.

## B.2.2 Calibration Code JPOLAR.PRO

```
pro Jpolar -
   MDS
   shot=GET_SHOT(shot)
   shot=SET_SHOT(shot)
;
;  The data is read in from 50 segments.  Each polarization angle is
;  sampled for 1 msec at 1MHz.  The first 49 are for each input angle
;  beginning at -8 to 188 degrees in 4 degree intervals. 50 is the offset
;
   npts=49
   npol1=fltarr(1024)
   npol2=npol1
   npol3=npol2
   anpol1=fltarr(49)
   anpol2=anpol1
   anpol3=anpol2
   NINE=9
   off1=DATA('DET1_0050')
   off2=DATA('DET2_0050')
   off3=DATA('DET3_0050')
   off1=SMOOTH(off1,13)
   off2=SMOOTH(off2,13)
   off3=SMOOTH(off3,13)

;  Normalize and then average data points

   for i=0,npts-1 do begin
     if i le 8 then $
          bogus1=data('DET1_000' + strcompress(string(i+1),/remove_all)) $
      else $
          bogus1=data('DET1_00' + strcompress(string(i+1),/remove_all))
      if i le 8 then $
          bogus2=data('DET2_000' + strcompress(string(i+1),/remove_all)) $
      else $
          bogus2=data('DET2_00' + strcompress(string(i+1),/remove_all))
      if i le 8 then $
          bogus3=data('DET3_000' + strcompress(string(i+1),/remove_all)) $
      else $
          bogus3=data('DET3_00' + strcompress(string(i+1),/remove_all))
        bogus1=SMOOTH(bogus1,13)
        bogus2=SMOOTH(bogus2,13)
        bogus3=SMOOTH(bogus3,13)

;       This subtracts smoothed offset from smoothed bogus

        bogus1=bogus1-off1
        bogus2=bogus2-off2
        bogus3=bogus3-off3
        sum=bogus1+bogus2+bogus3
        npol1=bogus1/sum
        npol2=bogus2/sum
        npol3=bogus3/sum

;
;       Average normalized data
;
        anpol1(i)=total(npol1)/1024
        anpol2(i)=total(npol2)/1024
        anpol3(i)=total(npol3)/1024
endfor
```

```
;
;  Each detector data set of 49 pts is fit with a 9th order polynomial

   theta=findgen(npts)*4-8

;  FIT POLYNOMIALS
   c1=poly_fit(theta,anpol1,8)
   c2=poly_fit(theta,anpol2,8)
   c3=poly_fit(theta,anpol3,8)
   anpol=[anpol1,anpol2,anpol3]
   plot,theta,anpol1,psym=1,yrange=[min(anpol),max(anpol)],xtitle='Degrees'
   oplot,theta,poly(theta,c1),co=2
   oplot,theta,anpol2,psym=1
   oplot,theta,poly(theta,c2),co=3
   oplot,theta,anpol3,psym=1
   oplot,theta,poly(theta,c3),co=4

;  The polynomial coeficients are stored in file "Coef.lis" for use in the
;  program "Mag.pro" which analyzes the data.

   openw,3,'COEF.dat'
  PRINTF,3,NINE
  PRINTF,3,C1
  PRINTF,3,NINE
  PRINTF,3,C2
  PRINTF,3,NINE
  PRINTF,3,C3
        close,3
        end
```

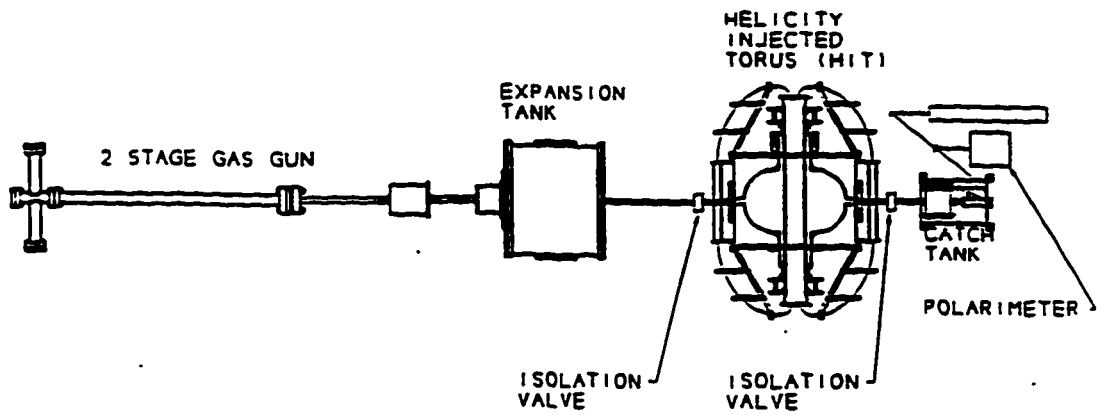


Figure B.1. Schematic of overall arrangement for alignment of the TIP diagnostic.

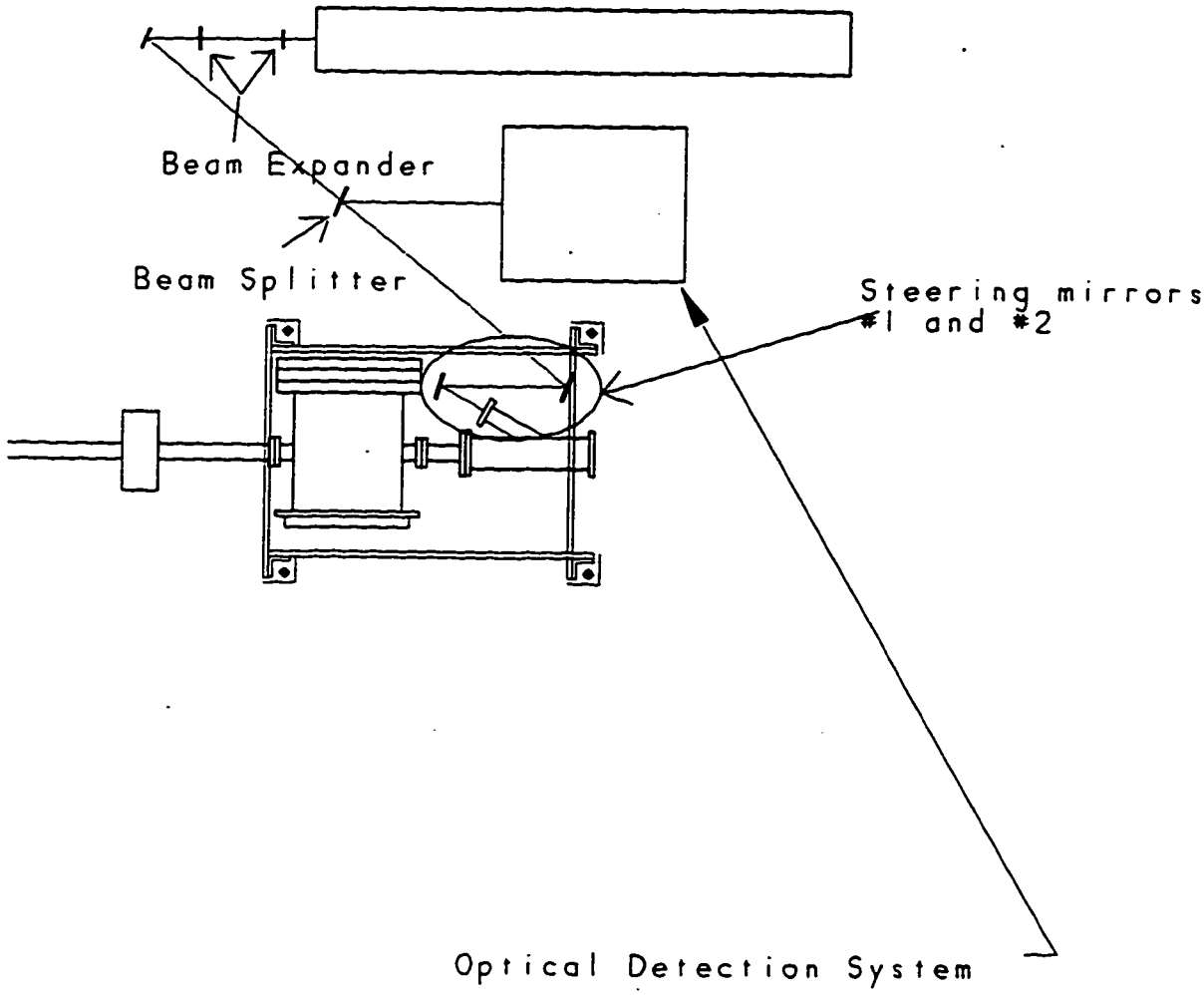


Figure B.2. Optical alignment components.

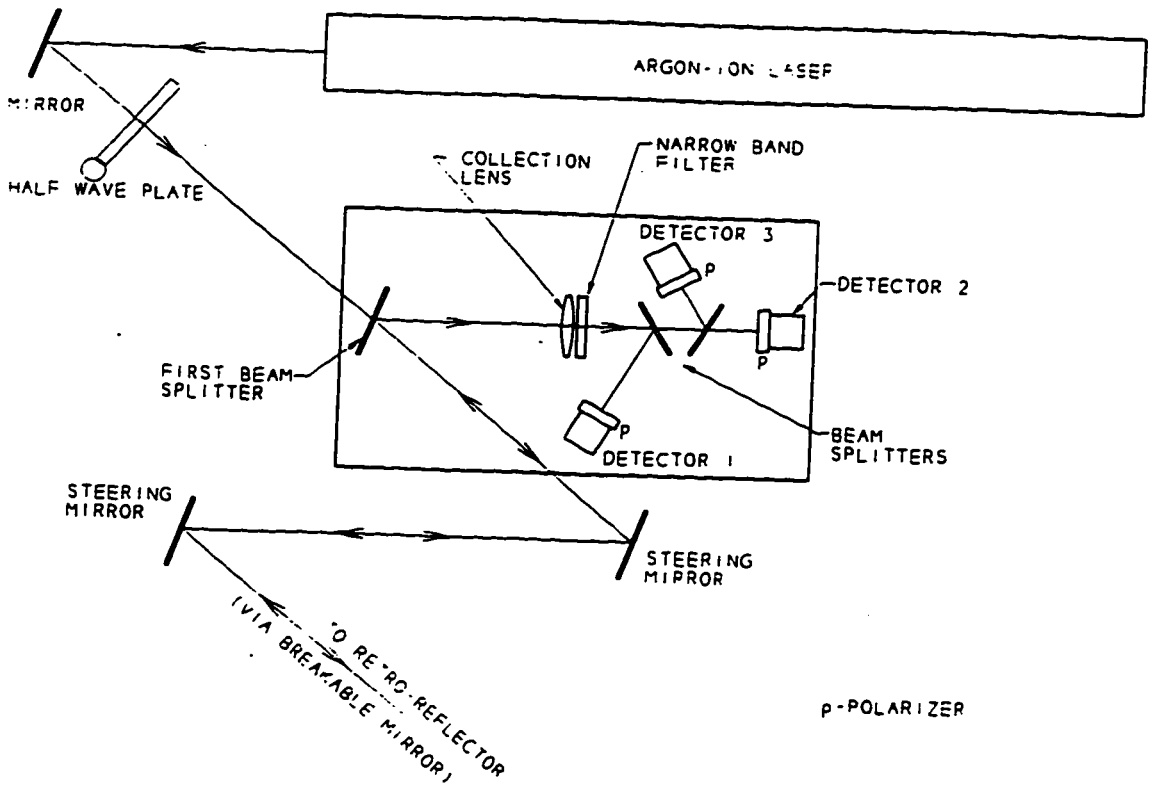


Figure B.3 Layout for calibration of optical detection system.

## Appendix C Diagnostic Operation

This procedure and checklist are written for operation of the diagnostic to make field measurements in the tokamak. For other operating conditions the procedures and list should be reviewed and modified prior to firing.

### C.1 TIP Pre-fire Checklist

Completion of this checklist prepares the diagnostic for pump down and firing operation. Cleaning and equipment preparation requires approximately 2 man-hours. Pump down requires 3-4 hours.

| **Miscellaneous** | |
|---|---|
| Insure probe/sabot on hand (appendix B) | |
| Insure cut diaphragm on hand (appendix D) | |
| Insure o-rings on hand | |
| Insure breakable mirror on hand | |
| Obtain liquid nitrogen | |
| | |
| **Gun System (Appendix D)** | |
| Pump Tube cleaned | |
| Barrel cleaned | |
| Piston cleaned | |
| | |
| **Expansion Tank System** | |
| Expansion tank vacuumed | |
| Expansion tank cold trap rinsed and re-installed | |
| Flapper valve removed and cleaned | |
| | |
| **Catch Tank System** | |
| Catch tank cleaned | |
| Breakable mirror holder removed and cleaned | |
| Catch tank view port window cleaned | |
| Catch tank system o-ring seals cleaned and greased | |
| Catch tank cold trap alcohol rinsed and reinstalled | |
| | |

**NOTE:** Insure laser alignment beam is concentric with barrel prior to continuing checklist.

| **Gun System (Appendix D)** | |
|---|---|
| Piston o-rings replaced | |
| Bridgeman seal replaced | |
| Piston assembled | |
| Piston stop assembled with three o-rings | |
| Muzzle insert cleaned | |
| Probe/sabot assembled | |
| Cut ss diaphragm on hand | |
| | |
| **Expansion Tank System** | |
| Install mylar diaphragm | |
| Install hand ports | |
| Set and install flapper valve | |
| Install baffles if removed | |
| Insure turbo pump guard in place | |
| Check shut vent valve | |
| Check open ion gauge valve | |
| Energize turbo cooling water | |
| Start cooling water to turbo pump | |
| Check shut turbo vent valves | |
| Shut ER-1 | |
| Shut RC-1 | |
| Check shut RT-1 | |
| Check shut ET-1 | |
| Check all window ports are installed | |
| Close and bolt access hatch | |
| | |
| **Catch System** | |
| Install window port if removed | |
| Install view port baffles | |
| Install breakable mirror | |
| Install probe deflector plate catch tube | |
| Check shut turbo vent valve | |
| Shut CR-1 | |
| Shut RC-2 | |
| Check shut RT-2 | |
| Check shut CT-1 | |

## Shutdown Checklist

| | |
|---|---|
| Dump valve open | |
| Turbo pumps secured | |
| Rough pumps secured | |
| Expansion tank ventilated and open | |
| Camera, strobe, and amplifier secured | |
| Lasers (4) secured | |
| Laser trigger amps secured | |
| Stepper motor secured | |
| Gas lines shut and vented | |

## C.2 TIP on HIT Pump Down Procedure

**Initial Conditions:**

- TIP Pre-fire checklist complete.
- HIT tank pumped down to base pressure.
- HIT isolation valves, H-1 and H-2 SHUT.
- Interlock bypass removed.

**Roughing Cycle:** This portion of the procedure isolates the vacuum system and pumps both the expansion tank and catch tank to less than 50 mtorr so they are ready for turbo pump operation.

Expansion Tank System

1. Install liquid nitrogen.
2. Start rough pump.
3. OPEN ER-1.
4. Slowly OPEN RC-1.
5. Verify proper pump operation by observing E-PS-1.
6. Interlock should prevent opening ET-1 while ER-1 is open.
7. Pump to 25-50 mtorr.

Catch System:

1. Check shut vents.
2. Install liquid nitrogen.
3. Start Roughing pump.
4. OPEN RC-2.
5. OPEN CR-1.

6. Interlock should prevent opening CT-1 while CR-1 is open.
7. Verify proper operation by observing C-PS-1.
8. Pump system down to 25 mtorr.

**Final Pump Down Cycle**:

Expansion System:

9. SHUT ER-1 and RC-1.
10. OPEN RT-1.
11. When E-PS-1 and E-PS-2 are less than 25 mtorr.
12. Start turbo pump and wait for normal operation light.
13. OPEN ET-1.
14. Interlock should shut ET-1 if E-PS-1 exceeds 100 mtorr.
23. Interlock should shut ET-1 and RT-1 if E-PS-2 exceeds 200 mtorr.

Catch System:

24. SHUT CR-1, RC-2.
25. OPEN RT-2.
26. When C-PS-1 and C-PS-2 are less than 25 mtorr.
27. Start turbo pump and wait for normal operation light.
28. OPEN CT-1.
29. Interlock should shut CT-1 if C-PS-1 exceeds 40 mtorr.
30. Interlock should shut CT-1 and RT-2 if C-PS-2 exceeds 200 mtorr.

During pump down, the following miscellaneous checklist should be completed: (Tokamak operation and conditioning should also begin during pump down)

| **Miscellaneous** | |
|---|---|
| Bring computer system online and take practice shot. | |
| Set stepper motor to proper position. | |
| Warm up illumination laser. | |
| Energize ODS and verify voltages. | |
| Take offset data shot. | |
| Align speed triggers. | |
| Test speed triggers. | |
| Check trigger delay times. | |
| Insure film in camera. | |
| Warm up camera and strobe( if necessary). | |
| Take test picture. | |
| Open and shut gas supply valves and record tank pressures. | |
| | |

## C.3 TIP Firing Procedure

**Final Alignment:** This procedure requires intermittent opening and closing of H1 and H-2 to align the illuminating laser with HeNe laser. This will require approximately 10 minutes, during which the systems (TIP and HIT) will be connected.

When both catch system and expansion system are less than 3 micro-torr:

1 OPEN H-1 and H-2.
2 Align illumination laser with HeNe laser.
3 Block laser and take offset data shot.
4 Install probe in breech of barrel.
5 Observe detector output voltages.
6 Shut H-1 and H-2.
7 Install steel diaphragm in barrel.
8 Close gun (this takes 10 minutes) per appendix D.1.1.
9 Evacuate auxiliary tank per appendix D.1.2.
10 Fill auxiliary tank with nitrogen to appropriate pressure (32 psi).

**Firing Procedure**: During this section the gun is made ready to fire and control is turned over to HIT system. This procedure occurs during the 3 minute tokamak charge cycle. The actual firing sequence opening and shutting isolation valves should take less than 15 seconds.

1. Pump down gun per appendix D.1.3.
2. Coincident with start of HIT charging cycle fill gun to firing pressures D.1.4.
3. At T-30 seconds enable firing valve.
4. At T-15 seconds SHUT ET-1,CT-1.
5. At T-5 seconds turn gun control over to HIT by opening H-1,2.

6. Tokamak control system fires gun
7. SHUT H-1,H-2 immediately upon hearing gun fire.

**Post Firing Procedure:**

Gun System:

47. De-energize gun pump and vent system to outside.
48. Isolate source tanks.
49. Turn vacuum enable switch and fire switch off and de-energize gun control.
50. Vent source tank supply lines.
51. De-energize power to firing valve motor.

Expansion System:

47. SHUT and remove gun coupler and bring exp. Tank to atmospheric pressure.
48. Start exhaust pump (shop vacuum).
49. OPEN V-1 valve and ventilate system for 15 minutes.
50. Remove hand ports.
51. Remove access flange.
52. Clean system.

Catch System:

47. SHUT RT-2.
48. De-energize and vent turbo pump.
49. De-energize rough pump.
50. OPEN vent valve.
51. SHUT CR-1.
52. De-energize speed trigger amplifier and laser.
53. Clean system.

## Appendix D Gas Gun Operating And Maintenance Procedures

### D.1 Gas Gun Operating Procedure

#### Precautions

The two stage gas gun is a highly energetic device and must be operated with extreme caution. Typical operating pressures inside the gun exceed 35,000 psi for low pressure operation and 55,000 psi under high pressure conditions. Typical projectile energy is on the order of 5 kJ. Improper operation of the gun poses severe risk of injury to personnel and damage to equipment. A diagram of the gun firing control system is provided in figure D.1. These systems should be understood and operational prior to gun operation.

The following precautions shall always be observed:

- At time of fire, no person shall have a direct line of sight view of the gas gun. A solid bulkhead, preferably concrete, should separate operators from the gun and target.

- A minimum of two people must be present to fire the gas gun. One person must be authorized by the principle investigator to oversee gun operation.

- The projectile impact location must have sufficient strength and bulk to absorb both the probe and sabot. A minimum of ¾" aluminum enclosed in a steel can is required. 1½" is preferred.

- All access doors to the gun and target area must be locked and interlocks installed once the fill procedure for the gun has begun.

#### Initial Conditions

Equipment Status

- All equipment cleaned according to appendix D.4
- Diagnostics in position and tested (i.e. front and/or back transducer, laser trigger, digitizers, camera, etc.).
- Alignment procedure completed per appendix D.5.

Valve Status

REFER TO FIGURE D.1

- V-1,V-2 OPEN.
- Line vent valves N-1,2,3 and He-1 OPEN.
- Tank source valves SHUT.
- F-1,F-2 VENT.
- G-1,2 OPEN.

D.1.1 Gas Gun Assembly

1. Secure alignment lasers.
2. Visually inspect tube to insure tube is clear of all cleaning equipment.
3. Install piston into pump tube, verifying proper o-ring orientation.
4. Install breech insert, insuring all three o-rings are present.
5. Bolt rear flange to pump tube using star pattern to insure even seal.
6. Install Probe/sabot into barrel by gently tapping with plastic mallet such that sabot rear surface is ~3/8" into the barrel.
7. Screw locking flange gently onto barrel such that no further motion is possible, then back screw off of barrel two turns.
8. Install pump tube insert insuring that both o-rings are in place.
9. Install pump tube diaphragm gripper.
10. Install diaphragm, insuring grooves face towards the pump tube.
11. Install barrel diaphragm gripper and insure o-ring is in place.

12. Carefully join pump tube to barrel by pushing forward on pump tube and squeezing diaphragm between gripper flanges.
    **Note:** The indexing pegs should join easily. Reposition pump tube if they do not.
13. Tighten grip on diaphragm by screwing large vernier flange onto pump tube. Use torque bars to firmly tighten without lifting pump tube off of its stand.

D.1.1 Auxiliary Tank Preparation

1. Attach mobile rough pump and pump down auxiliary tank to less than 3 psi.
2. Shut 3 way fill valve.
3. Open auxiliary tank source valve.
4. Slowly fill auxiliary tank to appropriate stripping pressure.
5. Shut 3 way fill valve and SHUT the auxiliary tank pressure gage isolation valve.

D.1.2 Gas Gun Pump Down Procedure

1. Shut valves V-1 and V-2.
2. Connect mobile rough pump to nipple located near the driver tube.
3. Shut valves P-1, P-2.
4. Check Open valves N-1, N-2, and N-3, and He-1.
5. Turn valves F-1 and F-2 to the *fill* position.
6. Open valves G-1 and G-2.
7. Energize the control box by pressing the *power* button located on the front panel of the control box (the *power* button will light up when power is on).
8. Insure the *emergency stop* button is completely pulled out.
9. Press the *secure* button located on the front panel of the control box so that the *secure* button is illuminated (If *secure* button does not remain illuminated

after it is pressed, then either one or both of the doors are ajar or the emergency stop button is pressed in).

10. Start vacuum pump.
11. Wait 10 seconds, then open valve V-1.
12. Wait 30 seconds, then open valve V-2.
13. After approximately 3 minutes of pumping, zero both the *pump* gauge and the *driver* gauge.

D.1.3 Gas Gun Fill Procedure

1. Insure that the gun is completely pumped down and that the *driver* and *pump* gauges are both zeroed.
2. Verify all systems are ready for firing the gas gun.
3. Tokamak operation notes:

    - Insure baseline data has been taken.
    - Tokamak turbo pump is isolated.
    - Gas puffing systems on line for tokamak.
    - Data acquisition systems online.
    - Interlock in place and tested.
    - Optical firing valve control tested.
    - TIP baseline data taken and laser path not blocked.

4. All personnel present in the gun room must move to the control area.
5. OPEN tank source valves and observe pressures.
6. Shut valves V-1 and V-2 and conduct room sweep.
7. Turn valves F-1 and F-2 to the *off* position.
8. Open valve He-1 to pressurize the pump tube lines.

9. Open the appropriate N valve to pressurize the driver tube lines beginning with lowest pressure tank first.
10. Turn valve F-2 to the *fill* position to fill the pump tube to about 100 psi. NOTE: If the piston was installed prior to 2 hours before gun operation the piston seals may initially have trouble maintaining a seal between the pump tube and the driver tube. The seals will seal better if the driver tube is filled to a pressure above about 750 psi. If, after several tries of filling the driver tube, the seals still do not work properly, the piston will need to be removed and the seals replaced.
11. Turn valve F-1 to the *fill* position to fill the driver tube to the desired fill pressure. Sequentially SHUT and OPEN the N-valves working from low to high pressure until the desired fill pressure is reached.
12. Turn valve F-2 to the *vent* position to reduce pump tube fill pressure to the desired value for the experiment.
13. Make sure the gun is properly filled and both the pump tube fill pressure and the driver tube fill pressure are at the correct values for the experiment.
14. Close valves G-1 and G-2 to avoid damage to the gauges.
15. Turn on the *vacuum enable* switch.
16. Turn on the *fire* switch located on the front panel of the control box.
17. Isolate all turbo-pumps.
18. OPEN H-1, H-2.
19. Fire gun either by remote actuation or by Tokamak control system.
20. Immediately SHUT H-1,H-2 once gun has fired.
21. PRESS in emergency dump button.

D.1.4 Post-Firing Procedure

1. Always wear hearing protection during the venting of the gun.
2. Open valve G-1 to read pressure in the pump tube.
3. Press in the *emergency stop* button to vent the driver tube if not done.

4. Very slowly open valve G-2 to read pressure in the pump tube. If it looks like the pressure is greater than the gauge can handle, then close valve G-2.
   **NOTE:** If the *pump* gauge reads atmospheric pressure (about 15 psi) after G-2 has been opened and the shot did not involve shooting a bullet, then the piston is probably on the front side of the fill hole trapping high pressure driver gas in the central breech. Extreme caution should be exercised when disassembling the central breech.
5. Turn valve F-2 to the *vent* position to vent the pump tube.
6. Verify that the gun has been fully vented by looking at the driver and pump tube gauges. They should read about 15 psi when the gun is fully vented.
7. Close all source tanks.
8. Open valves P-1, P-2, to fully vent the two source lines and the firing lines.
9. Disconnect vacuum hose and shut down vacuum pump.
10. Only after the gun has been fully vented can the *vacuum enable* switch be moved to the off position.
11. OPEN and SHUT N-1,2,3 and He-1 to vent those lines.
12. Shut down power to the control box by pushing the *power* button.

D.1.5 Aborted Firing Procedure

1. Immediately press EMERGENCY DUMP button.
2. SHUT any open N valve and He-1.
3. Slowly open G-1 and G-2 to observe system pressure.
4. Once pressures in system are less than 200 psi, proceed with normal shutdown.

D.1.6 Aborted Pump Down Procedure

**NOTE**: The vacuum pump should not be shut down until the following procedure is completed:

1. Shut valve V-2 to isolate the pump tube from the vacuum pump.
2. Turn valve F-2 to the *vent* position to bring the pump tube up to atmospheric pressure.
3. Shut valve V-1 to isolate the driver tube from the vacuum pump.
4. Turn valve F-2 to the *vent* position to bring the driver tube up to atmospheric pressure.
5. Disconnect the vacuum hose and shut down the vacuum pump.

## D.2 Diaphragm Cutting And Testing Procedure

### D.2.1 Score Depth Determination

The stainless steel diaphragms must be cut specifically for each set of operating pressures. Figure D.2A shows the machining dimensions of a diaphragm. Unfortunately, no scaling equation is available to accurately predict the score depth. Determination of the exact depth is achieved through direct testing by simply cutting diaphragms to known depths and firing the gun. This is a highly tedious process requiring several man-days of work.

Initially the testing should begin at score depths 0.005" shallower than the predicted opening depth and get progressively deeper in 0.005" increments. Table D.1 shows some historical operating points that can be extrapolated or interpolated to roughly predict the opening score depth.

Table D.1 Historical Gas Gun Operating Parameters

| Gas Types | Driver Pres. (psi) | Pump Tube Pres. (psi) | Burst Pres. (psi) | Thickness mills(gage)* | Score depth (mills) |
|---|---|---|---|---|---|
| $N_2/N_2$ | 2000 | 95 | 50000 | 80(14) | 22 |
| $N_2$/He | 1600 | 42 | 42000 | 80(14) | 26 |
| $N_2$/He | 1900 | 45 | 56000 | 75 | 11 |
| $N_2$/He | 1900 | 73 | 35000 | 75 | 38 |

*All diaphragms made of annealed 304 stainless steel

Once the opening depth has been bracketed, experience has shown that 0.002" increments should be used to finally choose the score depth. Ideally, the diaphragm should open fully along the score marks, but not show any signs of failure that could lead to pieces of the diaphragm detaching and traveling down range. A properly chosen score depth will yield consistent probe velocities and not measurably affect the affect the timing of a shot.

D.2.2 Diaphragm Cutting Procedure

1. Obtain 304 annealed stainless steel of desired thickness (typically 0.075").
2. Sheer steel into 4" x 4" squares.
3. Determine the most closely perpendicular corner and clip with sheer.
4. File edges to remove burs.
5. Lightly scrawl pattern shown in figure D.2b on surface of diaphragm.
6. Using the specially designed drilling "jig" drill pilot holes in diaphragm.
7. Remove from jig and expand holes with letter 'F' drill.
8. Remove burs created in drilling process.
9. Set up milling machine to use trenching tool with diaphragm cutting "jig".
10. Using specially designed cutting "jig", cut diaphragms to desired depth.
    **Note**: Depth of cut on each pass should not exceed 0.012".
    Avoid allowing trench to exceed boundary lines.

11. Clip corners of diaphragm such that entire diaphragm can fit inside gripping rings as shown in figure D.2c. Care should be take to preserve indexing holes as much as possible.

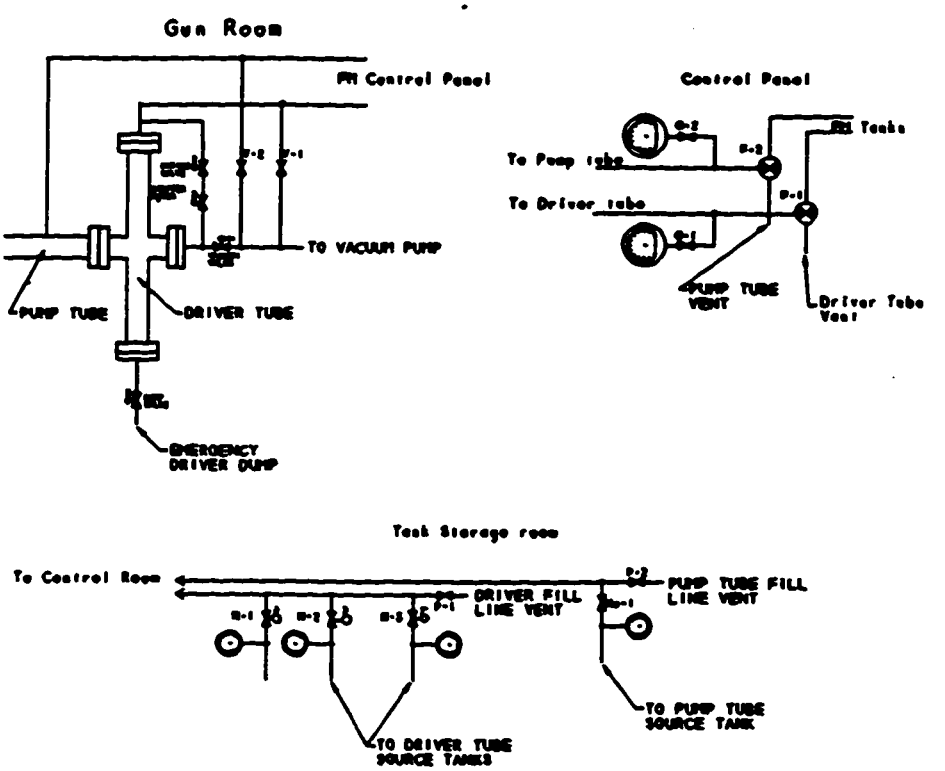


Figure D.1 Schematic of gun control system.

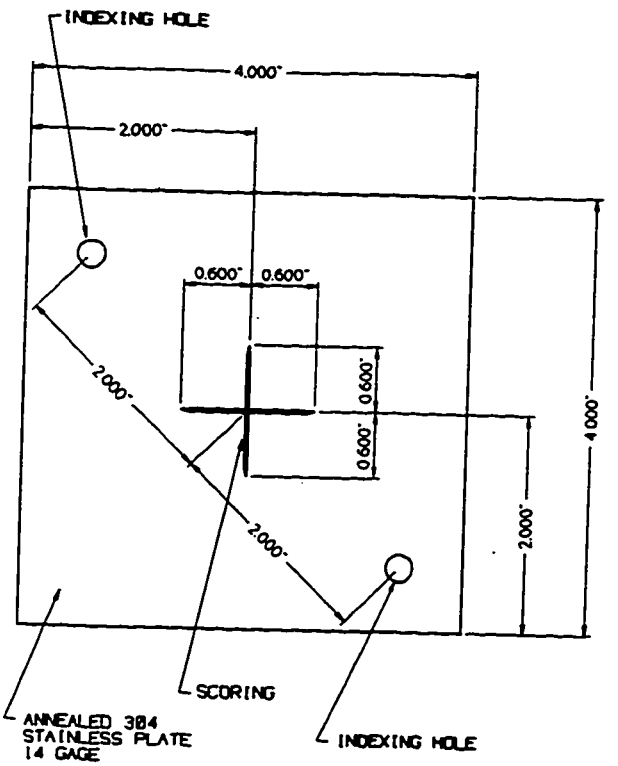


Figure D.2a Diagram of stainless steel diaphragm.

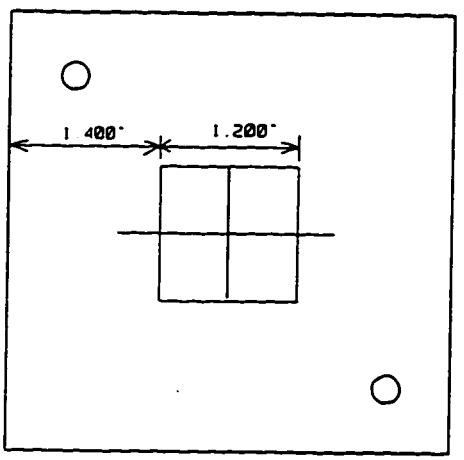


Figure D.2b Diagram of markings for cutting stainless steel diaphragms.

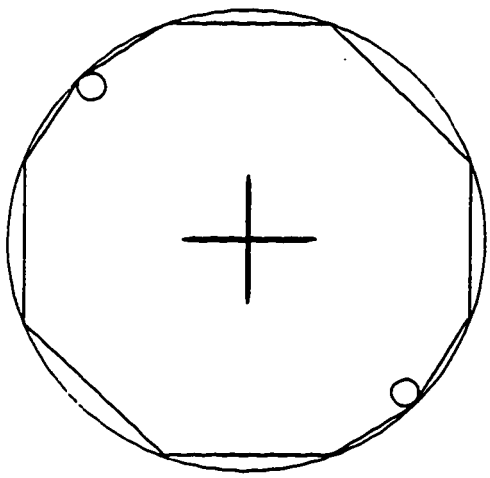

Figure D.2.c Diagram of trimmed stainless steel diaphragm.

## D.3 Bridgeman Seals

Bridgeman seals should be contracted out to CNC capable shops in orders of 100 or more. The dimensions and tolerances required are shown below in Figure D.3.

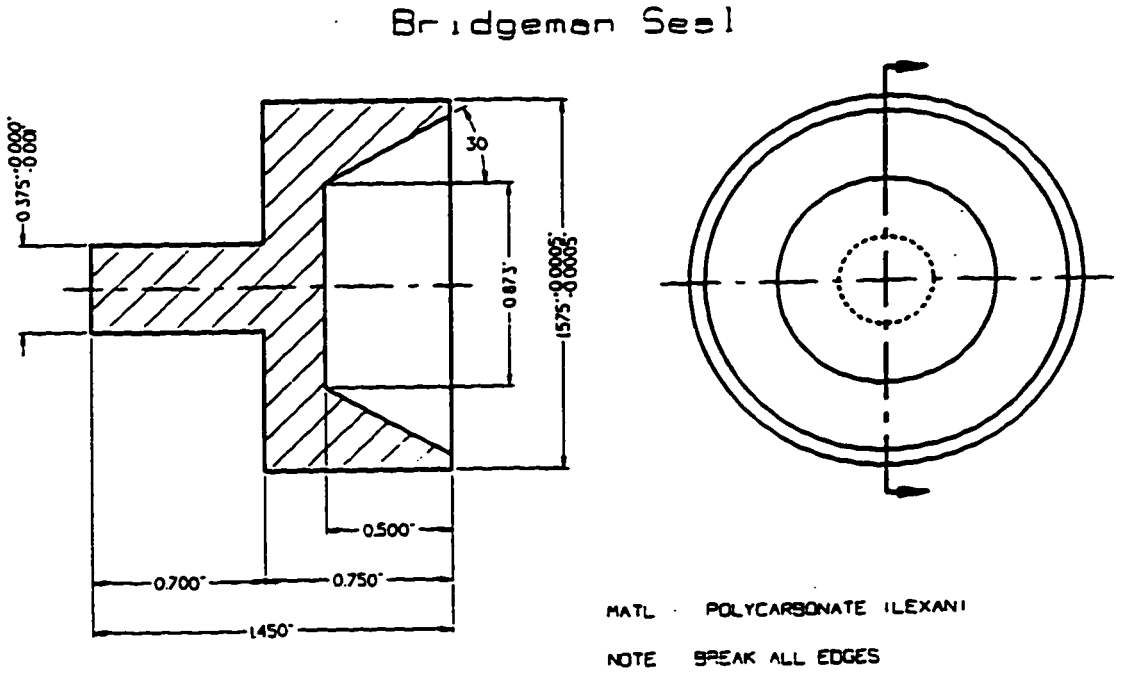


Figure D.3 Schematic of Lexan bridgman seals.

## D.4 Cleaning Procedure

### D.4.1 Pump Tube Cleaning Procedure

1. Insure gas gun is fully vented and stepper motor is de-energized.
2. Disconnect coupler and remove gripping flanges, diaphragm, and pump tube insert.
3. Remove breech flange and push piston out of pump tube. This may require the steel pushing bar.
4. Remove breech insert.
5. Fold terry towel over twice and cover 1¼" diameter pvc tube end. Soak towel with Acetone and drive towel through pump tube with twisting motion to remove all residue left from o-ring seals.
6. Repeat if necessary.
7. Clean breech and pump tube inserts with alcohol.
8. Clean piston with acetone and replace o-rings and bridgeman seal.

Note: Be careful to avoid rolling pump tube into gun barrel and also avoid bumping laser alignment system with pvc cleaning tube.

### D.4.2 Barrel Cleaning Procedure

1. Insure vacuum system is fully vented.
2. Remove mylar diaphragm holder and remaining mylar diaphragm.
3. Roll terri towel into ½" diameter pieces and soak with alcohol.
4. User aluminum cleaning rod to drive towels through barrel.
5. Repeat until towels exit with only light gray sheen.
6. Clean mylar diaphragm holder with alcohol.

## D.5 Alignment Procedures

This procedure assumes the TIP diagnostic has been installed and properly aligned with the desired flight path. Once this has been achieved the barrel is firmly anchored. All future system alignments are based on making the laser coincident with the bore of the gun since this will be the flight of the probe. Care should be taken to avoid movements of equipment relative to the gun barrel.

Note: This procedure requires access to the muzzle and consequently must be completed prior to gas interface system pump down.

1. Adjust beam expander and aperture on laser alignment system for most consistent beam size and shape.
2. Install centering target in breech of barrel.
3. Remove hand port near muzzle and install alignment mirror to observe the bore.
4. Use steering mirrors in laser alignment system to center beam precisely in bore.
5. Remove beam target and observation mirror.
6. Use hydraulic lift system to center pump tube on alignment beam.

This beam is used to align flapper valve, speed beams, and the illumination laser. Use extreme caution to avoid misalignment.

# Appendix E Data Reduction And Analysis Codes

## E.1 MAG.PRO

```
Pro MAG,Pos,angle
; This program converts detector data into polarization angle.
; It does it first by direct calculation assuming perfect 60 deg.
; separtion between detectors. This is stored in RANGLE.
; Then the program uses calibration curves and minimization to solve for
; the polarization angles and stores them in ANGLE in file ANGLE.LIS
;
; This section reads in the raw detector data as p1,p2,p3.
; It then gives the option of reading offset data.  The detector data
; then becomes v1,v2,v3.  The velocity is then read and the desired
; range of points to be analyzed is entered. (These correspond to their
; subscripted values.
;
;
  PRINT, FORMAT='($,"Enter the shot number  ")'
  READ,shot
  SET_DB,'HITDATA'
  shot=SET_SHOT(shot)
  p1=DATA('DET1_0001')
  p2=DATA('DET2_0001')
  p3=DATA('DET3_0001')
  time=DATA('DET1_0001_TM')
  n=N_ELEMENTS(p1)
  PRINT, FORMAT='($,"Enter the offset data shot number or 0 ")'
  READ,offshot
  IF offshot NE 0 THEN BEGIN
        offshot=SET_SHOT(offshot)
        off1=DATA('DET1_0001')
        OFF2=DATA('DET2_0001')
        OFF3=DATA('DET3_0001')
        v1=p1-off1
        v2=p2-off2
        v3=p3-off3
  ENDIF ELSE BEGIN
        v1=p1
        v2=p2
        v3=p3
  ENDELSE
  shot=SET_SHOT(shot)
  vel=2000.0
  Line41:
  PRINT,FORMAT='($,"Enter the first speed spike in msec  ")'
  READ,t1
  PRINT,FORMAT='($,"Enter the second speed spike in msec  ")'
  READ,t2
  d1=abs(time*1000.0-t1)
  d2=abs(time*1000.0-t2)
  tzero=WHERE(d1 LT 0.0001)
  tlast=WHERE(d2 LT 0.0001)
  tzero=tzero(0)-150
  tlast=tlast(0)+400

;
; This section calculates position and the direct calculation of
; polarization angle asuming ideal conditions.
;
  pos=vel*time
  v1=v1(tzero:tlast)
  v2=v2(tzero:tlast)
  v3=v3(tzero:tlast)
```

```
pos=pos(tzero:tlast)
n=N_ELEMENTS(V1)
PRINT,'The number of elements is  ',n
V=[V1,V2,V3]
PLOT,pos,v1,YRA=[MIN(V),MAX(V)],XRA=[MIN(POS),MAX(POS)]
OPLOT,pos,v2
OPLOT,pos,v3
Print,Format='($,"Do you want to re-enter start stop?(1 for yes)")'
Read,reply
IF reply EQ 1 THEN GOTO, line41
shot=shot+1

Print,Format='($,"Do you want a hard copy?(1 for yes)")'
READ,answer
      IF answer EQ 1 THEN BEGIN
      HP
      PLOT,pos,v1,YRA=[MIN(V),MAX(V)],XRA=[MIN(POS),MAX(POS)],tit=$
      'SHOT  '+stremo(shot)
OPLOT,pos,v2
OPLOT,pos,v3
      HPOUT
      endif
Print,'Press any key to continue '
ch=GET_KBRD(1)

; This section obtains the coeficients from the calibration curves.
; These curves are generated from the program JPOLAR.PRO.
; It also normalizes the data by calling the function NORM
;
PRINT,'Get coeficients '
GETCOEF,c1,c2,c3
PRINT,'Normalize'
NORM,v1,v2,v3
V=[v1,v2,v3]
nn=N_ELEMENTS(pos)
print,nn
POST=-200.0+(400.0/nn)*FINDGEN(nn)
PLOT,POST,V1,yra=[MIN(V),MAX(V)]
OPLOT,POST,V2,CO=2
OPLOT,POST,V3,CO=3
Print,Format='($,"Do you want a hard copy?(1 for yes)")'
READ,answer
      if answer EQ 1 then begin
      HP,/port
      !p.multi=[0,1,2]
      PLOT,POST,V1,yra=[0,1.0],xtit="Position (cm)",ytit=$
      "Normalized Intensity (Arb Units)",charsize=1.5
      oPLOT,POST,V2
      oPLOT,POST,V3
      hpout
      endif
!p.multi=[0,1,1]
 nnn=N_ELEMENTS(v1)
 Print,"The first tip data point is:  ",tzero
 Print,"The last tip data point is:  ",tlast
 Print,"The total tipdata points is:  ",nnn

;  Calculate the polarization angles using CALC_ANG. This is done by
;  calculating the remainder of the least squares function and
;  taking the derivitive.  This function is called RPOLY.  The
```

```
;  zeros of RPOLY are found using ROOT and then evaluated to determine
;  which root represents a minimum.  The x-coordinate is then stored
;  in variable called angle
;


  diff=0.0
  bsangle=0.0
  Angle=FLTARR(n)
  FOR i=0,n-1 DO BEGIN
        Angle(i)=CALC_ANG(v1(i),v2(i),v3(i),c1,c2,c3)
        diff=Angle(i)-bsangle
        if diff GT 45 then Angle(i)=Angle(i)-180
        if diff LT -45 then Angle(i)=Angle(i)+180
        bsangle=angle(i)
  ENDFOR
  PLOT,pos,Angle,YRA=[MIN(angle),MAX(angle)],XRA=[MIN(POS),MAX(POS)]
  PRINT,FORMAT='($,"Do you want a hard copy? 1=y")'
  read,answer
  if answer eq 1 THEN BEGIN
  hp
  PLOT,pos,Angle,YRA=[MIN(angle),MAX(angle)],XRA=[MIN(POS),MAX(POS)],$
  tit='SHOT   ' +stremo(shot)
  hpout
  endif

; This section stores the calculated polarization angles in file
; called angles.lis

  OPENW,U,'Angles.lis',/GET_LUN
  nn=N_elements(angle)
  PRINTF,u,nn
  PRINTF,u,angle
  CLOSE,U
  FREE_LUN,u

  Print,FORMAT='($,"Enter the HIT shot number")'
  READ,shot
  shot=SET_SHOT(shot)
  tf=DATA('T.I_TF')
  tf_tim=DATA('T.I_TF_TM')
  d1=abs(tf_tim*1000-t1)
  d2=abs(tf_tim*1000-t2)
  n=WHERE(d1 LT 0.001)
  m=WHERE(d2 LT 0.001)
  n=n(0)-150
  m=m(0)+400
  tf=tf(n:m)
  nn=N_ELEMENTS(tf)
  Print,"The first data point is ",n
  Print,"The last data point is ",m
  Print,"The total data points ",nn
  openw,3,"current.lis"
  PRINTF,3,tf,FORMAT='(4e16.9)'
  close,3
  plot,pos,tf
  end
```

## E.2 NEW_MAG.PRO

```
PRO NEW_MAG
  COMMON NEW_MAG_COMM,base,ang,tfc,verdet_f,refpt_f,$
  speed_f,nangle_f,calib_f,pitch_s,ctr_s,zangle_s,off1_s,off2_s,$
  xstart_f,xend_f,ylow_f,yhigh_f,ylowr_f,yhighr_f,x0x,y,rot_s,dx1_f,dx2_f,$
  ex,btipcor,bfieldx,resid
  DEFAULT, xsize,100
  DEFAULT, ysize,400

;  This is a widget for fitting the measured data to vacuum data.
;  The measured data is read in from the file called "angles.lis" which is
;  generated by the procedure mag.pro.  The TF current is read in from the
;  file "current.lis" which is also generated from the procedure mag.pro.
;  The positions of the return bundles are obtained by
;  calling the procedure return_pos.pro.  Finally, the calculations are
;  done by the procedure new_mag_event.

;  VARIABLES
;
; m       integer number of points evaluated along bullet flight path
; ang     polarization angle calculated in mag.pro
; tfr     raw tf current in amps
; tfc     tf current converted to megaamps
; x0x     x position of return bundles in meters
; y       y position of return bundles converted to an impact parameter
; verdet  verdet coeficient
; refpt   sets position of centercolumn
; speed   bullet speed
; nangle  polarization angle associated with zero gauss
; calib   correction factor to tf current data
; pitch   final vertical angle of rotation, assumed to be zero at start
; yaw     horizontal rotation
; zangle  horiz angle of incidence of the probe relative to the ctr column
; off1    distance from horizontal impact parameter at beginning of track
; off2    distance from horizontal impact parameter at end of track
; ylow    sets lower y axis range for magnetic plot
; ylowr   sets lower y axis range for residual plot
; yhigh   sets upper y axis range for magnetic plot
; yhighr  sets upper y axis range for residual plot
; xstart  sets beginning of both plots
; xend    sets end of both plots

  angles=''
  current=''

  Print,FORMAT='($,"Enter the filename containing the polar angles")'
  read,angles
  m=1
  openr,1,angles
  readf,1,m
  ang=fltarr(m)
  readf,1,ang
  close,1

  Print,FORMAT='($,"Enter the filename containing the tf current")'
  read,current
  openr,2,current
  tfr=fltarr(m)
  readf,2,tfr
  close,2
  tfc=tfr/1000000.0
```

```
xxx=findgen(m)
plot,xxx,tfc
Print,"type something stupid"
read,bs

TEK_COLOR

base=WIDGET_BASE(/COLUMN)
draw_base=WIDGET_DRAW(base,XSIZE=xsize,YSIZE=ysize)

files_base=WIDGET_BASE(base,/ROW)
        quit=WIDGET_BUTTON(files_base,VALUE="QUIT")
        yhighr_f=CW_FIELD(files_base,/COLUMN,/FLOATING,/RETURN_EVENTS,$
        TITLE="Resid Yhigh",VALUE=500.0)
        dx1_f=CW_FIELD(files_base,/COLUMN,/FLOATING,/RETURN_EVENTS,$
        TITLE="axial offset (mm)",VALUE=0.0)
        dx2_f=CW_FIELD(files_base,/COLUMN,/FLOATING,/RETURN_EVENTS,$
        TITLE="axial offset (mm)",VALUE=0.0)
measure_base=WIDGET_BASE(base,/ROW)
        verdet_f=CW_FIELD(measure_base,/COLUMN,/FLOATING,/RETURN_EVENTS,$
        TITLE="Verdet Constant",VALUE=0.00944)
        refpt_f=CW_FIELD(measure_base,/COLUMN,/FLOATING,/RETURN_EVENTS,$
        TITLE="Reference Position",VALUE=0.0)
        speed_f=CW_FIELD(measure_base,/COLUMN,/FLOATING,/RETURN_EVENTS,$
        TITLE="Speed (m/s)",VALUE=1950.0)
        nangle_f=CW_FIELD(measure_base,/COLUMN,/FLOATING,/RETURN_EVENTS,$
        TITLE="Null Angle",VALUE=8.0)
        calib_f=CW_FIELD(measure_base,/COLUMN,/FLOATING,/RETURN_EVENTS,$
        TITLE="Calibration factor",VALUE=1.0)

corr_base=WIDGET_BASE(base,/ROW)
      pitch_s=CW_FIELD(corr_base,/COLUMN,/FLOATING,/RETURN_EVENTS,$
      TITLE="Pitch Angle",VALUE=0.0)
      ctr_s=CW_FIELD(corr_base,/COLUMN,/FLOATING,/RETURN_EVENTS,$
      TITLE="Ctr off dist.(mm)",VALUE=0.0)
      rot_s=CW_FIELD(corr_base,/COLUMN,/FLOATING,/RETURN_EVENTS,$
      TITLE="Zangle",VALUE=0.0)
      off1_s=CW_FIELD(corr_base,/COLUMN,/FLOATING,/RETURN_EVENTS,$
      TITLE="Offset 1",VALUE=0.0)
      off2_s=CW_FIELD(corr_base,/COLUMN,/FLOATING,/RETURN_EVENTS,$
      TITLE="Offset 2",VALUE=0.0)

graph_base=WIDGET_BASE(base,/ROW)
      xstart_f=CW_FIELD(graph_base,/COLUMN,/FLOATING,/RETURN_EVENTS,$
      TITLE="Xstart",VALUE=-200.0)
      xend_f=CW_FIELD(graph_base,/COLUMN,/FLOATING,/RETURN_EVENTS,$
      TITLE="Xend",VALUE=200.0)
      ylow_f=CW_FIELD(graph_base,/COLUMN,/FLOATING,/RETURN_EVENTS,$
      TITLE="Ylow",VALUE=-500.0)
      yhigh_f=CW_FIELD(graph_base,/COLUMN,/FLOATING,/RETURN_EVENTS,$
      TITLE="Yhigh",VALUE=9500.0)
      ylowr_f=CW_FIELD(graph_base,/COLUMN,/FLOATING,/RETURN_EVENTS,$
      TITLE="Resid ylow",VALUE=-500.0)

WIDGET_CONTROL,base,/REALIZE
WIDGET_CONTROL,GET_VALUE=win,draw_base
WSET,win
!p.multi=[0,1,2]
XMANAGER,'NEW_MAG',base
```

## E.3 NEW_MAG_EVENT.PRO

```
Pro new_mag_event,ev

COMMON NEW_MAG_COMM,base,ang,tfc,verdet_f,refpt_f,$
speed_f,nangle_f,calib_f,pitch_s,ctr_s,zangle_s,off1_s,off2_s,$
xstart_f,xend_f,ylow_f,yhigh_f,ylowr_f,yhighr_f,x0x,y,rot_s,dx1_f,dx2_f,$
ex,btipcor,bfieldx,resid

; This is the procedure which calculates the correction to the TIP
; data and returns it as BTIPCORR.  It also calculates the vacuum fields
; along the bullet trajectory using CALC_VACB and returns them as BFIELDX.  It
; subtracts the difference and returns it as RESID.

;VARIABLES:
;
; input variables are described in the widget procedure NEW_MAG
;
; tfi is the TF current in mega-amps corrected for calibration offset
; xline,yline are just arrays used to plot the zero line on the graphs
;
  type=TAG_NAMES(ev,/structure)
  IF(type NE "WIDGET_BUTTON") THEN BEGIN
        WIDGET_CONTROL,verdet_f,GET_VALUE=verdet
        WIDGET_CONTROL,refpt_f,GET_VALUE=refpt
        WIDGET_CONTROL,speed_f,GET_VALUE=speed
        WIDGET_CONTROL,nangle_f,GET_VALUE=nangle
        WIDGET_CONTROL,calib_f,GET_VALUE=calib
        WIDGET_CONTROL,pitch_s,GET_VALUE=pitch
        WIDGET_CONTROL,ctr_s,GET_VALUE=ctr
        WIDGET_CONTROL,rot_s,GET_VALUE=zangle
        WIDGET_CONTROL,off1_s,GET_VALUE=off1
        WIDGET_CONTROL,off2_s,GET_VALUE=off2
        WIDGET_CONTROL,xstart_f,GET_VALUE=xstart
        WIDGET_CONTROL,xend_f,GET_VALUE=xend
        WIDGET_CONTROL,ylow_f,GET_VALUE=ylow;
        WIDGET_CONTROL,yhigh_f,GET_VALUE=yhigh;
        WIDGET_CONTROL,ylowr_f,GET_VALUE=ylowr
        WIDGET_CONTROL,yhighr_f,GET_VALUE=yhighr
        WIDGET_CONTROL,dx1_f,GET_VALUE=dx1
        WIDGET_CONTROL,dx2_f,GET_VALUE=dx2

 yaw=0.0
 m=N_ELEMENTS(ang)
 tfi=tfc*calib
 rot=0

 CALC_VACB,ang,tfi,verdet,refpt,speed,nangle,pitch,off1,off2,$
 bfieldx,btipcor,resid,ex,yaw,rot,ctr,dx1,dx2,zangle


 xline=FINDGEN(2*m)
 xline=xline-xline(m)
 yline=FLTARR(2*m)

 plot,ex,btipcor,xra=[xstart,xend],yra=[ylow,yhigh],tit=$
 "Comparison with vacuum (vacuum is dashed)",xtit="Position (cm)",$
 ytit="Magnetic Field (gauss)"
 oplot,ex,bfieldx,co=2,linestyle=2

 plot,ex,resid,xra=[xstart,xend],yra=[ylowr,yhighr],tit=$
 "Calculated Vacuum field minus Measured",xtit="Position (cm)",$
```

```
ytit="Magnetic Field (gauss)"
oplot,xline,yline

ENDIF ELSE WIDGET_CONTROL,/DESTROY,ev.TOP
END
```

## E.4 CALC_VACB.PRO

```
  Pro calc_vacb,ang,tfi,verdet,refpt,speed,nangle,pitch,off1,off2,$
  bfieldx,btipcor,resid,ex,yaw,rot,ctr,dx1,dx2,zangle
;
; This program takes flight profile parameters and calculates the vacuum
; magnetic field along the assumed path of the bullet.  It takes into
; account the individual TF coil elements and allows for rotating the
; ctr column. This is done by calling the procedure ctr_pos.pro.
; Calc_vac returns BFIELDX, BTIPCORR,RESID which are described in
; the procedure NEW_MAG_EVENT.pro.
;
  m=N_ELEMENTS(ang)
  x0=refpt
  jang=ang-nangle
  vel=speed/1000000.0

  offrt=(off2-off1)/(1000.0*m)
  off=FINDGEN(m)
  off=off*offrt+off1/1000.0

  fltangle=atan((off2-off1)/(vel*1000.*m))
  fltangle=fltangle*57.2958
  pitch=pitch-fltangle


;
; The axial location of the center of each coil element in meters is
; read in from an array called x0x stored in file coil_pos.dat which has
; 41 elements starting at top working clockwise around the tokamak with
; center column as one position last, at  0.0. The vertical positons are
; stored in array called y  which is later converted to an impact parameter
; by subtracting the nominal impact distance of 0.1778m from each point.


  return_pos,xcoils,ycoils,dx1,dx2
  ctr_pos,rot,ctrx,ctry

  ctrx=ctrx*0.0254
  ctry=ctry*0.0254

  x0x=[xcoils,ctrx]
  y=[ycoils,ctry]

; imp is a matrix of impact parameters relative to each coil element as the
; bullet travels along its flight path.
; xx is a matrix of the axial position along the flight path relative to
; each coil element.
; bx and by are the matrix contributions to the field prior to multiplying
; by the toroidal field current and mu-not.
; toby and tobx are the field contributions from the 40 return bundles
; bctry and bctrx are the contributions from the center conductor
; bfielx is the x component of the calculated magnetic field
; bfieldy is the y component of the calculated magnetic field
; bvac is the calculated magnetic field
; theta is angle bvac makes relative to bullet path

  imp=FLTARR(m,113,/nozero)
  xx=FLTARR(m,113,/nozero)
  bx=xx
  by=xx
```

```
toby=FLTARR(m)
tobx=FLTARR(m)
tobctrx=tobx
tobctry=tobx
tobstrapx=tobx
tobstrapy=tobx

bfieldx=FLTARR(m)
bfieldy=FLTARR(m)
bvac=FLTARR(m)
theta=FLTARR(m)
x=FINDGEN(m)
x=x0+x*vel-2.048
zang=zangle*!pi/180
x=x-(x-x(0))*sin(zang)*sin(zang)
y=y-0.1778

FOR j=0,39 DO BEGIN
imp(*,j)=y(j)-off
xx(*,j)=x-x0x(j)
ENDFOR

FOR j=40,112 DO BEGIN
imp(*,j)=y(j)-off-ctr/1000.0
xx(*,j)=x-x0x(j)
ENDFOR


;  This is line 141

bx=imp/(xx^2+imp^2)
by=xx/(xx^2+imp^2)

FOR k=0,39 DO BEGIN
bx(*,k)=0.005*TFI*bx(*,k)
by(*,k)=0.005*TFI*by(*,k)
tobx=tobx+bx(*,k)
toby=toby+by(*,k)
ENDFOR

FOR k=40,76 DO BEGIN
bx(*,k)=-0.005*TFI*bx(*,k)
by(*,k)=-0.005*TFI*by(*,k)
bx(*,42)=0.0
bx(*,60)=0.0
bx(*,66)=0.0
by(*,42)=0.0
by(*,60)=0.0
by(*,66)=0.0
tobctrx=tobctrx+bx(*,k)
tobctry=tobctry+by(*,k)
ENDFOR

;  This eliminates the three empty tubes in the center column


FOR k=77,112 DO BEGIN
bx(*,k)=-0.000833333*TFI*bx(*,k)
by(*,k)=-0.000833333*TFI*by(*,k)
tobstrapx=tobstrapx+bx(*,k)
```

```
  tobstrapy=tobstrapy+by(*,k)
  endfor
;  !p.multi=[0,1,1]


  bfieldx=tobx+tobctrx+tobstrapx
  bfieldy=toby+tobctry+tobstrapy
  theta=atan(bfieldy,bfieldx)
  bvac=sqrt(bfieldy^2+bfieldx^2)
  ex=x*100.0
  bfieldx=SMOOTH(bfieldx,5)*10000.0

;
; Pitch is the final pitch angle
; prate is rate of rotation rate in vertical plane assuming zero at exp tk
; yaw is the final yaw angle
; yrate is the rotation rate in the horizontal plane assuming zero at start

  pts=m*1.0
  prate=pitch*0.017453/pts
  yrate=yaw*0.017453/pts
;
; delta is difference between theta and the refracted pitch angle
; refpitch,refyaw, are the refraction corrected pitch and yaw angles
;
  refpitch=FLTARR(m)
  refyaw=FLTARR(m)
  cverdet=FLTARR(m)
  yang=FINDGEN(m)
  pang=FINDGEN(m)

        yang=yang*yrate
        pang=pang*prate

        refpitch=asin((sin(pang))/1.73)
        refyaw=asin((sin(yang))/1.73)
        length=2*(1.0/(cos(refpitch))/cos(refyaw))
        cverdet=verdet*length
        delta=theta-refpitch

; btipl is btip corrected for the increased length due to pitch yaw
; btipy corrects for yaw, btipcor, then corrects for pitch

  btipl=jang/cverdet
  btipcor=btipl*cos(theta)/cos(delta)
  btipcor=btipcor/cos(refyaw)
  resid=fltarr(m)
  resid=bfieldx-btipcor

  END
```

## E.5 RETURN_POS.PRO

```
PRO return_pos,xcoils,ycoils,dx1,dx2

; This procedure calculates the position of the x,y coordinates of the
; 40 individual return coils.  The variables dx1 and dx2 are used to axially
; move the positon of the four return coils associated with the bundles
; closest to the tip trajectory.

  impa=0.6096
  impb=0.4592
  impc=0.0655
  impd=-0.4211
  impe=-0.8148
  impf=-0.9652
  impg=-0.8148
  imph=-0.4211
  impi=0.0655
  impj=0.4592
  impctr=0.1778

  ya=impa+impctr
  yb=impb+impctr
  yc=impc+impctr
  yd=impd+impctr
  ye=impe+impctr
  yf=impf+impctr
  yg=impg+impctr
  yh=imph+impctr
  yi=impi+impctr
  yj=impj+impctr
  yact=[ya,yb,yc,yd,ye,yf,yg,yh,yi,yj]

; This section calculates the positon of the individual conductors
; relative to the central point given by xo* and imp*.  Note for coil
; c the rotaion angle is 45 deg because the coil is almost parallel to
; the trajectory.  All other coil angles are based on being perpendicular
; to the radius.

  r=0.017677
  pi=3.141593/180.0
  y=fltarr(40)
  x=fltarr(40)
  rota=45.0*pi
  y(0)=ya+r*cos(rota)
  y(1)=ya+r*sin(rota)
  y(2)=ya-r*cos(rota)
  y(3)=ya-r*sin(rota)

  rotb=9.0*pi
  y(4)=yb+r*cos(rotb)
  y(5)=yb+r*sin(rotb)
  y(6)=yb-r*cos(rotb)
  y(7)=yb-r*sin(rotb)

  rotc=45.0*pi
  y(8)=yc+r*cos(rotc)
  y(9)=yc+r*cos(rotc)
  y(10)=yc-r*cos(rotc)
  y(11)=yc-r*cos(rotc)

  rotd=27.0*pi
```

```
y(12)=yd+r*cos(rotd)
y(13)=yd+r*sin(rotd)
y(14)=yd-r*cos(rotd)
y(15)=yd-r*sin(rotd)

rote=9.0*pi
y(16)=ye+r*cos(rote)
y(17)=ye-r*sin(rote)
y(18)=ye-r*cos(rote)
y(19)=ye+r*sin(rote)

rotf=45.0*pi
y(20)=yf+r*cos(rotf)
y(21)=yf-r*sin(rotf)
y(22)=yf-r*cos(rotf)
y(23)=yf+r*sin(rotf)

rotg=9.0*pi
y(24)=yg+r*cos(rotg)
y(25)=yg+r*sin(rotg)
y(26)=yg-r*cos(rotg)
y(27)=yg-r*sin(rotg)

roth=27.0*pi
y(28)=yh+r*cos(roth)
y(29)=yh-r*sin(roth)
y(30)=yh-r*cos(roth)
y(31)=yh+r*sin(roth)

roti=27.0*pi
y(32)=yi+r*cos(roti)
y(33)=yi+r*sin(roti)
y(34)=yi-r*cos(roti)
y(35)=yi-r*sin(roti)

rotj=9.0*pi
y(36)=yj+r*cos(rotj)
y(37)=yj-r*sin(rotj)
y(38)=yj-r*cos(rotj)
y(39)=yj+r*sin(rotj)



;
; The axial location of the center of each coil element in meters is
; read in from a to j and then the center column, which is chosen to
; to be zero.
;
  dx1=dx1/1000.0
  dx2=dx2/1000.0
  x0a=0.0
  x0b=0.4628
  x0c=0.7489-dx1
  x0d=0.7489
  x0e=0.4628
  x0f=0.0
  x0g=-0.4628
  x0h=-0.7489
  x0i=-0.7489+dx2
```

```
x0j=-0.4628
x0ctr=0.0
xx=[x0a,x0b,x0c,x0d,x0e,x0f,x0g,x0h,x0i,x0j]

x(0)=x0a-r*sin(rota)
x(1)=x0a+r*cos(rota)
x(2)=x0a+r*sin(rota)
x(3)=x0a-r*cos(rota)

x(4)=x0b-r*sin(rotb)
x(5)=x0b+r*cos(rotb)
x(6)=x0b+r*sin(rotb)
x(7)=x0b-r*cos(rotb)

x(8)=x0c-r*sin(rotc)
x(9)=x0c+r*cos(rotc)
x(10)=x0c+r*sin(rotc)
x(11)=x0c-r*cos(rotc)

x(12)=x0d-r*sin(rotd)
x(13)=x0d+r*cos(rotd)
x(14)=x0d+r*sin(rotd)
x(15)=x0d-r*cos(rotd)

x(16)=x0e+r*sin(rote)
x(17)=x0e+r*cos(rote)
x(18)=x0e-r*sin(rote)
x(19)=x0e-r*cos(rote)

x(20)=x0f+r*sin(rotf)
x(21)=x0f+r*cos(rotf)
x(22)=x0f-r*sin(rotf)
x(23)=x0f-r*cos(rotf)


x(24)=x0g-r*sin(rotg)
x(25)=x0g+r*cos(rotg)
x(26)=x0g+r*sin(rotg)
x(27)=x0g-r*cos(rotg)

x(28)=x0h+r*sin(roth)
x(29)=x0h+r*cos(roth)
x(30)=x0h-r*sin(roth)
x(31)=x0h-r*cos(roth)

x(32)=x0i-r*sin(roti)
x(33)=x0i+r*cos(roti)
x(34)=x0i+r*sin(roti)
x(35)=x0i-r*cos(roti)

x(36)=x0j+r*sin(rotj)
x(37)=x0j+r*cos(rotj)
x(38)=x0j-r*sin(rotj)
x(39)=x0j-r*cos(rotj)

xcoils=x
ycoils=y
END
```

## E.6 CTR_POS.PRO

```
PRO ctr_pos,rot,ctrx,ctry

;  This program calculates the position of the center column elements.
;  The brass bars are broken up into six elements 0.25 by 0.25 inches each
;  The position of the center column elements are read into to arrays ctrx
;  ctry which can be rotated by the rotation angle rot
;variables used in the program
;
;pi      3.14159265359
;N       number of infinitely long current elements
;xc,yc   positions of current elements(any units)
;I       relative current
;j,k     counters
;xbar,ybar  coordinates of current elements in bar
;xbar60,ybar60 coordinates of current elements in bar rotated 60 degrees
;xbarm60,ybarm60 coordinates of current elements in bar rotated -60 degrees
;a,b     variables used to specify location of cable current elements
;width,thick  width and thickness of brass bar
;nx,ny   number of current elements in x and y direction for each
;        brass bar
; NOTE: positions 3,21,and 27 do not have current elements
;now we establish some variables

pi=3.14159265359
N=73
xc=findgen(N+1)*0
yc=findgen(N+1)*0


;input the position of all the cables
a=1.050
b=a*3^(0.5)/2

xc(1)=-3*a
yc(1)=0
xc(2)=-2*a
yc(2)=0
xc(3)=-1*a
yc(3)=0
xc(4)=-0*a
yc(4)=0
xc(5)=1*a
yc(5)=0
xc(6)=2*a
yc(6)=0
xc(7)=3*a
yc(7)=0

xc(8)=-2*a
yc(8)=2*b
xc(9)=-1*a
yc(9)=2*b
xc(10)=-0*a
yc(10)=2*b
xc(11)=1*a
yc(11)=2*b
xc(12)=2*a
yc(12)=2*b
```

```
 xc(13)=-2*a
 yc(13)=-2*b
 xc(14)=-1*a
 yc(14)=-2*b
 xc(15)=-0*a
 yc(15)=-2*b
 xc(16)=1*a
 yc(16)=-2*b
 xc(17)=2*a
 yc(17)=-2*b

 xc(18)=-5*a/2
 yc(18)=b
 xc(19)=-3*a/2
 yc(19)=b
 xc(20)=-1*a/2
 yc(20)=b
 xc(21)=1*a/2
 yc(21)=b
 xc(22)=3*a/2
 yc(22)=b
 xc(23)=5*a/2
 yc(23)=b

 xc(24)=-5*a/2
 yc(24)=-b
 xc(25)=-3*a/2
 yc(25)=-b
 xc(26)=-1*a/2
 yc(26)=-b
 xc(27)=1*a/2
 yc(27)=-b
 xc(28)=3*a/2
 yc(28)=-b
 xc(29)=5*a/2
 yc(29)=-b

 xc(30)=-3*a/2
 yc(30)=3*b
 xc(31)=-1*a/2
 yc(31)=3*b
 xc(32)=1*a/2
 yc(32)=3*b
 xc(33)=3*a/2
 yc(33)=3*b

 xc(34)=-3*a/2
 yc(34)=-3*b
 xc(35)=-1*a/2
 yc(35)=-3*b
 xc(36)=1*a/2
 yc(36)=-3*b
 xc(37)=3*a/2
 yc(37)=-3*b

  xcc=xc(1:37)
  ycc=yc(1:37)

;input the position of bars current elements.
thick=.250
```

```
width=1.50
ny=1
nx=6
xbar=(findgen(nx)+0.5-nx/2)/nx*width
ybar=fltarr(nx)

        xc1=xbar
        yc1=ybar+3*b+a/2+thick/2
        xc2=xbar
        yc2=ybar-(3*b+a/2+thick/2)

        xbar60=xbar/2-ybar*3^(0.5)/2
        ybar60=ybar/2+xbar*3^(0.5)/2
        xc3=xbar60-3^(0.5)/2*(3*b+a/2+thick/2)
        yc3=ybar60+0.5*(3*b+a/2+thick/2)
        xc4=xbar60+3^(0.5)/2*(3*b+a/2+thick/2)
        yc4=ybar60-0.5*(3*b+a/2+thick/2)

        xbarm60=xbar/2+ybar*3^(0.5)/2
        ybarm60=ybar/2-xbar*3^(0.5)/2
        xc5=xbarm60+3^(0.5)/2*(3*b+a/2+thick/2)
        yc5=ybarm60+0.5*(3*b+a/2+thick/2)
        xc6=xbarm60-3^(0.5)/2*(3*b+a/2+thick/2)
        yc6=ybarm60-0.5*(3*b+a/2+thick/2)

         ctrx =[xcc,xc1,xc2,xc3,xc4,xc5,xc6]
         ctry=[ycc,yc1,yc2,yc3,yc4,yc5,yc6]

;  plot,ctrx,ctry,psym=5

   rmat=[[cos(rot),sin(rot)],[-sin(rot),cos(rot)]]
   xymat=[[ctrx],[ctry]]
   newxymat=xymat#rmat

   ctrx=newxymat(*,0)
   ctry=newxymat(*,1)

; oplot,nctrx,nctry,psym=6,co=2


end
```

## Appendix F Plasma Magnetic Field Calculations

### F.1 Analytical Open Flux Model

One of the goals of the TIP experiment was to investigate the current profile in HIT by measuring the change in toroidal field caused by the plasma and using this data to derive the equilibrium profile using a Grad-Shafranov fitting code called EFIT. Several questions exist concerning the resulting plasma object formed in HIT. One question is whether closed flux is formed.

In order to investigate the question of closed versus open flux, a simplified open flux model was developed to predict the magnetic field profile along the TIP trajectory. These predictions were then compared with closed flux data obtained numerically using the EFIT equilibrium code. All calculations and numerical computations were done using the plasma parameters given in Table F.1.

| | |
|---|---|
| Toroidal field current (KA) | 770 |
| Injector current (KA) | 20 |
| Plasma current (KA) | 225 |
| Open flux (mWebbers) | 5 |

Table F.1 Plasma modeling parameters

The assumptions for the open flux model are as follows:

- no closed flux surfaces
- all plasma current flows along a thin sheath near the flux conserver
- sheath thickness is small, relative to the radius of curvature
- pressure in the plasma is negligible

Figure F.1 shows the dimensions of the tokamak and the location of the current.

Using these assumptions, the equilibrium magnetic fields can be described by the jump equation

$$B_0^2 + B_p^2 = (B_0 + \delta B)^2. \qquad \text{Eq. F.1}$$

In equation F.1, $B_0$ is the vacuum toroidal field, $B_p$ is the poloidal field, and $\delta B_t$ is the paramagnetic increase in toroidal B due to compression. The magnitude of the $\delta B_t$ is assumed small so that the jump equation can be solved for $B_p$

$$B_p \cong \sqrt{2B_o \delta B}. \qquad \text{Eq. F.2}$$

The value of $B_o$ is given by

$$B_0 = \frac{\mu_0 I_v}{2\pi R}. \qquad \text{Eq. F.3}$$

$\delta B_t$ is calculated by assuming the injector current follows the open field lines such that

$$\delta B = \frac{\mu_0 I_{inj}}{2\pi R} \qquad \text{Eq. F.4}$$

Substituting into equation F.2 yields

$$B_p = \frac{\mu_o \sqrt{2 I_{inj} I_{tf}}}{2\pi R}. \qquad \text{Eq. F.5}$$

The plasma current is computed using amperes law

$$\mu_o I_{plasma} = \oint B_p d\ell \qquad \text{Eq. F.6}$$

and the edge safety factor, q, can be calculated using the equation

$$q = \oint \frac{1}{\ell_t} \frac{B_t}{B_p} d\ell_p \qquad \text{Eq. F.7}$$

in which $\ell_p$ is the poloidal length around the plasma and $\ell_t$ is the toroidal length.

This integral can be solved analytically. Taking the values from Table F.1 the plasma current, $I_p$, is 290KA and the safety factor on the edge is 6.8. This calculation assumed no gap between the flux conserver and the plasma. It can be somewhat refined since the amount of flux trapped in the gap between the plasma and the flux conserver can be measured. Table F.1 gives a typical value of 5 miliwebbers of trapped poloidal flux. Taking equation F.5 for the poloidal field, the amount separation required to give 5 miliwebbers of flux in the gap is

$$\psi_p = (2\pi R \Delta x) B_p \qquad \text{Eq. F.8}$$

where $B_p$ is assumed constant over the gap. This results in a separation of 2.3 cm between the plasma and the flux conserver. Re-computing the plasma current and the edge safety factor give, $I_p$ = 220KA and q = 5.31 respectively. The value for the plasma current is somewhat consistent with the measured plasma current. In order to test the validity of this model, the values of the calculated poloidal magnetic field was compared with surface probe measurements. This comparison is shown in figure F.2. Fairly good agreement is obtained. The higher values of $B_p$ measured by the surface probes on the outer flux conserver is an indication the plasma contained closed flux which was Shafranov shifted outward to compress the outer poloidal field and achieve equilibrium.

## F.2 Computed Equilibrium Current Profiles

Assuming the case of closed flux surfaces, the form of the current profile is of great interest as discussed earlier. For low β tokamaks, the plasma pressure can be neglected and the equilibrium can be derived using Taylor's minimum energy method. [36] The result is a force free magnetic configuration given by the equation

$$\nabla \times B = \lambda B \qquad \text{Eq. F.9}$$

where λ is a global constant of the plasma. From this and the ideal MHD form of Ampere's law, the current profile is given by

$$J = \frac{\lambda B}{\mu_o} \qquad \text{Eq. F.10}$$

Three different λ profiles were evaluated using the EFIT code; hollow with the current driven on the edge of the plasma, flat, and peaked with the current more concentrated on the magnetic axis. The lambda profiles for these three cases along with the profile for the open flux case are shown in figures F.3a,b,c.

The plasma current for these evaluations was the same as the current in the open flux case. The difference between the calculated vacuum field and the calculated plasma field each current profiles is shown in Figure F.4. The EFIT compute profiles differ from the open flux model by roughly 100 gauss, which is beyond the present absolute resolution of the TIP diagnostic to differentiate between the open and closed flux case. The difference between the individual closed flux profiles is less than fifty gauss. Relative to the magnitude of the field which is several thousand gauss, these differences are quite subtle. Accuracy of less than 20 gauss (0.2%) over the entire shot is required to resolve these differences by measuring the toroidal field. A trajectory that is tangent to the

poloidal field, however, would directly measure magnetic fields created by the plasma current without interference from the large background toroidal field.

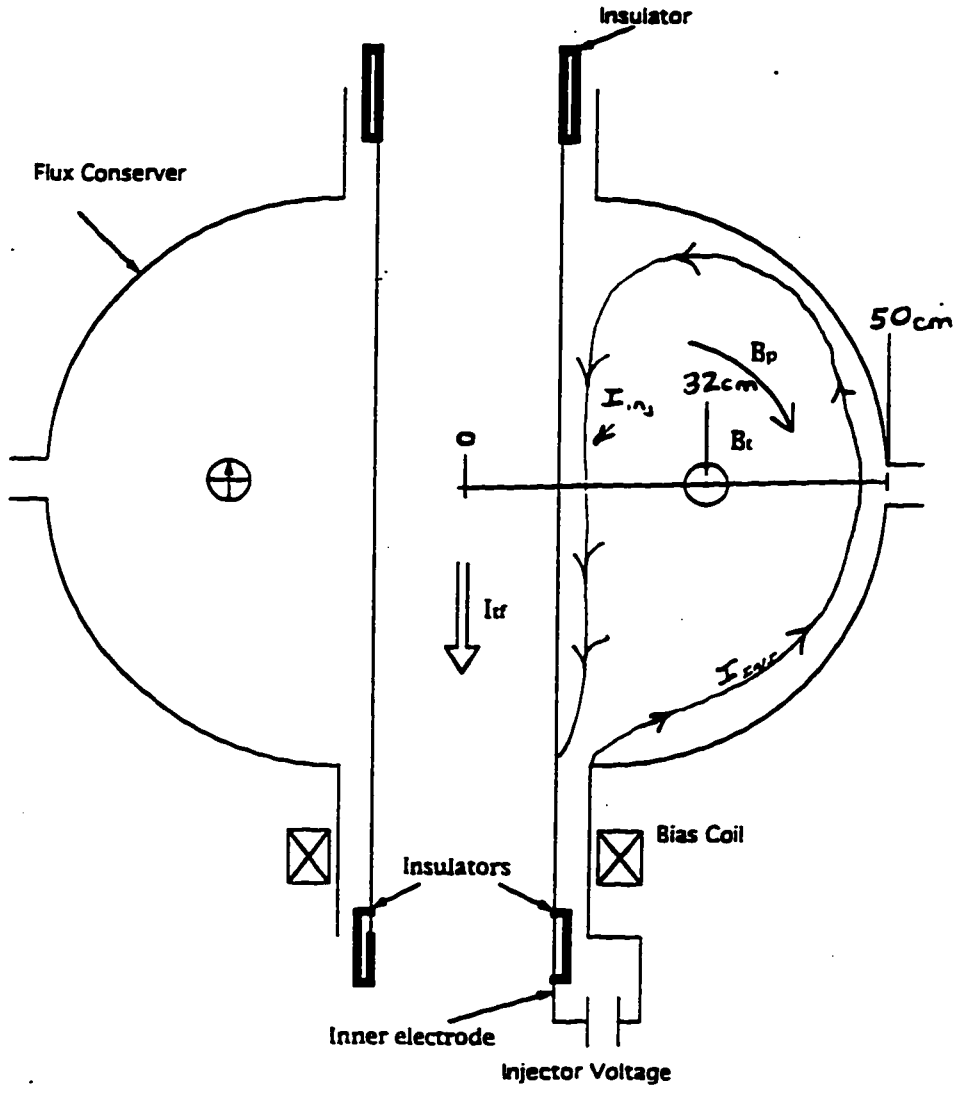


Figure F.1 Schematic drawing of open flux model

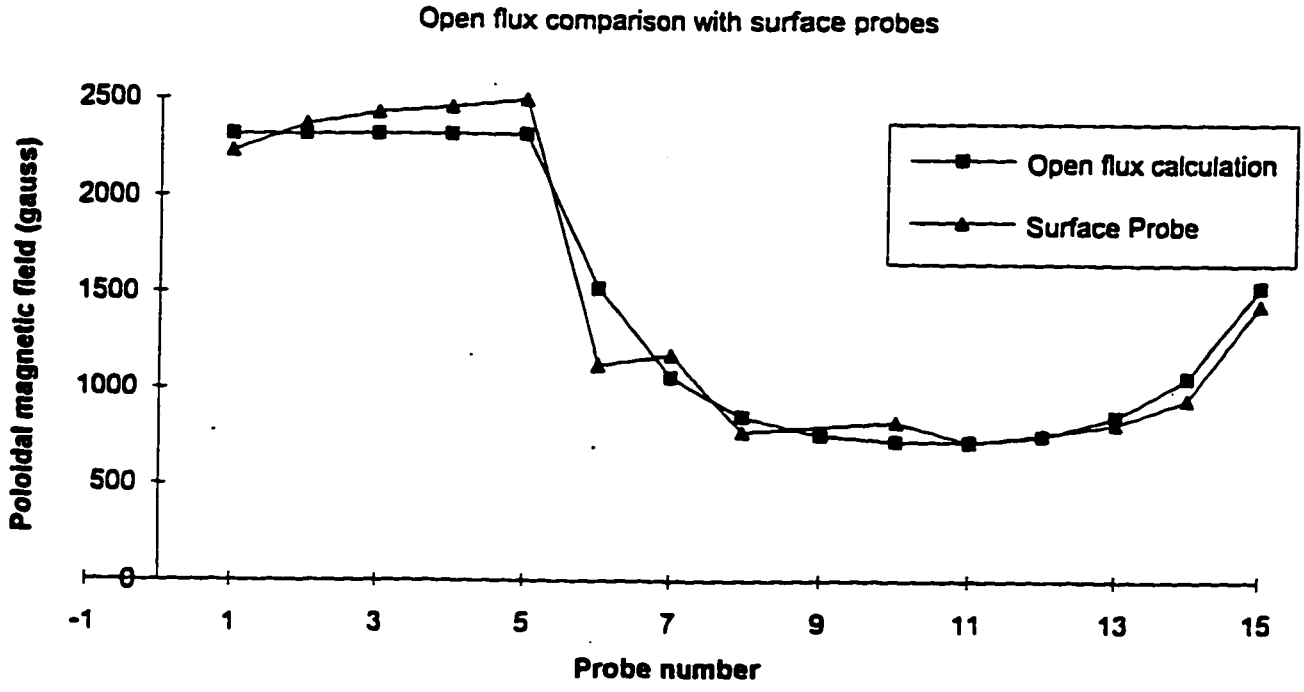


Figure F.2 Comparison poloidal magnetic field calculated by the open flux model with poloidal field probe measurements along flux conserver surface.

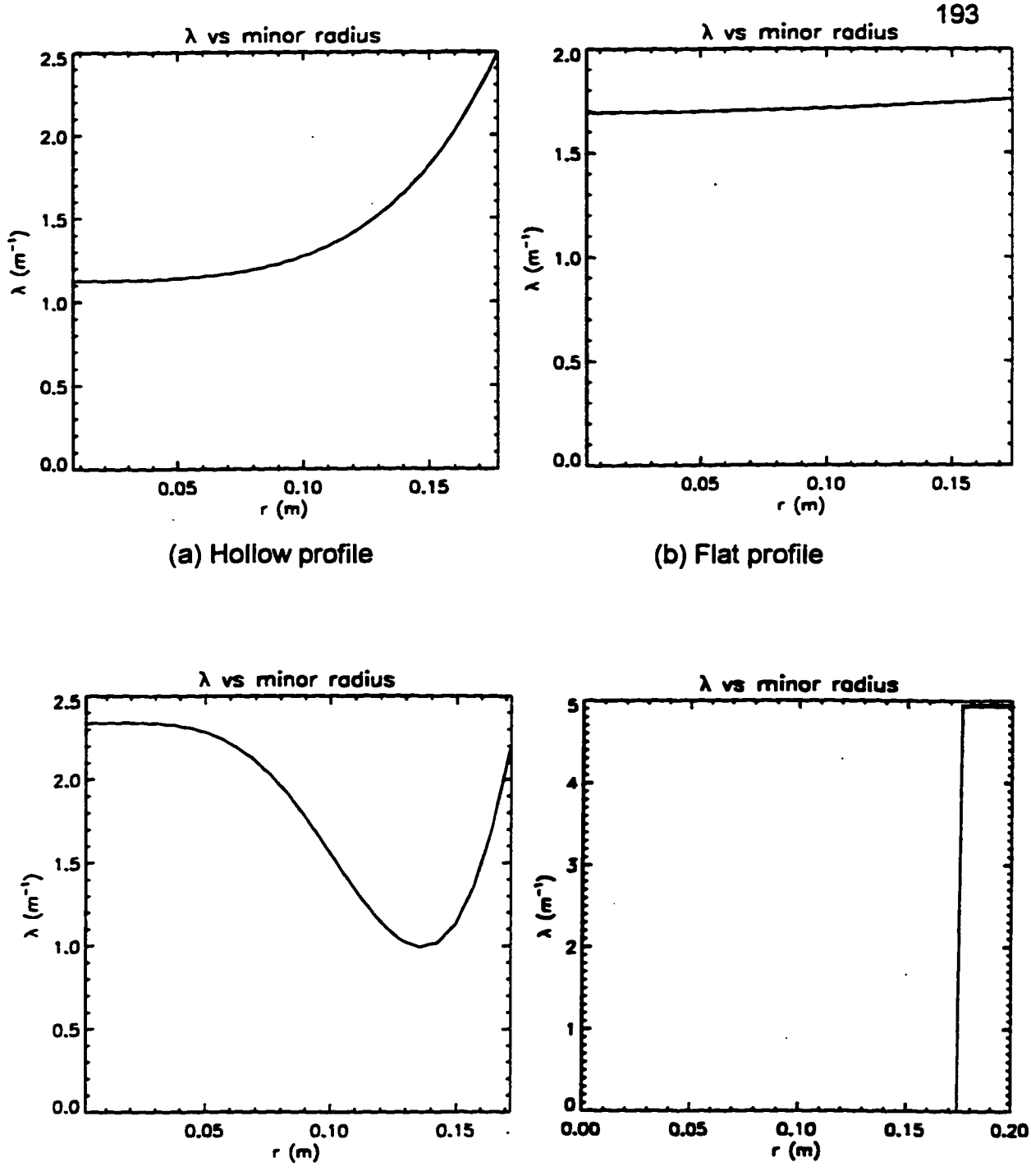


Figure F.3 Plot of λ profiles used to evaluate calculate magnetic field difference from vacuum along TIP trajectory through HIT.

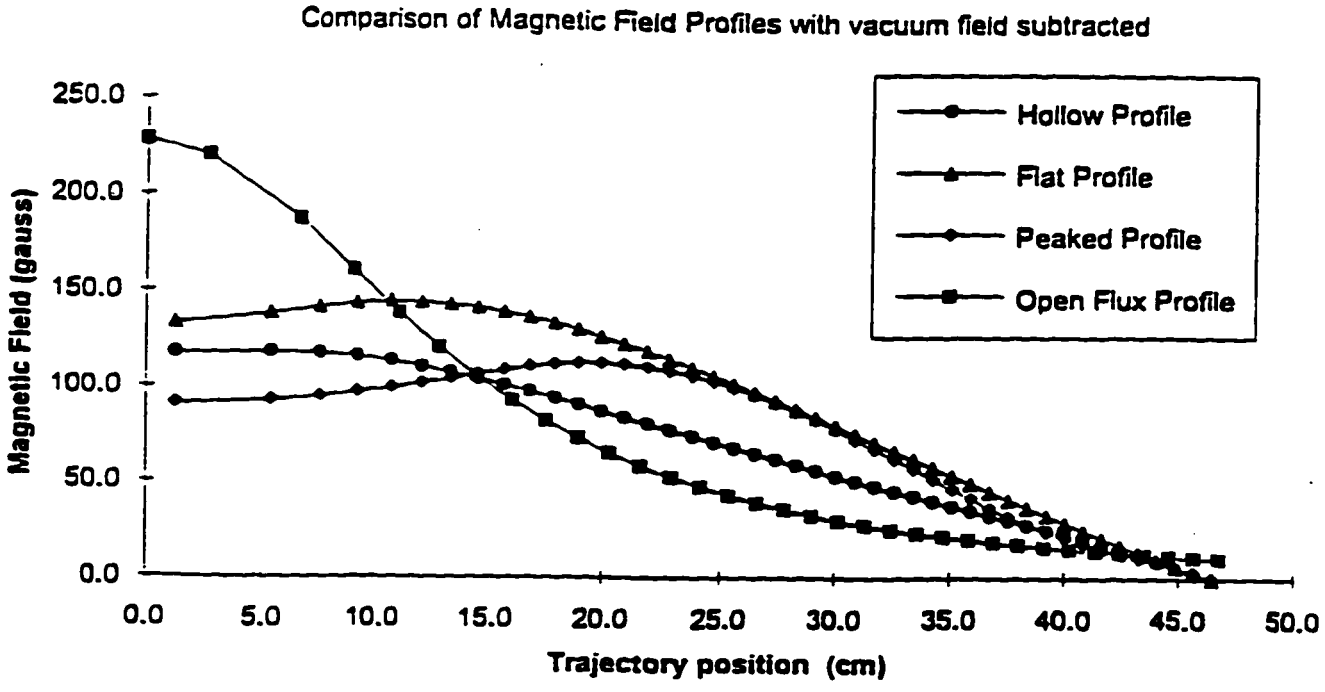


Figure F.4 Comparison of calculated closed flux magnetic field calculations with open flux model. Origin indicates location at closest point of approach directly above the center column.

# James P. Galambos

## EDUCATION:

| | | |
|---|---|---|
| United States Naval Academy<br>Annapolis, MD | 1982-1986 B.S. | Physics |
| Navy Nuclear Power Program<br>Idaho Falls, ID | 1986-1987 Certificate | Nuclear Engineering |
| University of Washington<br>Seattle, WA | 1991-1993 M.S.E. | Nuclear Engineering |
| University of Washington | 1993-1996 Ph.D. | Plasma Physics |

## JOURNAL PUBLICATIONS:

1. Galambos, J. P., Bohnet, M. A., Jarboe, T. R., Mattick, A. T., "Magnetic Field Measurements on the Helicity Injected Tokamak using the Transient Internal Probe," *Review of Scientific Instruments*, (accepted for publication January, 1997).

2. Galambos, J. P., Bohnet, M. A., Jarboe, T. R., Mattick, A. T., "Magnetic Field Measurements using the Transient Internal Probe," *Review of Scientific Instruments*, 67, 469, (1996).

3. Bohnet, M.A., Galambos, J.P., Jarboe, T. R., Mattick, A. T., "The Transient Internal Probe: A Novel Method for Measuring Internal Magnetic Field Profiles;" *Review of Scientific Instruments*, 66, 1197 (1995).

4. Spanjers, G.G., Galambos, J.P., Jarboe, T.R., Wurden, G., Wright, B., "Development of a Transient Internal Probe Diagnostic," *Review of Scientific Instruments*, 63, 5148, (1992).

## CONTRIBUTED PAPER AT PHYSICS CONFERENCE:

T. R. Jarboe, M. Bohnet, J. Galambos, A. Martin, B. Nelson, D. Orvis, J. Xie, L. Zhou, "Recent results of the Helicity Injected Tokamak Experiment," Sixteenth IAEA Fusion Energy Conference, Montreal, Canada, October 7-11,1996.